

UNIVERSIDAD POLITÉCNICA DE MADRID

ESCUELA TÉCNICA SUPERIOR DE INGENIEROS AERONÁUTICOS



# Electrodynamic Tethers For Planetary And De-orbiting Missions

Tesis Doctoral

Antonio Sánchez Torres  
Licenciado en Ciencias Físicas

2013



DEPARTAMENTO DE FÍSICA APLICADA A LA INGENIERÍA AERONÁUTICA

ESCUELA TÉCNICA SUPERIOR DE INGENIEROS AERONÁUTICOS



# Electrodynamic Tethers For Planetary And De-orbiting Missions

Autor

Antonio Sánchez Torres

Licenciado en Ciencias Físicas

Director de tesis

Juan R. Sanmartín Losada

Ph.D. Aerospace Engineering Sciences

Doctor Ingeniero Aeronáutico

2013





**POLITÉCNICA**

Tribunal nombrado por el Sr. Rector Magfco. de la Universidad Politécnica de Madrid, el día.....de.....de 20....

Presidente: \_\_\_\_\_

Vocal: \_\_\_\_\_

Vocal: \_\_\_\_\_

Vocal: \_\_\_\_\_

Secretario: \_\_\_\_\_

Suplente: \_\_\_\_\_

Suplente: \_\_\_\_\_

Realizado el acto de defensa y lectura de la Tesis el día.....de.....de 20...  
en la E.T.S.I./Facultad.....

Calificación .....

EL PRESIDENTE

LOS VOCALES

EL SECRETARIO



CONTENTS

|   |               |
|---|---------------|
| Acknowledgements . . . . .  | v             |
| Agradecimientos . . . . .   | vii           |
| Preface . . . . .   | ix            |
| Abstract . . . . .  | xiii          |
| Resumen . . . . .   | xv            |
| <br><b>1 Interplanetary mission with an electric solar sail</b>         | <br><b>1</b>  |
| 1.1 Introduction . . . . .  | 1             |
| 1.2 Ambient Solar Wind conditions . . . . .                             | 4             |
| 1.3 Potential profile of a single tether . . . . .                      | 6             |
| 1.4 Coulomb-to-Lorentz force ratio . . . . .                            | 8             |
| 1.5 Ion scattering and Coulomb force calculations . . . . .             | 10            |
| 1.6 Interference effects in an e-sail . . . . .                         | 11            |
| 1.7 Earth-to-Jupiter orbit transfer . . . . .                           | 12            |
| 1.8 Discussion . . . . .  | 16            |
| <br><b>2 Scientific missions in Jupiter with electrodynamic tethers</b> | <br><b>19</b> |
| 2.1 Introduction . . . . .  | 19            |

|          |   |           |
|----------|---|-----------|
| 2.2      | Tether radiation in Juno-type and circular-equatorial Jovian orbits . . .   | 21        |
| 2.2.1    | Introduction . . . . .  | 21        |
| 2.2.2    | Ambient and orbital Jovian conditions . . . . .                             | 24        |
| 2.2.3    | Cold-plasma model . . . . .   | 28        |
| 2.2.4    | The wave field from a tether current-density source . . . . .               | 29        |
| 2.2.5    | Radiation impedance formulas . . . . .                                      | 32        |
| 2.2.6    | The FM radiation impedance . . . . .  | 35        |
| 2.2.7    | The Alfven radiation impedance . . . . .                                    | 37        |
| 2.2.7.1  | The Alfven radiation impedance at the equator . . . .                       | 37        |
| 2.2.7.2  | The radiation impedance at the polar caps . . . . .                         | 41        |
| 2.2.8    | The general Alfven radiation impedance . . . . .                            | 42        |
| 2.2.9    | Bare tether radiation impedance . . . . .                                   | 47        |
| 2.2.10   | Discussion . . . . .  | 47        |
| 2.3      | Generation of auroral effects in Jupiter and grain-tether interaction . .   | 50        |
| 2.3.1    | Introduction . . . . .  | 50        |
| 2.3.2    | Generation of auroral effects . . . . .                                     | 51        |
| 2.3.3    | Discussion . . . . .  | 54        |
| 2.4      | Stability analysis for dusty plasmas under grain charge fluctuations . .    | 55        |
| 2.4.1    | Introduction . . . . .  | 55        |
| 2.4.2    | Non-Maxwellian distributions and charging model . . . . .                   | 56        |
| 2.4.3    | Fluid model for electrons and ions . . . . .                                | 57        |
| 2.4.4    | Discussion . . . . .  | 59        |
| <b>3</b> | <b>De-orbiting satellites at end of mission with electrodynamic tethers</b> | <b>63</b> |
| 3.1      | Introduction . . . . .  | 63        |
| 3.2      | Survival against debris . . . . .   | 65        |



|          |  |           |
|----------|--|-----------|
| 3.3      | Current model in tape-tethers . . . . .                                | 66        |
| 3.4      | Conductive tether design for a generic mission . . . . .               | 68        |
| 3.5      | Results . . . . .  | 71        |
| 3.6      | De-orbiting large satellites with rockets . . . . .                    | 76        |
| 3.7      | Discussion . . . . .   | 78        |
| <b>4</b> | <b>Conclusions</b>   | <b>79</b> |
|          | <b>Appendix A The radiation impedance with thermal effects</b>         | <b>95</b> |
|          | <b>Appendix B Modified equinoctial equations for orbital mechanics</b> | <b>99</b> |



## Acknowledgements

The thesis represents a very short road I have just walked over the grand scientific universe, where dreams become reality. I am very grateful to my Thesis Advisor, Prof. Juan Ramon Sanmartin, who gave me the opportunity to be a science-dreamer. He has guided the helm of the ship by a correct pathway of both concise and clear scientific language. He has evinced an invaluable patience and dedication to me since my first steps in the researching field. Sincerely, I am very proud to have learned with him. He also encouraged me to visit the University of Padova for improving my scientific experience.

I could not forget the warm welcome by Prof. Enrico Lorenzini in the wonderful four months I lived in Dante's land. Both cultural and scientific experience there were unforgettable.

I would like to thank all-stars persons and researchers of the Physics department. Specially fruitful was the collaboration with Prof. Jose Manuel Donoso and Prof. Luis Conde in the vast field of dusty plasmas, giving to me several everlasting advices. I am also in gratitude with Prof. Gonzalo Sanchez Arriaga for his disposition and helpful comments. I have to make a special mention for the secretary of the Physics department, Mari Carmen, who always solved my administrative problems with a generous smile.

Finally, I am in an eternal debt to my family, my beloved parents. Without their wise-advice, understanding and dedication I could not have finished my thesis.



## Agradecimientos

La presente tesis representa solo un pequeño camino recorrido sobre la inmensidad del universo científico, donde los sueños siempre se tornan en realidad. Quiero agradecer plenamente a mi Director de Tesis, el Profesor Juan Ramón Sanmartín, por darme la oportunidad de ser un soñador de ciencia. He encontrado en él, el guía que gira el timón del barco por las aguas del cristalino sendero en el que se debe mantener siempre, con la justa brevedad, el difícil lenguaje científico. Desde mis primeros pasos en el campo de la investigación él siempre ha tenido hacia mi persona una inestimable paciencia y dedicación. Sinceramente, estoy muy orgulloso de haber aprendido con él. Además de todo esto, alentó a que prosiguiera mi formación científica con una estancia en la Universidad de Padua.

No puedo olvidar la gran acogida que tuve por parte del Profesor Enrico Lorenzini en los maravillosos cuatro meses que pasé en la tierra de Dante. La experiencia que allí tuve, tanto cultural como científica, fue verdaderamente inolvidable.

Me gustaría agradecer a todas las grandes personas y científicos del Departamento de Física del que gratamente he formado parte durante todo este largo tiempo. Especialmente deseo agradecer a los Profesores Jose Manuel Donoso y Luis Conde por la llama que en mí despertaron sobre el inmenso campo de los plasmas granulares, con consejos ciertamente inolvidables. También agradezco al Profesor Gonzalo Sanchez Arriaga por su plena disposición y sus comentarios de gran interés e utilidad para la tesis. De manera especial quiero agradecer a la secretaria de nuestro departamento de Física, Mari Carmen, cuya capacidad para resolver, con generosa sonrisa, todos los problemas administrativos aún me asombra.

Finalmente, estoy en eterna deuda con mi familia, mis queridos padres. Sin sus sabios consejos, su atención y dedicación, no podría haber llevado a buen puerto la Tesis.



# Preface

## Funding

This thesis was supported by the Ministry of Science and Innovation of Spain under FPI Grant No. BES-2009-013319.

## Publications and presentations

This thesis have been partly or completely published in conference proceedings, book chapters and refereed journals.

### Publications in journals

1. Sanchez-Torres, A., Sanmartin, J. R., Donoso, J. M., and Charro, M., The radiation impedance of electrodynamic tethers in a polar Jovian orbit, *Advances in Space Research*, 45, 1050-1057, 2010.
2. Conde. L, Donoso, J. M., Sanchez-Torres, A., Tkachenko, I. M., de la Cal, E., Carralero, D., y Pablos, J. L., Plasmas Granulares, *Real Sociedad Española de Física*, Vol. 25-3. Julio-Septiembre, 2011.
3. Sanchez-Torres, A. and Sanmartin J. R., Tether radiation in Juno-type and circular-equatorial Jovian orbits, *Journal of Geophysical Research*, Vol. 116, A12, A12226, 1-12, 2011.
4. Charro, M., Sanmartin J. R., Bombardelli, C., Sanchez-Torres, A., Lorenzini, E. C., Garrett, H. B., and Evans, R. W., A proposed Two-Stage Two-Tether Scientific Mission at Jupiter, *IEEE Trans. Plasma Sci.*, vol. 40, no. 2, pp. 274-280, Feb. 2012.

**Other publications***Proceedings*

1. Donoso, J. M., Sanchez-Torres, A., and Conde, L., Stability analysis for dusty plasma under grain charge fluctuations due to non-Maxwellian electron distributions, *Proceedings of the 37th EPS Conference on Plasma Physics*, vol 34A, ISBN: 2-914771-62-2, 2010.
2. Zanutto D., Colombatti, G., Lorenzini, E., Mantellato, R., and Sanchez-Torres, A., Orbital debris mitigation through deorbiting with passive electrodynamic drag, *Proceedings of the 63th International Astronautical Congress*, IAC-12-D9.2.8., ISSN: 0074-1795, 2012.
3. Sanmartin, J. R., Sanchez-Torres, A., Khan, S. B., Sanchez-Arriaga, G., and Charro, M., Tape-tether design for de-orbiting from given altitude and inclination, to appear in *Proceedings of the 6th European Conference on Space Debris*.

*Book chapters*

1. Sanchez-Torres, A., Radioisotopes - Applications in Physical Sciences. Chapter: Radioisotope Power Systems for Space Applications, *INTECH*, ISBN: 978-953-307-510-5, pp. 457-472, 2011.

Manuscripts with the results in sections 1, 2.4 and 3 are in preparation.

**Contributions to conferences**

1. Sanchez-Torres, A., Sanmartin J.R., and Donoso, J.M., The radiation impedance of electrodynamic tethers in Jupiter, *37th Cospar Scientific Assembly*, Montreal, Canada, July 2008.



2. Bombardelli, C., Sánchez-Torres, A., Charro, M., Sanmartin J.R., and Lorenzini, E.C., A low-orbit, science mission at Jupiter, European Planetary Science Congress, Postdam, Germany, September 13-18, 2009.
3. Sanmartin J. R., Bombardelli, C., and Sanchez-Torres, A., A light tether mission at Jupiter, *SPINE Meeting*, ONERA, Toulouse, September 28-29, 2009.
4. Sanmartin J. R., Sanchez-Torres, A., Bombardelli, C., Charro, M., and Lorenzini, E. C., A Light Tether, Low-Orbit Scientific Mission at Jupiter, *3<sup>rd</sup> Europa Jupiter System Mission (EJSM) Instrument Workshop*, ESA, ESTEC, January 2010.
5. Sanchez-Torres, A. and Sanmartin, J. R. The radiation impedance of a current-carrying conductor in a JUNO-like Jovian orbit, *38th Cospar Scientific Assembly*, Bremen, Germany, July 2010.
6. Sanchez-Torres, A., L. Conde, and Donoso, J. M., The ionization instability of a weakly ionized dusty plasma with grain charge fluctuations, *38th Cospar Scientific Assembly*, Bremen, Germany, July 2010.
7. Sanmartin J. R., Sanchez-Torres, A., and Khan, S. B., Sheath Interference Effects in the Bare-tether Array of an Electric Solar Sail, *11th Spacecraft Charging Technology Conference*, Albuquerque, NM, 20-24 September 2010.
8. Sanmartin J. R. and Sanchez-Torres, A., Tether de-orbiting of satellite at end of mission, *39th COSPAR Scientific Assembly*, Mysore, India, July 14-22, 2012.
9. Sanchez-Torres, A., Propulsive Force in an Electric Solar Sail, *10<sup>th</sup> International Workshop on Electric Probes in Magnetized Plasmas (IWEP2013)*, Madrid, 9-12 July, 2013.

## Collaborations

Contributions in chapter 3, mainly in the orbital perturbation model for de-orbiting satellites at end of mission, were developed during a visit to University of Padova with Prof. E. Lorenzini.



# Abstract

New technological and scientific applications by electrodynamic tethers for planetary missions are analyzed:

i) A set of cylindrical, parallel tethers (electric solar sail or e-sail) is considered for an interplanetary mission; ions from the solar wind are repelled by the high potential of the tether, providing momentum to the e-sail. An approximated model of a stationary potential for a high solar wind flow is considered. With the force provided by a negative biased tether, an indirect method for the optimization trajectory of an Earth-to-Jupiter orbit transfer is analyzed.

ii) The deployment of a tether from the e-sail allows several scientific applications in Jupiter. iia) It might be used as a source of radiative waves for plasma diagnostics and artificial aurora generator. A conductive tether orbiting in the Jovian magnetosphere produces waves. Wave radiation by a conductor carrying a steady current in both a polar, highly eccentric, low perijove orbit, as in NASA's Juno mission, and an equatorial low Jovian orbit (LJO) mission below the intense radiation belts, is considered. Both missions will need electric power generation for scientific instruments and communication systems. Tethers generate power more efficiently than solar panels or radioisotope power systems (RPS). The radiation impedance is required to determine the current in the overall tether circuit. In a cold plasma model, radiation occurs mainly in the Alfvén and fast magnetosonic modes, exhibiting a large refraction index. The radiation impedance of insulated tethers is determined for both modes and either mission. Unlike the Earth ionospheric case, the low-density, highly magnetized Jovian plasma makes the electron gyrofrequency much larger than the plasma frequency; this substantially modifies the power spectrum for either mode by increasing the Alfvén velocity. An estimation of the radiation impedance of bare tethers is also considered. iib) In LJO, a spacecraft orbiting in a slow downward spiral under the radiation belts would allow determining magnetic field structure and atmospheric composition for understanding the

formation, evolution, and structure of Jupiter. Additionally, if the cathodic contactor is switched off, a tether floats electrically, allowing e-beam emission that generate auroras. On/off switching produces bias/current pulses and signal emission, which might be used for Jovian plasma diagnostics. In LJO, the ions impacting against the negative-biased tether do produce secondary electrons, which racing down Jupiter's magnetic field lines, reach the upper atmosphere. The energetic electrons there generate auroral effects. Regions where the tether efficiently should produce secondary electrons are analyzed. iic) Other scientific application suggested in LJO is the in-situ detection of charged grains. Charged grains naturally orbit near Jupiter. High-energy electrons in the Jovian ambient may be modeled by the kappa distribution function. In complex plasma scenarios, where the Jovian high electric field may accelerate charges up superthermal velocities, the use of non-Maxwellian distributions should be considered. In these cases, the distribution tails fit well to a power-law dependence for electrons. Fluctuations of the charged grains for non-Mawellian distribution function are here studied.

iii) The present thesis is concluded with the analysis for de-orbiting satellites at end of mission by electrodynamic tethers. A de-orbit tether system must present very small tether-to-satellite mass ratio and small probability of a tether cut by small debris too. The present work shows how to select tape dimensions so as to minimize the product of those two magnitudes. Preliminary results of tape-tether design are here discussed to minimize that function. Results for de-orbiting Cryosat and Envisat are also presented.

## Resumen

Nuevas aplicaciones tecnológicas y científicas mediante amarras electrodinámicas son analizadas para misiones planetarias.

i) Primero, se considera un conjunto de amarras cilíndricas en paralelo (veleros electrosolares) para una misión interplanetaria. Los iones provenientes del viento solar son repelidos por el alto potencial de dichas amarras generando empuje sobre el velero. Para conocer el intercambio de momento que provocan los iones sobre las amarras se ha considerado un modelo de potencial estacionario. Se ha analizado la transferencia orbital de la Tierra a Júpiter siguiendo un método de optimización de trayectoria indirecto.

ii) Una vez que el velero se encuentra cerca de Júpiter, se ha considerado el despliegue de una amarra para diferentes objetivos científicos. iia) Una amarra podría ser utilizada para diagnóstico de plasmas, al ser una fuente efectiva de ondas, y también como un generador de auroras artificiales. Una amarra conductora que orbite en la magnetosfera jovial es capaz de producir ondas. Se han analizado las diferentes ondas radiadas por un conductor por el que circula una corriente constante que sigue una órbita polar de alta excentricidad y bajo apoápside, como ocurre en la misión Juno de la NASA. iib) Además, se ha estudiado una misión tentativa que sigue una órbita ecuatorial (LJO) por debajo de los intensos cinturones de radiación. Ambas misiones requieren potencia eléctrica para los sistemas de comunicación e instrumentos científicos. Las amarras pueden generar potencia de manera más eficiente que otros sistemas que utilizan paneles solares o sistemas de potencia de radioisótopos (RPS). La impedancia de radiación es necesaria para determinar la corriente que circula por todo el circuito de la amarra. En un modelo de plasma frío, la radiación ocurre principalmente en los modos de Alfvén y magnetosónica rápida, mostrando un elevado índice de refracción. Se ha estudiado la impedancia de radiación en amarras con recubrimiento aislante para los dos modos de radiación y cada una de las misiones. A diferencia del caso ionosférico terrestre, la baja densidad y el intenso campo magnético que aparecen en el entorno de Júpiter consiguen que la girofrecuencia de los electrones sea mucho mayor que la frecuencia del plasma; esto hace que el espectro de potencia para cada modo se modifique substan-

cialmente, aumentando la velocidad de Alfvén. Se ha estimado también la impedancia de radiación para amarras sin aislante conductor. En la misión LJO, un vehículo espacial bajando lentamente la altitud de su órbita permitiría estudiar la estructura del campo magnético y composición atmosférica para entender la formación, evolución, y estructura de Júpiter. Adicionalmente, si el contactor (cátodo) se apaga, se dice que la amarra flota eléctricamente, permitiendo emisión de haz de electrones que generan auroras. El continuo apagado y encendido produce pulsos de corriente dando lugar a emisiones de señales, que pueden ser utilizadas para diagnóstico del plasma jovial. En Órbita Baja Jovial, los iones que impactan contra una amarra polarizada negativamente producen electrones secundarios, que, viajando helicoidalmente sobre las líneas de campo magnético de Júpiter, son capaces de alcanzar su atmósfera más alta, y, de esta manera, generar auroras. Se han identificado cuáles son las regiones donde la amarra sería más eficiente para producir auroras. iic) Otra aplicación científica sugerida para la misión LJO es la detección de granos cargados que orbitan cerca de Júpiter. Los electrones de alta energía en este ambiente pueden ser modelados por una distribución no Maxwelliana conocida como distribución kappa. En escenarios con plasmas complejos, donde los campos eléctricos en Júpiter pueden acelerar las cargas hasta velocidades que superen la velocidad térmica, este tipo de distribuciones son muy útiles. En este caso las colas de las distribuciones de electrones siguen una ley de potencias. Se han estudiado las fluctuaciones de granos cargados para funciones de distribución kappa.

iii) La tesis concluye con el análisis para deorbitar satélites con amarras electrodinámicas que siguen una Órbita Baja Terrestre (LEO). Una amarra debe presentar una baja probabilidad de corte por pequeño *debris* y además debe ser suficientemente ligero para que el cociente entre la masa de la amarra y el satélite sea muy pequeño. En este trabajo se estiman las medidas de la longitud, anchura y espesor que debe tener una amarra para minimizar el producto de la probabilidad de corte por el cociente entre las masas de la amarra y el satélite. Se presentan resultados preliminares del diseño de una amarra con forma de cinta para deorbitar satélites relativamente ligeros como Cryosat y pesados como Envisat.

Las misiones espaciales a planetas exteriores y en el ámbito terrestre plantean importantes retos científico-tecnológicos que deben ser abordados y solucionados. Por ello, desde el inicio de la era espacial se han diseñado novedosos métodos propulsivos, sistemas de guiado, navegación y control más robustos, y nuevos materiales para mejorar el rendimiento de los vehículos espaciales (SC). En un gran número de misiones interplanetarias y en todas las misiones a planetas exteriores se han empleado sistemas de radioisótopos (RPS) para generar potencia eléctrica en los vehículos espaciales y en los rovers de exploración. Estos sistemas emplean como fuente de energía el escaso y costoso plutonio-238. La NASA, por medio de un informe de la *National Academy of Science* (5 de Mayo del 2009), expresó una profunda preocupación por la baja cantidad de plutonio almacenado, insuficiente para desarrollar todas las misiones de exploración planetaria planeadas en el futuro [81, 91]. Esta circunstancia ha llevado a dicha Agencia tomar la decisión de limitar el uso de estos sistemas RPS en algunas misiones de especial interés científico y una recomendación de alta prioridad para que el Congreso de los EEUU apruebe el reestablecimiento de la producción de plutonio-238, -son necesarios cerca de 5 kg de este material radiactivo al año-, para salvaguardar las misiones que requieran dichos sistemas de potencia a partir del año 2018. Por otro lado, la Agencia estadounidense ha estado considerando el uso de fuentes de energía alternativa; como la fisión nuclear a través del ambicioso proyecto Prometheus, para llevar a cabo una misión de exploración en el sistema jovial (JIMO). Finalmente, dicha misión fue desestimada por su elevado coste. Recientemente se han estado desarrollando sistemas que consigan energía a través de los recursos naturales que nos aporta el Sol, mediante paneles solares -poco eficientes para misiones a planetas alejados de la luz solar-. En este contexto, la misión JUNO del programa Nuevas Fronteras de la NASA, cuyo lanzamiento fue realizado con éxito en Agosto de 2011, va a ser la primera misión equipada con paneles solares que sobrevolará Júpiter en el 2015 siguiendo una órbita polar. Anteriormente se habían empleado los antes mencionados RPS para las misiones Pioneer 10,11, Voyager 1,2, Ulysses, Cassini-Huygens y Galileo (todas sobrevuelos excepto Galileo). Dicha misión seguirá una órbita elíptica de alta excentricidad con un periápside muy cercano a Júpiter, y apoápside lejano, evitando que los intensos cinturones de radiación puedan dañar los instrumentos de navegación y científicos.

Un tether o amarra electrodinámica es capaz de operar como sistema propulsivo o generador de potencia, pero también puede ser considerado como solución científico-tecnológica en misiones espaciales tanto en LEO (Órbita Baja Terrestre) como en planetas exteriores. Siguiendo una perspectiva histórica, durante las misiones terrestres TSS-1 (1992) y TSS-1R (1996) se emplearon amarras standard con recubrimiento aislante en toda su longitud, aplicando como terminal anódico pasivo un colector esférico para captar electrones. En una geometría alternativa, propuesta por *J. R. Sanmartín et al.* (1993) [93], se consideró dejar la amarra sin recubrimiento aislante (“bare tether”), y sin colector anódico esférico, de forma que recogiera electrones a lo largo del segmento que resulta polarizado positivo, como si se tratara de una sonda de Langmuir de gran longitud. A diferencia de la amarra standard, el “bare tether” es capaz de recoger electrones a lo largo de una superficie grande ya que este segmento es de varios kilómetros de longitud. Como el radio de la amarra es del orden de la longitud de Debye y pequeño comparado con el radio de Larmor de los electrones, permite una recolección eficiente de electrones en el régimen OML (Orbital Motion Limited) de sondas de Langmuir. La corriente dada por la teoría OML varía en función del perímetro y la longitud. En el caso de una cinta delgada, el perímetro depende de la anchura, que debe ser suficientemente grande para evitar cortes producidos por *debris* y micrometeoritos, y suficientemente pequeño para que la amarra funcione en dicho régimen [95].

En el experimento espacial TSS-1R mencionado anteriormente, se identificó una recolección de corriente más elevada que la que predecía el modelo teórico de Parker-Murphy, debido posiblemente a que se utilizaba un colector esférico de radio bastante mayor que la longitud de Debye [79]. En el caso de una amarra “bare”, que recoge electrones a lo largo de gran parte de su longitud, se puede producir un fenómeno conocido como *atrapamiento adiabático de electrones* (adiabatic electron trapping) [25, 40, 60, 73, 74, 97]. En el caso terrestre (LEO) se da la condición mesotérmica en la que la amarra se mueve con una velocidad muy superior a la velocidad térmica de los iones del ambiente y muy inferior a la velocidad térmica de los electrones. J. Laframboise y L.



Parker [57] mostraron que, para una función de distribución quasi-isotrópica, la densidad de electrones debe entonces ser necesariamente inferior a la densidad ambiente. Por otra parte, debido a su flujo hipersónico y a la alta polarización positiva de la amarra, la densidad de los iones es mayor que la densidad ambiente en una vasta región de la parte “ram” del flujo, violando la condición de cuasi-neutralidad, en una región de dimensión mayor que la longitud de Debye-. La solución a esta paradoja podría basarse en el atrapamiento adiabático de electrones ambiente en órbitas acotadas entorno al tether.

Se pueden señalar los siguientes problemas de ámbito científico-tecnológico que son abordados en la tesis:

#### i) Misión interplanetaria con veleros electrosolares

P. Janhunen [46, 47, 48, 49, 50] propuso un nuevo sistema de propulsión, conocido como *velero electrosolar*, basado en la utilización de la presión dinámica del viento solar sobre una red de amarras. Estos veleros electrosolares tienen la peculiaridad de aprovechar la fuerza de Coulomb sobre la superficie virtual originada por el campo eléctrico de las amarras “bare” para generar empuje. Los iones que provienen del viento solar son desviados por el potencial generado por la amarra, transfiriendo el momento necesario para producir empuje sobre el vehículo espacial. Para que esto ocurra es necesario que el potencial al que se encuentre la amarra sea suficientemente mayor que la energía cinética de los iones [106]. Para evitar el problema del, anteriormente mencionado *efecto ram*, que podría dar lugar al atrapamiento adiabático de electrones en amarras polarizadas positivamente, se ha optado por determinar la fuerza que el viento solar genera sobre amarras polarizadas negativamente. Para determinar correctamente la fuerza es necesario tener un detallado perfil del potencial generado por la amarra. Dicho perfil se ha obtenido con la aproximación de potencial estacionario. De este modo se puede mostrar a qué distancia de la amarra se produce la desviación de los iones existentes en el viento solar, y la cantidad de movimiento que es transferido. Entre las diferentes aplicaciones posibles, se ha optado por estudiar la optimización de trayectoria en una misión interplanetaria entre la Tierra y Júpiter, sometiendo a las amarras

del velero electrosolar diferentes polarizaciones negativas. Generalmente, las misiones espaciales a planetas exteriores llevadas a cabo han utilizado maniobras de asistencia gravitacionales, de manera que se diseña una combinación entre diferentes órbitas en las que el vehículo espacial pasa cerca de un planeta o varios de ellos y es impulsado, -aprovechando la velocidad orbital del planeta-, hasta alcanzar el planeta de destino. El velero electrosolar, en cambio, permite una transferencia directa desde la Tierra hasta otro planeta. Como futuros trabajos, podrían ser objeto de estudio las misiones para la observación de las regiones polares del Sol [70], y misiones a otros planetas [69], de manera que se pueda acortar el tiempo de vuelo admitiendo cargas de pago más pesadas que las sostenidas por los sistemas de propulsión convencionales. La diferencia entre un velero solar y el electrosolar es el modo que tiene de interaccionar el viento solar con la vela para generar empuje. Mientras el velero electrosolar utiliza la presión dinámica del viento solar, los veleros solares recurren a la presión de radiación. Otra diferencia esencial es la variación de la fuerza en función de la distancia en el sistema solar. En el caso del velero solar la fuerza es inversamente proporcional a la distancia al cuadrado, mientras que en el velero electrosolar la variación es inversamente proporcional a la distancia elevada a un exponente que depende del potencial suministrado a las amarras. Generalmente este exponente se ha encontrado cercano a 1, de manera que la fuerza no decae tan rápido con la distancia como en el caso de la vela solar [92].

## ii) Misión científica en Júpiter con una amarra electrodinámica

En las misiones [100, 101] se han estudiado las posibilidades que tiene una amarra para ejecutar una trayectoria de captura en Júpiter, y órbitas que reduzcan el apoápside de forma adecuada para visitar las diferentes lunas galileanas. El problema inmediato que surge en el “tour” lunar es la alta dosis de radiación a la que se somete la amarra al cruzar el intenso cinturón de radiación. En una misión tipo Juno se podría considerar la alternativa del despliegue de un “bare tether” [14] y obtener una potencia bastante elevada para el perfecto funcionamiento de los instrumentos científicos y comunicación, solucionando el problema de la dosis acumulada en las misiones anteriores. En principio,

se conseguiría una potencia eléctrica aceptable con un “bare tether” moderadamente pequeño. En este capítulo de la tesis se han analizado los diferentes modos radiativos que emitirá una amarra orbitando en torno a Júpiter y la generación de auroras artificiales a través de los electrones secundarios emitidos por la amarra. Se ha estudiado también la aparición de inestabilidades en plasmas granulares debido a fluctuaciones en la carga que podemos encontrar en el laboratorio o en diferentes planetas o lunas planetarias.

## ii) Impedancia de radiación de una amarra en Júpiter

El trabajo pionero que llevó a cabo S. D. Drell en 1965 [31], consiguió mostrar que el movimiento de un conductor sobre el plasma es capaz de generar ondas de Alfvén, analizando la impedancia y potencia radiada. En este capítulo se ha mostrado que la impedancia de radiación en LEO, tanto para una amarra con recubrimiento aislante como descubierta, se puede despreciar [94], mientras que la impedancia radiativa  $Z_A \propto V_A$  para una misión tipo JUNO es considerablemente alta [86, 87, 88], debido a que la velocidad de Alfvén,  $V_A$ , es muy alta -cercana a la velocidad de la luz en la zona polar-. Una amarra orbitando en el entorno jovial, sería un importante emisor de ondas a bajas frecuencias, facilitando la posible detección de señales. La obtención de la impedancia radiativa se encuentra ligada a la influencia que puede llegar a tener sobre el circuito resistivo a través de una posible reducción de corriente que circule por el conductor.

En la tesis se ha determinado la impedancia de radiación de una amarra en dos misiones que evitan los intensos cinturones de radiación de Júpiter: la misión JUNO de la NASA (en órbita polar de alta excentricidad y bajo periápside), y para una misión tentativa, en órbita ecuatorial circular, debajo de los cinturones de radiación, ligada a la misión *Europa Jupiter System Mission* (EJSM) de ESA. Se han considerado amarras “bare” y standard (con recubrimiento aislante). Las amarras podrían generar potencia eléctrica, que es algo de extrema necesidad para ciencia planetaria.

Una amarra que conduce corriente de forma continua, emite ondas de Alfvén y mag-

netosónicas rápidas. La potencia radiada depende, en gran medida, de la operatividad del cátodo, con una diferencia de dos órdenes de magnitud si se encuentra encendido o apagado. Si el cátodo se enciende, se producirá un importante aumento tanto en la corriente que circula por la amarra como en la potencia radiada, permitiendo algún tipo de detección fijando una fase de referencia (“phase-locked”). Tras el encendido del cátodo se produce un pulso de polarización/corriente en toda la amarra, que se modelaría como una línea de transmisión.

En lo referente a la emisión de señales, las amarras espaciales permiten la generación de pulsos de radiación. Suponiendo que el cátodo de una amarra está desconectado, los iones son atraídos en gran parte del cable exceptuando una pequeña región donde capturará electrones. Con el cátodo encendido, la amarra recogerá electrones en toda su longitud y se generará un pulso de radiación. En LEO debido a que la impedancia de radiación es baja, cabe esperar que el pulso no altere la potencia total. Sin embargo, en Júpiter, la impedancia de radiación es bastante más alta, y el cociente de masas es algo mayor, modificando dicha potencia. Entre los resultados encontrados cabe destacar que la caída de potencial producida por la emisión de ondas magnetosónicas rápidas por parte de una amarra standard que orbita en Júpiter es entre 30 y 300 veces mayor que en LEO. La impedancia producida por la emisión de ondas de Alfvén en Júpiter es varios órdenes de magnitud mayor que en LEO. En el caso de amarras sin recubrimiento aislante se ha estimado que la impedancia de radiación en Júpiter es reducida, aproximadamente, a la mitad.

#### **iiib) Misión para adquisición de potencia eléctrica y generación de auroras artificiales**

Una vez superados los cinturones de radiación joviales, se propone una misión para adquisición de potencia eléctrica y generación de auroras artificiales, cuando la amarra sin recubrimiento aislante orbite ecuatorialmente y por debajo del *halo* de Júpiter [15], describiendo trayectorias que reduzcan el radio orbital desde las proximidades donde se

produce el máximo de *resonancia de Lorentz* a una distancia de 1.4 radios de Júpiter. Para el estudio se ha analizado las líneas de campo magnético considerando la expansión del potencial en suma de armónicos esféricos cuyos coeficientes vienen recogidos en el modelo VIP4 de la magnetósfera jovial. Los electrones secundarios emitidos tras los impactos de iones  $S^+$ ,  $O^+$  sobre la amarra, con un ángulo ‘pitch’ inferior al *ángulo del cono de pérdidas*, describirían trayectorias helicoidales a lo largo de las líneas de campo, siendo capaces de penetrar en las capas de la atmósfera interior de Júpiter y excitar los gases  $H_2$  y  $He$ , para producir efectos aurorales en un cierto espectro.

Una amarra en órbita baja terrestre (LEO), que disponga de contactor eléctrico operativamente apagado en cualquiera de sus extremos, sería una fuente efectiva de haces de electrones capaz de generar auroras artificiales. Debido a que la corriente desaparece en los extremos de la amarra, y al elevado valor del cociente de masas ión-electrón que existe en el entorno, el tether se encuentra operando con una alta polarización negativa, atrayendo a los iones, en la práctica totalidad de su longitud -condición de “amarra flotando eléctricamente”-, excepto un pequeño segmento polarizado positivamente. Los electrones secundarios liberados tras el impacto de los iones, en gran parte de la longitud de la amarra, son capaces de producir excitaciones sobre los gases  $N_2$ ,  $O$ ,  $O_2$  de la capa E atmosférica, causando emisiones de luz (auroras artificiales) [66, 98], en diferentes longitudes de onda del espectro y a alturas entre 120-150 km. La amarra, equipada con instrumentos de observación, podría analizar en la “huella” del haz de electrones, los perfiles de densidad de las especies neutras dominantes en la termosfera baja, de vital interés para los estudios de simulación numérica de objetos en reentrada. Aprovechando este análisis, se ha realizado para esta tesis, cálculos sencillos para la producción de un haz de electrones capaz de generar auroras artificiales en Júpiter. Una vez analizada la distribución topológica de las líneas de campo magnético en Júpiter, se establecerá si dichas líneas de campo se acercan lo suficiente a la atmósfera joviana, para poder asegurar que la emisión de electrones surgida desde la “amarra en condición eléctricamente flotante”, consiga excitar los gases de dichas zonas y permita la generación de auroras. Además, se ha investigado la generación de potencia de una amarra que orbite ecuatorial y circularmente debajo de los cinturones de radiación [18].

### **ii) Detección de granos de polvo. Análisis de estabilidad en granos cargados y móviles**

Se podría incluir un detector capaz de medir “in situ” la distribución de granos de polvo en la región por debajo del *halo* jovial. Otro aspecto a tratar son los efectos de resonancia de Lorentz sobre los granos de polvo localizados a cierta distancia de Júpiter. Se puede aplicar la teoría OML de sondas sobre éstos, para analizar que efectos producen sobre la amarra. Una amarra equipada con un detector de granos de polvo parecido al de Cassini, sería un importante instrumento de medición de las diferentes propiedades físicas y químicas de éstos, en una región algo desconocida (sólo se disponen de simulaciones numéricas) [105].

Dada la alta actividad energética de la población de electrones e iones en Júpiter, se hace especialmente difícil la determinación de la densidad de corriente en las superficies de un vehículo espacial que viaje alrededor de dicho planeta. Para ello Divine y Garrett consideraron las funciones de distribución kappa para determinar la densidad de electrones y temperatura en el plasma ambiente [27]. Esto puede llevar a plantearse la utilización de dicha función de distribución para analizar posibles fluctuaciones en un entorno con plasma granular [23, 89]. En la presente tesis se presenta un análisis de inestabilidades en un plasmas granular en el que se aprecian granos cargados y móviles. Al incorporar un pequeño movimiento en los granos ligeros se ha observado una pequeña rama de inestabilidad que desaparece cuando se consideran granos más masivos [30].

### **iii) Deorbitación de satélites en LEO mediante amarra electrodinámica**

En la parte final de esta tesis se puede relacionar la evolución de los riesgos que acaecen en la misión jovial considerada anteriormente, como si se tratara de un resultado de eyección de micrometeoritos que surgen al impactar meteoritos sobre las lunas joviales, y de otras colisiones entre partículas que orbitan en los anillos interiores de

Júpiter. En este último capítulo se analizará la aplicación de la amarra para deorbitar satélites en Órbita Baja Terrestre. En la sección anterior sobre la misión para adquisición de potencia eléctrica en Júpiter se ha visto la potencialidad que tiene una amarra para utilizar la fuerza de Lorentz en su beneficio. Por ello, una amarra electrodinámica puede ser de gran utilidad para deorbitar satélites [45] y eliminar la basura espacial, *debris*, en el entorno terrestre. La amarra funcionaría sin consumo de combustible, y no sería necesaria la equipación con paneles solares. Además, sería capaz de generar potencia eléctrica, ayudándose del plasma ambiente y el campo geomagnético. El tiempo necesario para reducir el radio orbital depende de la potencia mecánica disipada por la fuerza de arrastre, la velocidad relativa entre la amarra y el plasma, las masas del planeta Tierra y del objeto destinado a ser deorbitado, y las posiciones de la órbita inicial y final. La fuerza de arrastre se produce a través de la fuerza de Lorentz, cuando la amarra interacciona con el plasma, recogiendo electrones y conduciendo corriente a través de él. Esta fuerza depende de los tamaños característicos del cable, de tal forma que para amarras cortas la *deorbitación* sería más lenta que para cables de mayor longitud, ya que para los primeros la corriente circulante sería más pequeña. Sin embargo, si la caída en altitud es demasiado rápida la probabilidad de que se corte puede ser alta. En esta parte de la tesis se ha analizado la minimización conjunta de la probabilidad de corte y el cociente entre la masas de la amarra y del satélite que se desea deorbitar [107, 108]. Se presentan resultados preliminares del diseño de una amarra con forma de cinta para deorbitar principalmente el satélite Cryosat. Actualmente existe un satélite meteorológico de más de 8 toneladas, conocido como Envisat, que se encuentra orbitando entorno a la Tierra a una altitud cercana a los 780 km. Brevemente se darán los resultados para deorbitar dicho satélite con una amarra electrodinámica, y se compararán con una estrategia de deorbitado mediante cohete de propulsión sólida.





# CHAPTER 1

## INTERPLANETARY MISSION WITH AN ELECTRIC SOLAR SAIL

### 1.1 Introduction

Many alternatives to reach outer planets have been studied during decades. Most of the missions have used gravity assists to reach such large distances. One suggested method is the deployment of a solar sail which is capable to produce thrust with the absorbed and reflected solar photons. Other suggested method by Zubrin [120] is through the use of magnetic sails deploying a superconducting magnet with very large radius (in the 100-200 km range) to procure accelerations of about  $0.01 \text{ ms}^{-2}$ . Winglee [118] proposed a mini-magnetospheric, bubble-like sail providing thrust from the dynamic pressure of the solar wind; i.e. the particles are repelled by its self-generated magnetic field.

Alfven was the first to consider an insulated conducting tether for generating propulsion for interplanetary travel by using the electromagnetic interaction with the Sun's magnetic field [1]. An insulated conducting tether, connected to a spacecraft and terminated at both ends by plasma contactors, provides propulsion in two ways: i) the current induced in the tether by the interplanetary magnetic field may be used to power ion thruster; ii) tether does interact with the magnetic field, producing thrust or drag. Since the magnetic field of the solar wind is very low for practical interplanetary mission, the system proposed by Alfven in 1972 would require a very large superconducting wire ( $\sim 1000 \text{ km}$ ) to generate about 1000 A.

An electric solar sail (e-sail) is a promising propellantless propulsion concept for the exploration of the Solar System [46, 47, 48, 49, 50]. An e-sail consists of an array of bare conductive tethers at very high positive/negative bias, capable of extracting solar-wind momentum by Coulomb deflection of protons. The present work focuses on the negative-bias case with a potential profile that must be correctly modeled. Ion scattering does occur at some point of the profile and the resulting thrust are determined; that thrust scales slower with distance to the Sun, than it was previously suggested in the literature [47, 48, 49, 50]. Possible interference effects in a tether array for both starfish-like and parallel designs, are briefly discussed. Finally, as trajectory optimization example, an optimal orbit transfer from Earth to Jupiter is considered.

Electric solar sail (e-sail) uses bare wires in a new technology application, which involves Coulomb forces on charges instead of Lorentz forces on currents [48]. An e-sail requires Coulomb drag calculations under intriguing conditions. Early crude calculations of Coulomb drag on Low Earth Orbit (LEO) satellites at relative motion with respect to the ambient plasma,  $v_{rel} (\equiv v_{orb} - v_{pl})$ , involves i) satellites in mesothermal flow, i.e. moving subsonic and supersonic with respect to electrons and ions, respectively; ii) complex geometries with 3D-Radius  $R$  large compared with the Debye length  $\lambda_D$ ; and iii) satellites at negative bias  $\Phi_p$ , following the floating probe condition, with  $-e\Phi_p$  is a few times  $kT_e$ .

Satellites orbiting in Medium Earth Orbit (MEO), such as LAGEOS I and II, could float positive because of photoelectron emission, which is dependent on weak solar light but independent of ambient plasma density, thus becoming relevant at low enough plasma density; two-dimensional geometry involved tin/copper dipoles a few centimeters long, which were dropped in MEO in the early 60's. Coulomb drag is also determinant in evolution of formation-flying satellites and grains in dusty plasmas, in a variety of parameter ranges [54, 55]. A new application for Radiation Belts Remediation will use space tethers at high bias to effectively scatter the high-energy electrons in the Belts, in the sheath layer produced by them [24].

An e-sail will use the dynamic pressure of the solar wind for propulsion [48]. Standard solar sails use a physical membrane whereas e-sails would use a bare-tether array to set

up a virtual sail (see Fig. 1.1). IKAROS, the first solar sail mission, was launched by the Japanese Space Agency (JAXA) on May 21, 2010, deploying a 14 m side square sail. The weight of the thin ( $7.5 \mu\text{m}$ ) membrane is 15 kg, including 2 kg for the four tip masses at corners of the sail. The material used is a synthetic polymeric resin called polyimide, with aluminum coating to make it capable of supporting very high temperatures. This assures an areal density, which is defined as total material mass divided by material area, as low as  $10 \text{ g/m}^2$ . The thin-film solar cells that cover some surface area of the membrane and the tip masses increase substantially the total areal density to about  $76 \text{ g/m}^2$ . NASA recently launched a small solar sail ( $\sim 10 \text{ m}$  side square sail) called NanoSail-D in LEO on January 20, 2011. Future NASA missions such as Heliostorm, Solar Polar Imager, and Interstellar Probe will be solar sail with larger membrane size ( $\sim 200 \text{ m}$  side square sail). The material used for the design of the thin sail membrane might be Mylar coated with aluminium, aluminized Kapton, aluminized Polyimide, or carbon nanotubes.

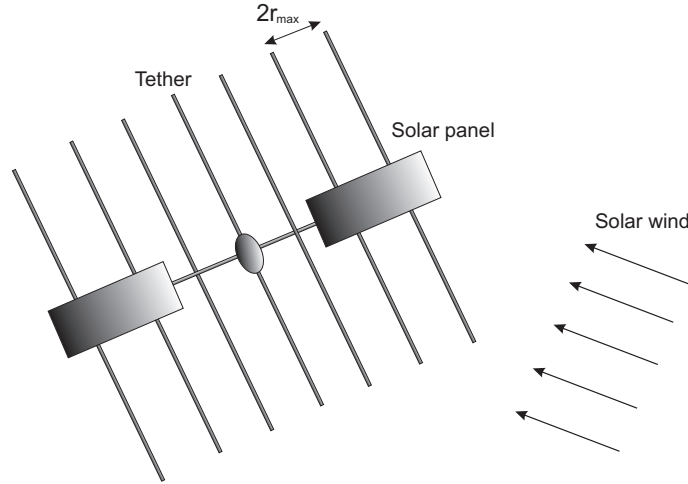


Figure 1.1: Schematic description of the electric solar sail for a set of parallel tethers. Solar panels keeps the tether at high bias. For positive (negative) bias, the ions will be scattered (collected).

At 1 astronomical unit (AU) the photon pressure is 3 orders of magnitude larger than the dynamic pressure in the solar wind,

$$P_{\text{dyn}} \approx n_{\infty} m_i v_{sw}^2 \sim 2 \times 10^{-9} \text{ N/m}^2, \quad P_{\text{phot}} \approx 4.563 \left( \frac{1 \text{ AU}}{r_{sc}} \right)^2 \frac{\mu\text{N}}{\text{m}^2}, \quad (1.1)$$

with a solar constant

$$S_c \equiv P_{phot} \times c \approx 1.27 \text{ kW/m}^2, \quad (1.2)$$

where  $r_{sc}$  is distance between Sun and spacecraft (SC) and  $c$  is the light velocity. However, an e-sail may have a (virtual) effective area per unit mass much larger than a standard sail membrane; the e-sail thrust might be comparatively much larger. Solar wind conditions at 1 AU, quite different from LEO conditions, make Coulomb forces dominant. The ESTCube-1 test mission for e-sail concept was recently launched on 7 May 2013. The mission will validate tether deployment and measure the force produced in a polar or equatorial Earth orbit (LEO).

A review of the ambient solar wind conditions as compared to LEO is presented in section 1.2. In section 1.3, the potential profile of the tether is determined. In section 1.4 we study the forces acting on the e-sail, showing that the Coulomb-to-Lorentz force ratio for a tether at 1 AU would be very large; the electrical power required for maintaining tethers at high bias is also considered. The ion scattering problem in that potential profile and the resulting force on the tether are studied in section 1.5. In section 1.6, we briefly comment on possible sheath-interference effects in an e-sail for both parallel and starfish-like design. An optimization trajectory for an orbit transfer from Earth to Jupiter is presented in section 1.7. Discussions are presented in section 1.8.

## 1.2 Ambient Solar Wind conditions

Typical values for the ambient plasma at 1 AU in the ecliptic plane are  $T_e \sim 12 \text{ eV}$ ,  $B \sim 10^{-8} \text{ T}$ ,  $n_\infty \sim 7 \text{ cm}^{-3}$ ,  $v_{sw} = 400 \text{ km/s}$ . The prevalent ion species in the solar wind is  $H^+$ . Density models [62] become simply  $n_\infty \propto 1/r_{sc}^2$  beyond 1 AU

$$n_\infty \approx 7.2 \left( \frac{1\text{AU}}{r_{sc}} \right)^2 + 1.95 \cdot 10^{-3} \left( \frac{1\text{AU}}{r_{sc}} \right)^4 + 8.1 \cdot 10^{-7} \left( \frac{1\text{AU}}{r_{sc}} \right)^6 \text{ cm}^{-3}. \quad (1.3)$$

In a simple isothermal outflow Parker model [78], the solar wind velocity increases slowly with distance from the Sun as  $\propto \sqrt{\ln r_{sc}}$ . At 1 AU, it is about two orders of magnitude greater than orbital velocity in LEO. In-situ observations have established that the solar wind velocity increases from  $\sim 400 \text{ km/s}$  at ecliptic plane (slow solar wind) up to  $\sim 700 \text{ km/s}$  at polar latitudes (fast wind).

Different rough  $T_e$  models [71] may be used beyond 1 AU. For the slow wind model we have

$$T_e \approx 3.8 \left[ 1 + 1.5 \left( \frac{1 \text{ AU}}{r_{sc}} \right)^{4/3} \right] eV, \quad (1.4)$$

$$T_e \approx 12 \times \left( \frac{1 \text{ AU}}{r_{sc}} \right)^{1/3} eV, \quad (1.5)$$

whereas for fast wind streams, we have

$$T_e \approx 25 \left[ 1 + 0.55 \left( \frac{1 \text{ AU}}{r_{sc}} \right)^{4/3} \right] eV. \quad (1.6)$$

As shown in the next section, discussing Coulomb and Lorentz forces involves two lengths,  $\lambda_D$  and  $v_{rel}/\Omega_i$ , which need be compared to tether radius  $R$  and length  $L$ , respectively;  $\Omega_i$  is the ion gyrofrequency,  $eB/m_i$ . The dimensionless ratio  $\Omega_i L/v_{rel}$  will be typically small at 1 AU and large in LEO. The dimensionless ratio  $\lambda_D/R$  will be typically of order unity in LEO and large at 1 AU. A summary of typical values for the ambient plasma and characteristics lengths is presented in Table 1.1.

| Localization | $v_{rel}$ (km/s) | B (G)     | Species        | $T_e$ (eV) | $n_\infty$ (cm <sup>-3</sup> ) | $v_{rel}/\Omega_i$ (m) | $\lambda_D$ (m)    |
|--------------|------------------|-----------|----------------|------------|--------------------------------|------------------------|--------------------|
| LEO          | 8                | 0.3       | O <sup>+</sup> | 0.15       | $10^5 - 10^6$                  | $10^2$                 | $5 \times 10^{-3}$ |
| 1 AU         | 400              | $10^{-4}$ | H <sup>+</sup> | 12         | 7.2                            | $10^6$                 | 10                 |

Table 1.1: Typical values for the ambient plasma and characteristic lengths.

The mesothermal condition ( $v_{ti} \ll v_{rel} \ll v_{te}$ ) occurs at 1 AU and in LEO. Since  $v_{rel} \approx v_{sw} \ll v_{te}$  the solar wind electrons are isotropic for the positive potential case; a fraction of electrons in the distribution have zero velocities. For a negative bias, we have  $v_{ti} \ll v_{rel} \approx v_{sw}$  and non trapped ions are expected in the potential structure.

Several profiles are needed for the correct evaluation of the optimization trajectory. Equations (1.3) and (1.5) give both density and temperature profiles. Simple Parker's model is used to determine the solar wind velocity [78]. Eugene Parker realized the solar corona may act like a De-Laval nozzle; considering the acceleration of a fluid down a converging tube: a density gradient will act like the converging phase and spherical expansion like the diverging stage. The stationary expansion of the solar

corona considering spherical symmetry, satisfies the equations of motion and continuity,

$$\rho v_{sw} \frac{dv_{sw}}{dr} = -\frac{dp}{dr} - \frac{\mu_{\odot} \rho}{r^2}, \quad (1.7)$$

$$\frac{d}{dr} (r^2 \rho v_{sw}) = 0, \quad (1.8)$$

where  $\mu_{\odot}$  is the Sun's gravitational constant. For an ideal gas at temperature  $T_0$  in the Sun's corona, the sound velocity is  $c_s = \sqrt{kT_0/M_{\odot}}$ , being  $M_{\odot}$  the Sun's mass. Introducing  $c_s = \sqrt{p/\rho}$ , equation (1.7) reads

$$v_{sw} \frac{dv_{sw}}{dr} = -c_s^2 \frac{d\rho}{\rho dr} - \frac{\mu_{\odot}}{r^2}. \quad (1.9)$$

With equation (1.8) we have

$$v_{sw} \frac{dv_{sw}}{dr} = -c_s^2 r^2 v_{sw} \frac{d}{dr} \left( \frac{1}{r^2 v_{sw}} \right) - \frac{\mu_{\odot}}{r^2}. \quad (1.10)$$

Carrying out the derivatives and simplifying equation (1.10) we have

$$\left( v_{sw} - \frac{c_s^2}{v_{sw}} \right) \frac{dv_{sw}}{dr} = \frac{2c_s^2}{r^2} (r - r_c), \quad r_c = \frac{\mu_{\odot}}{2c_s^2}. \quad (1.11)$$

The solar wind flow reaches the sound velocity when the plasma reaches the critical distance  $r_c$ . The solution proposed by Parker passes just through the critical point and produces a supersonic flow,

$$\frac{v_{sw}^2}{c_s^2} - \ln \frac{v_{sw}^2}{c_s^2} = 4 \ln \frac{r}{r_c} + 4 \frac{r_c}{r} - 3 \quad (1.12)$$

For  $r \gg r_c$  the solar wind velocity is  $v_{sw} \approx 2c_s \sqrt{\ln r/r_c}$ . Other complex models might be used for a detailed calculation [64, 109, 112, 114].

### 1.3 Potential profile of a single tether

A simple approximation of symmetric potential profiles, which are exact for the infinite-cylinder stationary (nonmoving) case, is here considered. For a negative polarity electric sail, tethers attract ions and repels electrons from the solar wind. We follow the works of Sanmartin and Estes [95] for positive-biased probe and Choiniere for negative-polarized case [20, 21]. The determination of ion trajectories to obtain the potential profile  $\Phi(r)$  for wire bias  $\Phi_p$ , requires solving Poisson's equation,

$$\frac{\lambda_{De}^2}{r} \frac{d}{dr} \left( r \frac{d}{dr} \frac{e|\Phi|}{kT_e} \right) = \frac{n_i}{n_{\infty}} - \frac{n_e}{n_{\infty}} \quad (1.13)$$

with boundary conditions  $\Phi(r = R) = \Phi_p$  and  $\Phi \rightarrow 0$  as  $r \rightarrow \infty$ . Since  $e|\Phi_p| \gg kT_i, kT_e$  the normalized electron density  $N_e \equiv n_e/n_\infty$  for repelled-particle gives the simple Boltzmann law,

$$N_e \approx \exp\left(-\frac{e|\Phi|}{kT_e}\right). \quad (1.14)$$

Several works considered a current model to a moving cylindrical probe [44, 51, 58, 110, 113]. Following the work of Goddard and Laframboise [37], the ion distribution function for an ion bulk flow moving parallel to the tether velocity reads

$$f_i = \frac{n_i m_i}{2\pi kT_i} \exp\left[-\frac{E}{kT_i} + 2S\sqrt{\frac{E}{kT_i}} - S^2\right], \quad S \equiv \frac{v_{sw}}{\sqrt{2kT_i/m_i}}. \quad (1.15)$$

Considering that the angular momentum  $J_r$  is conserved, the normalized ion density  $N_i \equiv n_i/n_\infty$  may be then roughly approximated as

$$N_i = \frac{e^{-S^2}}{\pi} \int_{E_{\min}}^{\infty} \frac{dE}{kT_i} \exp\left(-\frac{E}{kT_i} + 2\sqrt{\frac{E}{kT_i}}S\right) \times \left[2 \sin^{-1} \frac{J_r^*(E)}{J_r(E)} \sin^{-1} \frac{J_R^*(E)}{J_r(E)}\right], \quad (1.16)$$

where  $J_r(E) \equiv \sqrt{2m_i r^2 [E - e|\Phi(r)|]}$  is conserved for  $E \geq e|\Phi|$ , and  $J_r^*(E) = \min\{J_{r'}(E); \quad r \leq r' < \infty\}$ . The definite integral is limited by  $E_{\min} = \max(0, \max\{e|\Phi(r')|; \quad r \leq r' < \infty\})$ . Notice that  $J_r$  vanishes in the numerical integration for  $E < e|\Phi|$ .

The system equations given by (1.13)-(1.16), which determines the potential profile, are numerically solved with an algorithm similar implemented in references [20],[21] and [85]. The integrand in equation (1.16) is carried out with a trapezoidal quadrature algorithm. Since  $R \leq r < \infty$  the method truncates in a finite domain  $R \leq r < r_{\max}$ . One may choose the appropriate  $r_{\max}$  value for each  $\Phi_p$ . Since  $R \sim 20 \mu m$  and  $r_{\max} \gg \lambda_{De} \sim 10$  m, the very large interval  $[R, r_{\max}]$  and the potential are discretized with  $N$  points not equally spaced. The potential  $\Phi$  at the mesh point is found by looking with a Newton method for the zero of a vector-function of components  $\mathcal{F}_i(\Phi) = \Phi_i - \tilde{\Phi}_i$  and  $\Phi_i = \Phi(r = r_i)$  for  $i = 0, \dots, N$ . Trying with an initial potential profile  $\Phi_i$ , the ion density is calculated with Eq. (1.16). This readily finds the new potential  $\tilde{\Phi}$  by solving Poisson's equation (1.13) and imposing boundary conditions  $\tilde{\Phi}(R) = \Phi_p$  and  $\tilde{\Phi} \sim 1/r$  at  $r_{\max}$ . As example, Figure 1.2 shows the profiles of potential and both electron and ion density for  $|\Phi_p| = 20$  kV,  $R = 20 \mu m$  and the ambient conditions at 1 AU.

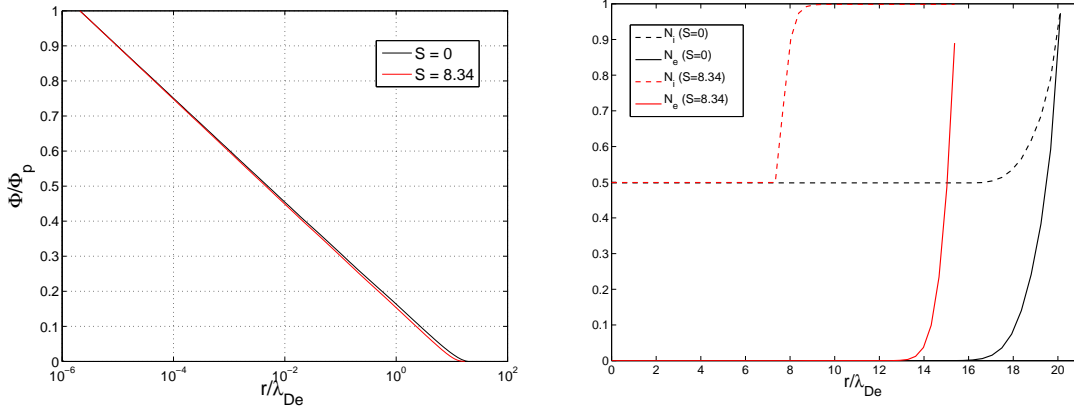


Figure 1.2: Profiles of potential (left) and electron/ion densities (right) for  $|\Phi_p| = 20$  kV,  $R = 20 \mu\text{m}$  and the ambient conditions at 1 AU. Both profiles are illustrated for  $S = 0$  (black line) and  $S = 8.34$  (red line). Notice that  $N_i \simeq n_i/N_\infty$  and  $N_e \simeq n_e/N_\infty$ .

Left figure in Figure 1.2 shows that the potential range is larger for  $S = 0$ . The profile at the right figure on Figure 1.2 shows a similar behavior for both electron and ion density as it is found by McMahon et.al. (see Figure 2 in reference [68]), where ions reach the  $N_i \approx 1$  condition much faster than electrons for ion flow. As consequence, the quasi-neutrality condition occurs in a shorter distance for the large ion flow stream at 1AU ( $S = 8.34$ ). Similar behavior is realized for the 1-6 AU applicable range of the Earth-to-Jupiter orbit transfer considered in section 1.7.

## 1.4 Coulomb-to-Lorentz force ratio

The Coulomb force on an e-sail wire is thrust because the solar wind overtakes the sail. Originally, wire bias  $\Phi_p$  was set positive but a negative bias allows for thrust too [49]. A negative bias illustrates the basic characteristics of the e-sail. The Coulomb force is then made of two contributions to momentum transfer, from i) ions that reach the wire,  $F_{\text{coll}}$ , and ii) ions that orbit within the sheath and escape,  $F_{\text{orb}}$ . For the e-sail we will have  $F_{\text{orb}} \gg F_{\text{coll}}$  because the sheath is very large assuming high bias and ratio  $\lambda_D/R \gg 1$ . Further,  $F_{\text{coll}}$ , is just the OML ion current multiplied by the incident momentum per unit charge [106],

$$F_{\text{coll}} = I_{\text{coll}} \times \frac{m_i v_{\text{rel}}}{e}, \quad I_{\text{coll}} (\text{OML}) \approx 2RL \times en_\infty \sqrt{2e |\Phi_p| / m_i}, \quad (1.17)$$



while the Lorentz force is  $F_L \sim I_{av}LB$ , with the average current  $I_{av}$  comparable to  $I_{coll}$ . The collected-to-Lorentz force ratio is then

$$\frac{F_{coll}}{F_L} \approx \frac{v_{rel}}{\Omega_i L} \gg 1. \quad (1.18)$$

Considering both ion contributions, the Coulomb force can be estimated as proportional to both frontal area and dynamic pressure

$$F_c \propto 2r_{max}L \times n_{\infty}m_i v_{rel}^2. \quad (1.19)$$

With the plasma conditions considered here at 1 AU we have  $r_{max} \gg \lambda_D$ . Assuming a round wire and positive bias,  $\Phi_p > 0$ , the Lorentz force on the average current  $I_{av}$  reads

$$F_L \sim \frac{1}{2}2RL \times en_{\infty} \sqrt{\frac{2e\Phi_p}{m_e}} \times LB, \quad (1.20)$$

where bias has been taken uniform, and arising from solar panels, because the very small magnetic field at 1 AU induces a negligible motional electric field,  $E_m = v_{rel} \times B$ .

The Coulomb-to-Lorentz force ratio will then read

$$\frac{F_c}{F_L} \propto \frac{v_{rel}}{\Omega_i L} \frac{\lambda_D}{R} \frac{r_{max}}{\lambda_D} \sqrt{\frac{m_e}{m_i}} \sqrt{\frac{m_i v_{rel}^2/2}{e\Phi_p}}. \quad (1.21)$$

In LEO, both ratios  $v_{rel}/\Omega_i L$  and  $m_i v_{rel}^2/2e\Phi_p$  are small, and  $\lambda_D/R$  is of order unity. At 1 AU both ratios  $v_{rel}/\Omega_i L$  and  $\lambda_D/R$  are large, whereas  $m_i v_{rel}^2/2e\Phi_p$  should be just small for an effective ion scattering. Ratios  $r_{max}/\lambda_D$  and  $m_e/m_i$  are similarly large and small, respectively, in both LEO and 1 AU. The Coulomb force, determined by a front-area, is then dominant at 1 AU, whereas it is negligible in LEO. In the  $\Phi_p < 0$  case, the Lorentz force in Eq. (1.20) is reduced in the ratio  $\sqrt{m_e/m_i}$ , making the Coulomb-to-Lorentz force in Eq. (1.21) to increase in the inverse of that ratio, with  $|\Phi_p|$  replacing  $\Phi_p$  in Eq. (1.21). Since the current reaching the power source is  $I_{max} = 2I_{av} \propto n_{\infty} \sqrt{|\Phi_p|}$ , the power required for a given bias is

$$\dot{W} = I_{max} |\Phi_p| \propto n_{\infty} |\Phi_p| \sqrt{|\Phi_p|}. \quad (1.22)$$

With solar panels in the spacecraft providing the electric power required to keep tethers at high bias, generated power depends on both the area  $A$  of panels, and the solar constant  $S_c$  of equation (1.2), yielding

$$\dot{W} \propto A \times S_c. \quad (1.23)$$

Since  $\dot{W} \propto S_c$ , and  $S_c$  and  $N_e$  itself, vary with distance to the Sun as  $1/r_{sc}^2$ , tether bias,  $\Phi_p \propto \left(\dot{W}/n_\infty\right)^{2/3}$ , is independent of distance  $r_{sc}$ . Ratio  $2e|\Phi_p|/m_i v_{rel}^2$ , and propulsive efficiency might keep constant with increasing  $r_{sc}$  if the SC velocity increases along with  $v_{sw}$ .

The current collection from a sunlit spacecraft in low-density plasma ambient is usually affected by emission of photoelectrons from its surface. A conductive tether emits photoelectrons when a photon of energy  $hc/\lambda$  is absorbed by its surface, where  $h$  and  $\lambda$  are Planck's constant and wavelength of the photon, respectively. The energy of the emitted photoelectrons is  $E = hc/\lambda - W_f \approx 1240 [\text{eV} \cdot \text{nm}]/\lambda[\text{nm}] - W_f$ , where  $W_f$  is the work function of the material at surface. For an aluminum tether ( $W_f = 4.2 \text{ eV}$ ) only radiation of  $\lambda < 295 \text{ nm}$  might produce photoelectrons. In such short wavelength range, the Sun does emit mostly UV radiation, and soft x-rays with a very low intensity. For high-energy photons emitted by the Sun we have  $4.2 \text{ eV} < E < 1.24 \text{ keV} \ll e|\Phi_p|$ . For tethers at high positive bias, photoelectrons have no enough energy to overtake the potential. Photoelectrons will be attracted back to the tether, without generating additional current. For a negative-biased tether, however, photoelectrons are scattered, contributing to the current gathered. Grad (1973) estimated the photoelectron emission at 1 AU from several materials [38]; for aluminum oxide the photoelectron current is about  $42 \mu\text{A m}^{-2} \times 2R \times (1 \text{ AU}/r_{sc})^2$  per unit length.

## 1.5 Ion scattering and Coulomb force calculations

The momentum exchanged between solar wind ions and the tether determines the Coulomb force. We first analyze the deflection of a single particle of mass  $m_i$  moving in a field  $\Phi(r)$  whose center is at rest. The classical scattering problem is represented in Fig. 1.3, where the deflection angle is  $\chi = \pi - 2\delta$ , where

$$\delta = \rho \int_{r_{\min}}^{\infty} \frac{dr}{r^2 \sqrt{1 - U_{eff}(r)}}, \quad U_{eff} = \frac{\rho^2}{r^2} + \frac{e|\Phi(r)|}{E_{sw}}, \quad (1.24)$$

$\rho$  is the impact parameter,  $E_{sw} = m_i v_{sw}^2/2$ , and  $r_{\min}$ , is the closest approach to the center, which is determined from equation  $U_{eff}(r_{\min}) = 1$ .

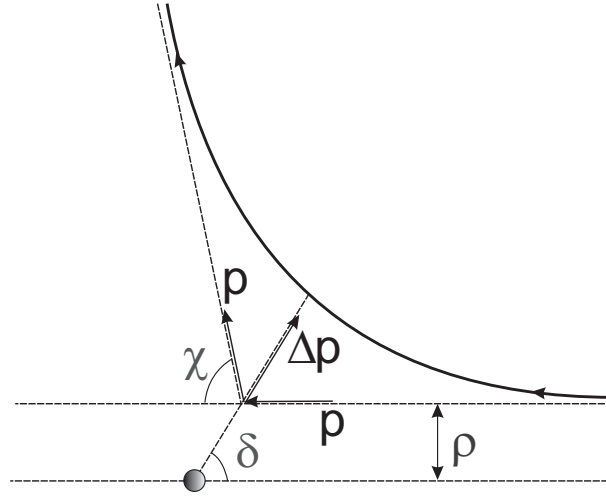


Figure 1.3: Ion scattering under the action of the potential generated by a single tether. Notice that  $\chi + 2\delta = \pi$ ,  $\rho$  is the impact parameter and  $\chi$  is the deflection angle. We assume same initial and final momentum  $p$  of the particle.

From classical considerations for scattering in a central field in Fig. 1.3, the exchanged momentum is  $\Delta p = p \sin \chi / \sin \delta$ . Since  $\chi + 2\delta = \pi$  and  $p = m_i v_{sw}$ , the exchanged momentum reads  $\Delta p = 2m_i v_{sw} \sin(\chi/2)$ . The force per unit tether length then reads

$$\frac{F_c}{L} = n_{\infty} v_{sw} \times 2 \int_0^{r_{\max}} 2m_i v_{sw} \sin[\chi(\rho)/2] d\rho = 4P_{dyn} \int_0^{r_{\max}} \sin(\chi/2) d\rho, \quad (1.25)$$

where  $r_{\max}$  is the maximum distance reached for the potential  $\Phi_p$ . Calculating equation (1.25) numerically, the force per unit length versus distance for several  $\Phi_p$  values is presented in Figure 1.4. A thrust per length of about  $500 \text{ nN/m}$  was estimated by Janhunen for a 20 kV charged tether of  $L = 20 \text{ km}$  and  $R = 25 \text{ }\mu\text{m}$  with the ambient condition at 1 AU. Our results show lower thrust for ion flow stream; near one forth of the thrust given in reference [50].

## 1.6 Interference effects in an e-sail

Interference in sheath-structure may occur within a tether array [96]. Interference effects depends on the e-sail design. In a parallel tether array,  $N_t$  tethers are separated a distance of  $2r_{\max}$  to avoid the superposition of both potentials (Figure 1.1).

In a starfish,  $N_t$  tethers meet at the spacecraft/power system. At the opposite ends,

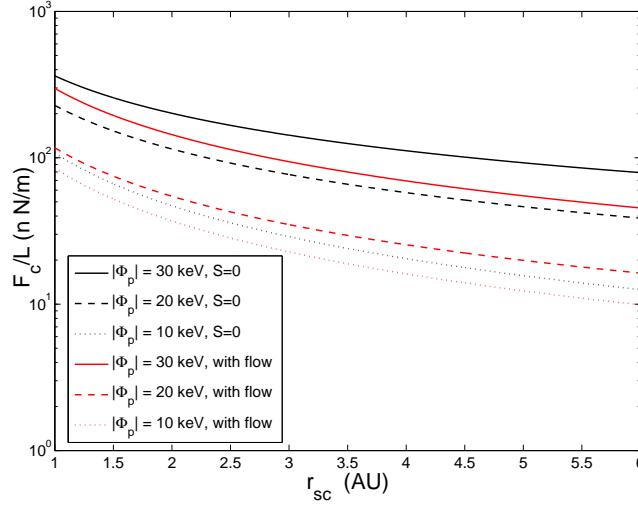


Figure 1.4: Force per unit tether length versus distance from the Sun for several  $\Phi_p$  considering flow and  $S = 0$ . Notice that the ion flow reduce the force per unit length.

the potential of adjacent tethers are assumed to just not overlap (Figure 1.5). The number,  $N_t$ , of tethers deployed for obtaining the largest, circle, front-area possible using this symmetry, must be

$$N_t = \frac{\pi}{\gamma} \approx \pi \frac{L}{r_{\max}}, \quad (1.26)$$

where  $\gamma = \tan^{-1}(r_{\max}/L)$ . Since  $L \gg r_{\max}$ , the number of tethers would be very large.

Notice that potentials will strongly interfere at points closer to the spacecraft. Also, a parallel array has a mass per unit area  $\rho_t \pi R^2 / 2r_{\max}$ , where  $\rho_t$  is the tether density, whereas the value for the starfish-like configuration is  $\rho_t \pi R^2 / r_{\max}$ . Clearly, a parallel array performs better than a starfish array in two respects. First, the parallel array has half the mass per unit area. Secondly, sheath interference is strong over most of the starfish-array circle.

## 1.7 Earth-to-Jupiter orbit transfer

An e-sail might be used for flyby towards outer planets. As example, an optimal interplanetary trajectory from Earth to Jupiter is determined for minimum time transfer. A set of parallel, cylindrical tethers and no interference effects among them is assumed. Since the e-sail does not work inside the Jovian magnetosphere, which reaches about

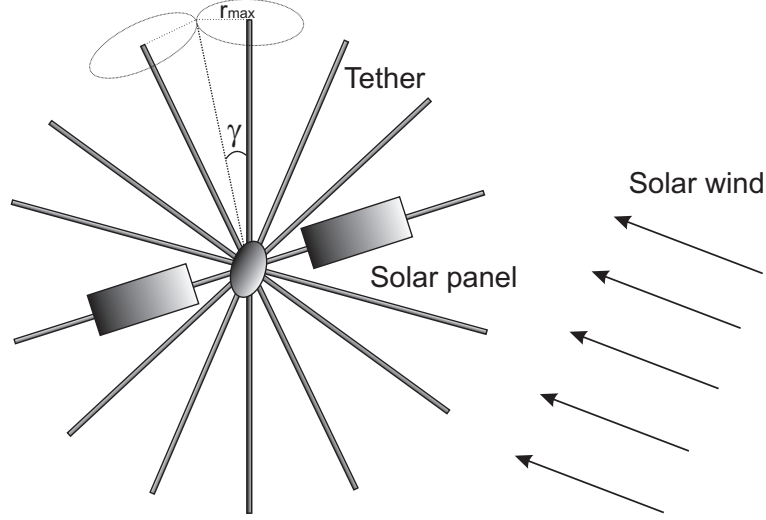


Figure 1.5: In Starfish-like design, since  $L \gg r_{max}$  the number of tethers required must be very large.

100 Jupiter's radius, some high-thrust propulsion system may be added to the e-sail for the capture phase. Capture by a single, fast rotating tether in parabolic orbit is shown in reference [100]. Since the ecliptic inclination is about 1.3 deg and the Jovian orbit eccentricity is small ( $e \approx 0.048$ ), an orbit transfer between two circular, coplanar orbits is assumed. Following Mengali and Quarta, (2011) a two-dimensional model for a heliocentric polar inertial plane is now considered [80],

$$\dot{r}_{sc} = u, \quad (1.27)$$

$$\dot{\theta} = \frac{v}{r_{sc}}, \quad (1.28)$$

$$\dot{u} = \frac{v^2}{r_{sc}} - \frac{\mu_{\odot}}{r_{sc}^2} + a\tau \cos \alpha \times \left( \frac{1\text{AU}}{r_{sc}} \right)^{\beta}, \quad (1.29)$$

$$\dot{v} = -\frac{uv}{r_{sc}} + a\tau \sin \alpha \times \left( \frac{1\text{AU}}{r_{sc}} \right)^{\beta}, \quad (1.30)$$

where  $\mu_{\odot}$  is the Sun's gravitational constant,  $r_{sc}$  is the Sun-sailcraft distance,  $\theta$  is the polar angle,  $u$  and  $v$  are the radial and transverse components of velocity,  $\beta$  is the power law, which is approximately given by the force profiles in Figure 1.4. The sail acceleration  $a$  is given by  $F_c N_t L / (m_t + m_{pay})$ , being  $m_{pay}$  and  $m_t$  the masses of payload and tether, respectively,  $N_t$  is the number of tethers and  $L$  their lengths. Since it is assumed an orbit transfer from two circular coplanar orbits, the initial conditions for

the state variables are

$$r_{sc}(t_0) = r_e, \quad \theta(t_0) = u(t_0) = 0, \quad v(t_0) = \sqrt{\mu_\odot/r_e}, \quad (1.31)$$

where  $r_e$  is the distance from Sun to Earth, which is equal to 1 AU. A minimum flight time  $t_f$  problem is solved by the Hamiltonian

$$H = \lambda_{r_{sc}} u + \lambda_\theta \frac{v}{r_{sc}} + \lambda_u \left( \frac{v^2}{r_{sc}^2} - \frac{\mu_\odot}{r_{sc}^3} \right) - \lambda_v \frac{uv}{r_{sc}} + H_0, \quad (1.32)$$

where  $\lambda_{r_{sc}}$ ,  $\lambda_\theta$ ,  $\lambda_u$  and  $\lambda_v$  are the adjoint variables associates with the state variables  $r_{sc}$ ,  $\theta$ ,  $u$ , and  $v$ , respectively. The term  $H_0$  explicitly depends on the control  $(\tau, \alpha)$  variables,

$$H_0 \equiv a\tau (\lambda_u \cos \alpha + \lambda_v \sin \alpha) \left( \frac{r_e}{r_{sc}} \right)^\beta, \quad (1.33)$$

where the power law given by  $\beta$  is approximately determined with the variation of thrust versus distance (see Figure 1.4). Optimal control law is derived with the Euler-Lagrange equations for the adjoint variables,

$$\dot{\lambda}_{r_{sc}} = -\frac{\partial H}{\partial r_{sc}} = \frac{\lambda_\theta v}{r_{sc}^2} + \lambda_u \left( \frac{v^2}{r_{sc}^2} - \frac{2\mu_\odot}{r_{sc}^3} \right) - \lambda_v \frac{uv}{r_{sc}^2} + \beta \frac{H_0}{r_{sc}}, \quad (1.34)$$

$$\dot{\lambda}_\theta = -\frac{\partial H}{\partial \theta} = 0, \quad (1.35)$$

$$\dot{\lambda}_u = -\frac{\partial H}{\partial u} = -\lambda_{r_{sc}} + \lambda_v \frac{v}{r_{sc}}, \quad (1.36)$$

$$\dot{\lambda}_v = -\frac{\partial H}{\partial v} = -\frac{\lambda_\theta}{r_{sc}} - 2\frac{\lambda_u v}{r_{sc}} + \frac{\lambda_v u}{r_{sc}}. \quad (1.37)$$

From Pontryagin's maximum principle, an optimal control law may be determined by maximizing  $H_0$ . Introducing the primer vector control law [61, 82]

$$\lambda \equiv \lambda [\cos \alpha_\lambda, \sin \alpha_\lambda]^T, \quad \lambda \equiv \sqrt{\lambda_u^2 + \lambda_v^2}, \quad \alpha_\lambda \equiv \cos^{-1} \left( \frac{\lambda_v}{\sqrt{\lambda_u^2 + \lambda_v^2}} \right), \quad (1.38)$$

where  $\alpha_\lambda$  is the coning angle, an optimal steering law is found with  $\alpha = \alpha_\lambda$  and  $\text{sign}(\alpha_\lambda) \alpha_{\max}$  for  $|\alpha_\lambda| \leq \alpha_{\max}$  and  $|\alpha_\lambda| > \alpha_{\max}$ , respectively. Finally, an optimal switching law is found with a bang-bang control, where  $\tau = 0$  and  $\tau = 1$  for  $\lambda_u \cos \alpha + \lambda_v \sin \alpha \leq 0$  and  $\lambda_u \cos \alpha + \lambda_v \sin \alpha > 0$ . For stability requirements is assumed a maximum value of  $\alpha_{\max} = 35$  deg [69]. For a circular, coplanar transfer orbit the final hyperbolic excess velocity is

$$V_\infty = \sqrt{u(t_f)^2 + \left[ v(t_f) - \sqrt{\mu_\odot/r_J} \right]^2}, \quad (1.39)$$

where  $r_J$  is distance from the sun to Jupiter (5.2 AU). For the special case of rendezvous trajectory, the final hyperbolic excess velocity vanishes. We consider here a free range of  $V_\infty$  values between  $0.5\Delta V_H$  and  $\Delta V_H$ , being  $\Delta V_H$  the velocity variation for a Hohmann heliocentric transfer in a coplanar, circular orbit. For Jupiter, the final hyperbolic excess velocity is

$$\Delta V_H = \sqrt{\frac{\mu_\odot}{r_e}} \left[ \sqrt{\frac{2r_J}{r_J + r_e}} - 1 \right] + \sqrt{\frac{\mu_\odot}{r_J}} \left[ 1 - \sqrt{\frac{2r_e}{r_J + r_e}} \right] \approx 14.44 \text{ km/s.} \quad (1.40)$$

Additionally, the minimum flight time is found imposing final conditions. The final spacecraft distance coincides with the target orbit radius,  $r(t_f) = r_J$ . Considering that the final angular position of the SC is free, i.e.  $\lambda_\theta(t_f) = 0$ , equation (1.35) implies that  $\lambda_\theta = \text{constant} = 0$ . Using the boundary condition  $\lambda_u(t_f) \left[ v(t_f) - \sqrt{\mu_\odot/r_J} \right] = \lambda_v(t_f) u(t_f)$  given by reference [10] and imposing the transversality condition  $H(t_f) = 1$  we found the minimum flight time.

As example, one may choose 100 tethers of 20 km and  $R = 20 \mu m$  for Earth-to-Jupiter orbit transfer, i.e. orbit from 1 AU to 5.2 AU. We consider  $m_{pay} = 100$  kg for several  $\Phi_p$  values and  $m_{pay} = 1000$  kg for  $|\Phi_p| = 30$  kV. Figure 1.6 shows the optimized orbit from Earth to Jupiter for several  $\Phi_p$  values, and assuming flow (straight-line) and  $S = 0$  (pointed-line).

A summary of results for Jupiter-to-Earth transfer is shown in Table 1.2. Notice that same accelerations might be attained with 200 tethers of 10 km. For an Earth-to-Jupiter orbit transfer which combines an hybrid strategy of chemical thrusters with an electric solar sail, the capture will occur if the chemical thruster gives the following variation of velocity required to reach a parabolic orbit around Jupiter [9]

$$\Delta V_{\text{cap}} = \sqrt{\frac{2\mu_J}{R_J + h_p} + V_\infty^2} - \sqrt{\frac{2\mu_J}{R_J + h_p}}, \quad (1.41)$$

where  $R_J$  and  $\mu_J$  are radius and gravitational standard parameter of Jupiter, respectively, and  $h_p$  would be the pericenter height of the capture orbit around Jupiter.

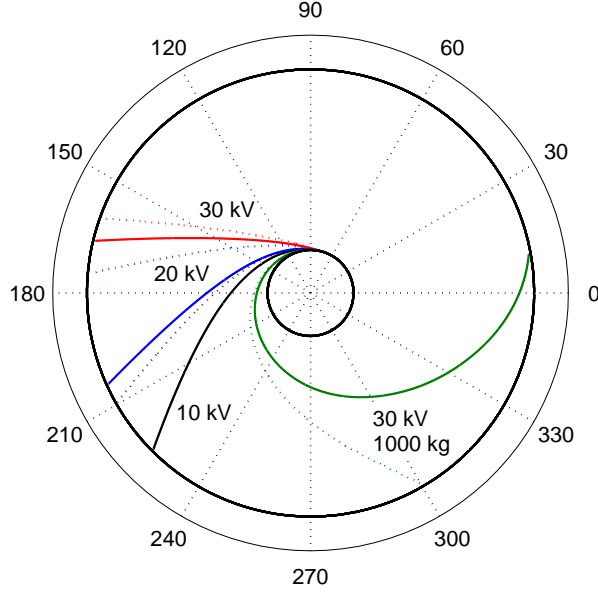


Figure 1.6: Orbit transfer from Earth to Jupiter assuming flow (straight-line) and  $S = 0$  (pointed-line) for several tether bias of  $|\Phi_p| = 10, 20$  and  $30$  kV. We consider here aluminum tethers with  $L = 20$  km and  $R = 20 \mu m$ . For a set of 100 tethers with the dimensions suggested we have  $m_t = 13.6$  kg.

| $ \Phi_p $ (kV)              | $F_c/L$ (nN/m) | $\beta$ | $m_{pay}$ (kg) | $N_t$ | $L$ (km) | $t$ (years) |
|------------------------------|----------------|---------|----------------|-------|----------|-------------|
| flowing case                 |                |         |                |       |          |             |
| 10                           | 85             | 1.20    | 100            | 100   | 20       | 1.32        |
| 20                           | 117            | 1.10    | 100            | 100   | 20       | 1.10        |
| 30                           | 280            | 1.05    | 100            | 100   | 20       | 0.75        |
| 30                           | 280            | 1.05    | 1000           | 100   | 20       | 3.45        |
| non-flowing case ( $S = 0$ ) |                |         |                |       |          |             |
| 10                           | 108            | 1.20    | 100            | 100   | 20       | 1.17        |
| 20                           | 228            | 1.00    | 100            | 100   | 20       | 0.82        |
| 30                           | 363            | 0.85    | 100            | 100   | 20       | 0.68        |
| 30                           | 363            | 0.85    | 1000           | 100   | 20       | 2.06        |

Table 1.2: Results for a Jupiter-to-Earth transfer with  $R = 20 \mu m$ , and considering flow and  $S = 0$ .

## 1.8 Discussion

In the present work, we use a symmetric potential profile, given by the numerical solution of equations (1.13), (1.14) and (1.16), to calculate ion scattering due to a



simple tether. Godard and Laframboise shown large collected currents for  $S$  increasing (Figure 2 from Ref. [37]); i.e. much more ions are collected by the tether for larger flow-to-thermal velocity ratio, decreasing the number of ions scattered by the potential. The validity of symmetric potential is expected if i) the collector-to-Debye length ratio is small, corresponding to OML condition, and ii) the condition  $S^2 \ll e|\Phi_p|/kT_i$  is attained. Since both conditions occurs for the range here considered from 1 AU to 6 AU, the potential might be considered nearly symmetric. For large  $S$  values, ions will enter into the sheath and substantial potential asymmetries may then occur even if  $S^2 \ll e|\Phi_p|/kT_i$  [37]. In the case of interest, small potential asymmetries at the front of the e-sail are assumed, whereas the larger perturbation might occur in the wake for a single tether.

Similar behaviors between our results shown from figure 1.2 and the figure 2 in reference [68] are realized for both electron and ion density in the ion flow stream case. Since the potential reaches lower distance and the quasi-neutrality condition  $N_e = N_i = 1$  is reached earlier, the resulting thrust is reduced for cylindrical tethers in high plasma flow. The ion density near the tether is equal to half of the ambient density ( $N_i = 0.5$ ), i.e. half of the directions are blocked by the tether. All incoming directions are populated at the surface of this sufficiently small radius tether, resulting in a maximized surface ion density of half the ambient density, corresponding to the OML.

The resulting thrust, given by equation (1.25), is used to determine the optimal trajectory from Earth to Jupiter for several values of masses and potential bias. For both flow and non-flow conditions,  $\beta$  exponent, which gives the power-law for the thrust, decreases if  $\Phi_p$  increases. Table 1.2 shows the  $\beta$  exponent decreases more rapidly with  $\Phi_p$  for  $S = 0$ . Since  $r_{\max}$  varies along the orbit trajectory from Jupiter to Earth, the distance between parallel tethers should be accommodated to evade interference effects.

Meteoroid population models should be considered to analyze the sever probability in a set of parallel tethers for an interplanetary mission. The orbit trajectory should be selected for the lower impact risk against the tether. Models like the NASA's Meteoroid Engineering Model (MEM) are applicable to missions from 0.2 to 2.0 AU near the

ecliptic plane [63], whereas the ESA's Interplanetary Meteoroid Environment Model (IMEM) increases the range up 5.0 AU and is available for every latitude [26]. In chapter 3 the sever probability of a single tether will be determined for a de-orbiting mission in Low Earth Orbit.

A tether might be deployed at Jupiter from the electric solar sail for capture and scientific phases. The tether capture will be produced through lowering apojove under repeated Lorentz force, which uses no propellant. A detailed analysis of Jovian capture by an electrodynamic tether is shown in reference [100]. The tether capture for other planets might be extremely difficult. For a Saturn mission, tether capture could be unattainable due to a small magnetic field and a moderate mean density, which is not enough to produce drag force for lowering the apojove. Superconductive tether material, as in Alfven's old method for solar-wind thrusting, appears necessary for use in Saturn. In the next chapter several scientific missions at Jupiter will be discussed; tether radiation, generation of auroral effects and charged grain interactions are analyzed.

## CHAPTER 2

# SCIENTIFIC MISSIONS IN JUPITER WITH ELECTRODYNAMIC TETHERS

### 2.1 Introduction

In the previous chapter we have shown that a set of parallel tethers might be used to reach Jupiter in a direct orbit transfer. Gravity assists are generally used to reach outer planets as Jupiter. NASA's Juno mission, the first solar-powered mission to Jupiter, will use an Earth Gravity Assist to reach Jupiter. The Juno spacecraft will fly-by the Earth on 9 October 2013 at an altitude of 563 km. On 5 July 2016, Juno will follow an orbit insertion to allow capture into a polar, high-eccentricity ( $i \approx 90^\circ$ ,  $e \approx 0.947$ ) orbit with low perijove ( $\sim 1.06R_J$ ) and high apojove ( $\sim 39R_J$ ). The large  $J_2$  zonal harmonic of the Jovian gravitational field produces fast apsidal precession ( $\sim 1^\circ/\text{orbit}$ ) during the 32 planned orbits. Figure 2.1 shows the elliptical orbits for Juno-like mission,  $\psi$  and  $\nu$  being argument of periapsis and true anomaly, respectively. For Jovian moons protection requirements the mission will finish with the orbiter falling to Jupiter [67].

Low-efficiency radioisotope power systems (RPSs) were used in all past outer planet exploration missions [81, 91]. The radioisotope thermoelectric generator (RTG), a RPS well-known type, was used for the Galileo Jupiter Orbiter, delivering approximately 300 W of electric power. The long half-life of the isotope used,  $Pu^{238}$ , allows long operative

mission times. This type of man-made radioisotope is expensive, however, and will be limited as support to some scheduled outer-planet missions [81]. Considerable effort goes into developing technologies to solve the severe power-generation problem. Typical solar arrays on spacecraft like Juno and the already launched Rosetta are inefficient in supplying electrical power, because of the weak light reaching outer solar regions, such as at Jupiter and the main asteroid belt. A nuclear reactor is another proposed device for power generation; the canceled Jupiter Icy Moons Orbiter (JIMO) mission would have used this type of energy in a Jovian mission.

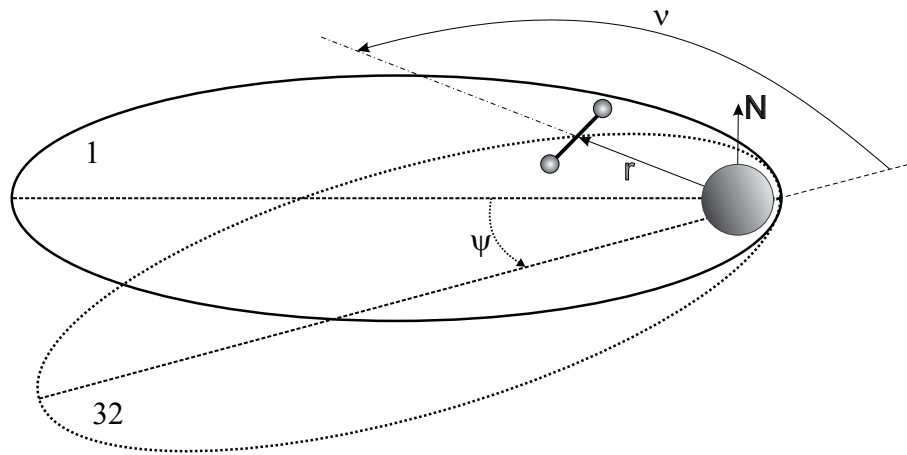


Figure 2.1: Elliptical orbits for Juno mission. The influence of Jupiter's oblateness produces apsidal precession over the polar plane;  $\psi$  is argument of periapsis,  $\nu$  is true anomaly.

A conductive tether orbiting in the Jovian magnetosphere could produce the required power for feeding communication systems and scientific instruments. Power generation has been considered in proposed bare-tether missions to the Jovian system. A Jupiter capture into low-perijove, equatorial orbit [100] would be followed by a moon tour [101], using power generated in the tether. Alternatively, capture would be followed by repeated apojove lowering, using Lorentz drag at each perijove pass; afterwards, slow inward spiraling in Low Jovian Orbit (LJO), below the radiation belts, would allow in-situ measurements of charged grains and auroral sounding of the inner Jovian magnetosphere [18]. Power generation in a Juno-type orbit has been also considered [14]. A two-stage mission to place a spacecraft (SC) below the Jovian radiation belts, using a spinning bare tether with plasma contactors at both ends to provide propulsion

and power, is proposed. Capture by Lorentz drag on the tether, at the periapsis of a barely hyperbolic equatorial orbit, is followed by a sequence of orbits at near-constant periapsis, drag finally bringing the SC down to a circular orbit below the halo ring ( $\sim 1.4R_J$ ). Although increasing both tether heating and bowing, retrograde motion can substantially reduce accumulated dose as compared with prograde motion, at equal tether-to-SC mass ratio. In the second stage, the tether is cut to a segment one order of magnitude smaller, with a single plasma contactor, making the SC to slowly spiral inward over several months while generating large onboard power, which would allow multiple scientific applications, including in situ study of Jovian grains, auroral sounding of upper atmosphere, and space- and time-resolved observations of surface and subsurface.

A LJO mission would determine the structure and dynamics of the Jovian atmosphere, which is actually one of the goals of the ESA Europa Jupiter System Mission too. Data registered over long periods would allow studying atmospheric variability over different time scales. In-situ measurements would provide information about mass, charge and composition of dusty grains. Tethers moving close to the Jovian surface would increase our knowledge of its inner composition and structure. Additionally, the tether would give high resolution for gravity and magnetic field determination, and abundance of water in Jupiter. A Juno-type polar orbit with close perijove allows excellent science in-situ measurements, determining the mass of Jupiter's solid core and the abundance of species in its atmosphere. Additionally, a polar orbit would allow exploring high latitude phenomena such as auroras and would determine higher harmonics of the Jupiter's gravity and magnetic field.

## 2.2 Tether radiation in Juno-type and circular-equatorial Jovian orbits

### 2.2.1 Introduction

Wave radiation by a conductor carrying a steady current in both a polar, highly eccentric, low perijove orbit, as in NASA's Juno mission, and an equatorial Low Jovian Orbit

(LJO) mission below the intense radiation belts is considered. Both missions will need electric power generation for scientific instruments and communication systems. Tethers generate power more efficiently than solar panels or Radioisotope Power Systems (RPS). The radiation impedance is required, if not too small, to determine the current in the overall tether circuit. In a cold plasma model, radiation occurs mainly in the Alfvén and Fast Magnetosonic modes, exhibiting a large refraction index. The radiation impedance of insulated tethers is determined for both modes and either mission. Unlike the Earth ionospheric case, the low-density, highly-magnetized Jovian plasma makes the electron gyrofrequency much larger than the plasma frequency; this substantially modifies the power spectrum for either mode by increasing the Alfvén velocity. Finally, an estimation of the radiation impedance of bare tethers is considered. In LJO, a spacecraft orbiting in a slow downwards spiral under the radiation belts would allow determining magnetic field structure and atmospheric composition for understanding the formation, evolution and structure of Jupiter. Additionally, if the cathodic contactor is switched off, a tether floats electrically allowing e-beam emission that generate auroras. On/off switching produces bias/current pulses and signal emission, which might be used for Jovian plasma diagnostics.

Pioneer work on the plasma waves radiated by a conductive tether in Low Earth Orbit (LEO) was carried out by Drell et al. in 1965 [31]. This work was followed by later authors Barnett and Olbert, 1986 [6]; Dobrowolny and Veltri, 1986 [28]; Hastings and Wang, 1987, 1989 [41] [42]; Estes, 1988 [33]; Donohue et al., 1991 [29]; Sanmartin and Martinez-Sanchez, 1995 [94] considering the cold plasma approximation. Recently, Biancalani and Pegoraro in 2010 [13], considered radiation by a loop current inside a satellite orbiting in LEO, and Sanchez-Torres et al, 2010 [87] carried out a preliminary study of the Alfvén impedance of a tether in a Juno-like orbit at the Jovian magnetosphere. The Alfvén impedance  $Z_A$  was determined for the first orbit and both equatorial and polar region cases. High Alfvén velocity  $V_A$  found in [87] gives high Alfvén impedance too, because of  $Z_A \propto V_A$ . Additionally, there are two contributions to the Alfvén impedance, involving logarithmic terms that depend of both tether length and contactor size.

Figure 2.2 shows the 5 modes of a magnetized cold plasma,  $\theta$  being the angle between magnetic field  $\mathbf{B}$  and wavevector  $\mathbf{k}$ : Alfven or shear Alfven (A), fast magnetosonic or compressional Alfven (FM), slow extraordinary (SE), ordinary (O) and fast extraordinary (FE). For a steady-current carrying tether, the wave frequency in the plasma frame is given by the Doppler relation  $\omega = \mathbf{V}_{rel} \cdot \mathbf{k}$ . Since the relative velocity  $\mathbf{V}_{rel}$  is much lower than the light velocity  $c$ , the refraction index  $n \equiv ck/\omega$ , is very large in all cases,  $n^2 > c^2/V_{rel}^2$ . Both fast magnetosonic and Alfven branches present resonances at large  $n$  values, allowing steady current emission in the cold plasma model.

In the present work we consider the radiation impedance for both Alfven and FM waves, and both Juno and LJO missions. Anticipating that the wave vector  $\mathbf{k}$  will be nearly perpendicular to the ambient magnetic field in all cases considered,  $\mathbf{k} \simeq \mathbf{k}_\perp$ , the Doppler relation reads

$$\omega \simeq \mathbf{V}_{rel} \cdot \mathbf{k}_\perp = (\mathbf{V}_{orb} - \mathbf{V}_{pl}) \cdot \mathbf{k}_\perp, \quad (2.1)$$

greatly simplifying the calculation of impedances. For most of the analysis we will consider the simpler, insulated tether case.

A review of the ambient and orbital Jovian conditions is presented in section 2.2.2. The plasma cold model is described in section 2.2.3. In section 2.2.4, we study the wave field from a tether current-density source. The dispersion relation for both Alfven and Fast Magnetosonic waves is discussed. We also discuss the analysis of the radiation impedance carried out by Biancalani and Pegoraro, 2010 [12], who used a current-source model irrelevant for tethers, leading to impedances small by orders of magnitude when compared to a generic current-source. Using the dispersion relation we give the radiation impedance formulas for Alfven and FM modes in section 2.2.5. In section 2.2.6 we calculate FM impedance for either Juno and LJO mission. The integrand of the Alfven radiation impedance is markedly simple for equator and polar caps cases. In section 2.2.7 we calculate the Alfven radiation impedance for both extreme cases. In section 2.2.8 we determine the general Alfven radiation impedance for both missions. Bare tether radiation impedance is briefly discussed in section 2.2.9. Discussion and a summary of the main results are presented in section 2.2.10. Thermal effects for the Alfven radiation impedance, which will be included in a future work, are briefly

discussed in Appendix A.

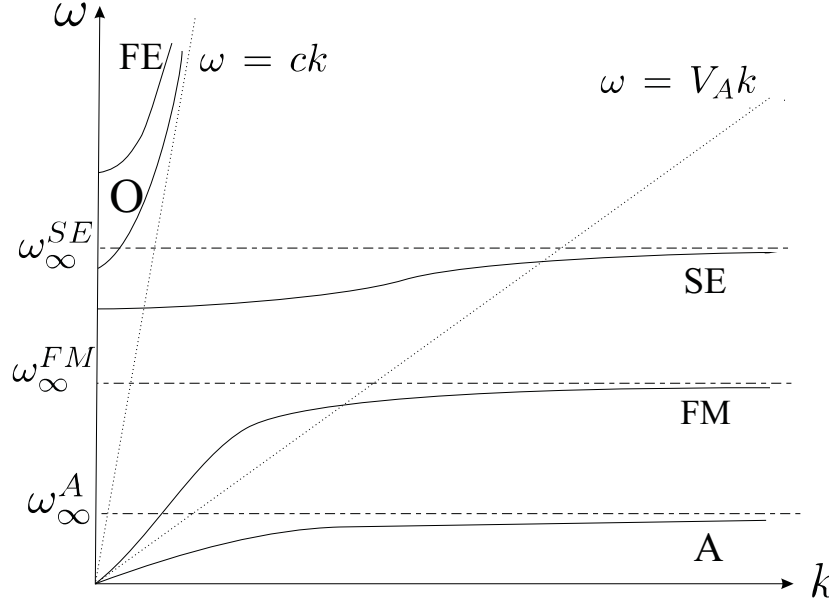


Figure 2.2: Representation of branches (fast extraordinary(FE), ordinary (O), slow extraordinary (SE), fast magnetosonic (FM), and Alfven (A)) for the dispersion relation of a cold, magnetized plasma at given angle between  $\mathbf{k}$  and  $\mathbf{B}$ . Because of the highly magnetized and low-density Jovian plasma,  $\omega_{\infty}^{FM}$  ranges from  $\omega_{pe}$  down to the lower hybrid frequencies,  $\omega_{LH}$ .

### 2.2.2 Ambient and orbital Jovian conditions

The thermal plasma density in the Divine-Garrett model [27] for the particular plasmasphere region here studied ( $1.0R_J < r < 3.8R_J$ ), is

$$N_e = 4.65 \cdot \exp \left[ 7.68 \frac{R_J}{r} - \left( \frac{r}{R_J} - 1 \right)^2 \lambda^2 \right] \text{ cm}^{-3}, \quad (2.2)$$

where  $\lambda$  is latitude and  $R_J$  is Jupiter's equatorial radius. The dipole-model magnetic field, neglecting its tilt, is

$$B = B_0 \left( \frac{R_J}{r} \right)^3 \sqrt{1 + 3 \sin^2 \lambda}, \quad (2.3)$$

with  $\mathbf{B}$  contained in the meridian plane, and  $B_0 \approx 4.23$  gauss the surface magnetic field at the Jovian equator. Using a co-rotational model of the Jovian near-magnetosphere [27], the magnitude of the plasma velocity, taking a  $\sim 10$  h Jovian rotation period,



reads

$$V_{pl} = 12.6 \times \frac{r \cos \lambda}{R_J} \frac{\text{km}}{\text{s}}. \quad (2.4)$$

Considering cyclotron and plasma frequencies for each species  $\Omega_\sigma = eB/m_\sigma$ ,  $\omega_{p\sigma} = \sqrt{e^2 N_e / m_\sigma \varepsilon_0}$  with  $\sigma = e, i$ , and assuming sulphur ions and equations (2.2) and (2.3), we can determine the Alfven velocity,  $V_A \equiv c\Omega_i/\omega_{pi} \propto B/\sqrt{m_i N_e}$ .

For the equatorial circular Jovian orbit in a LJO mission, we have  $\lambda = 0$  and  $r = \text{constant} \equiv r_c$  in (2.2), (2.3) and (2.4). Orbital and Alfven velocities then read

$$\begin{aligned} V_{orb} &= \sqrt{\frac{\mu_J}{r_c}} \approx 42.2 \sqrt{\frac{R_J}{r_c}} \frac{\text{km}}{\text{s}}, \\ V_A &\approx 7.55 \cdot 10^5 \frac{\text{km}}{\text{s}} \left( \frac{R_J}{r_c} \right)^3 \times \exp \left( -3.84 \frac{R_J}{r_c} \right), \end{aligned}$$

where  $\mu_J$  is the gravitational parameter of Jupiter. For  $r_c < 2.24R_J$ , we have  $|\mathbf{V}_{orb}| > |\mathbf{V}_{pl}|$ . The relative velocity  $\mathbf{V}_{rel} = \mathbf{V}_{orb} - \mathbf{V}_{pl}$  then gives  $V_{rel}^{ret} = V_{orb} + V_{pl}$  in retrograde orbit and  $V_{rel}^{pro} = V_{orb} - V_{pl}$  in prograde orbit. Such velocities represented in Figure 2.3 follow the ordering  $V_{pl} \leq V_{rel}^{pro} \leq V_{orb} \leq V_{rel}^{ret}$ . Frequencies in the plasma follow the ordering  $\Omega_e \gg \omega_{pe} \gg \omega_{pi} \gg \Omega_i$ , making  $n \rightarrow \infty$  FM waves range from  $\omega_{pe}$  down to a lower hybrid frequency  $\omega_{LH} \simeq \omega_{pi}$  [3].

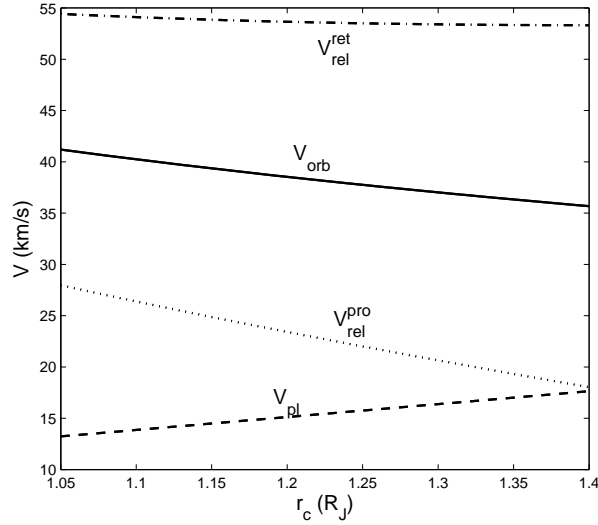


Figure 2.3: Relative, orbital and plasma velocities for LJO. Note that  $V_{orb} > V_{pl}$  for  $r < 2.24R_J$ .

For Juno, fast apsidal precession substantially modifies the ambient plasma/orbit conditions. We use  $\lambda = \nu + \psi$  in (2.2), (2.3) and (2.4). For the representative arc of

orbits here studied,  $-90^\circ < \lambda < 90^\circ$ , the high-eccentricity allows the parabolic orbit approximation,

$$r \simeq \frac{2r_p}{1 + \cos \nu},$$

where  $r_p$  is perijove distance. The orbital velocity for a parabolic orbit can be written in components as  $\mathbf{V}_{orb} = (V_r, V_\nu, 0)$ , with

$$V_r = \sqrt{\frac{\mu_J}{2r_p}} \sin \nu, \quad V_\nu = \sqrt{\frac{\mu_J}{2r_p}} (1 + \cos \nu).$$

The magnitude of the velocity  $V_{orb}$  in the polar plane, then reads

$$V_{orb} = \sqrt{\frac{2\mu_J}{r}} \approx 59.7 \sqrt{\frac{R_J}{r}} \frac{\text{km}}{\text{s}}. \quad (2.5)$$

Figure 2.4 shows  $V_{orb}$  versus  $\lambda = \nu + \psi$ . For both the first and last orbits the orbital velocity is larger than  $V_{pl}$ .

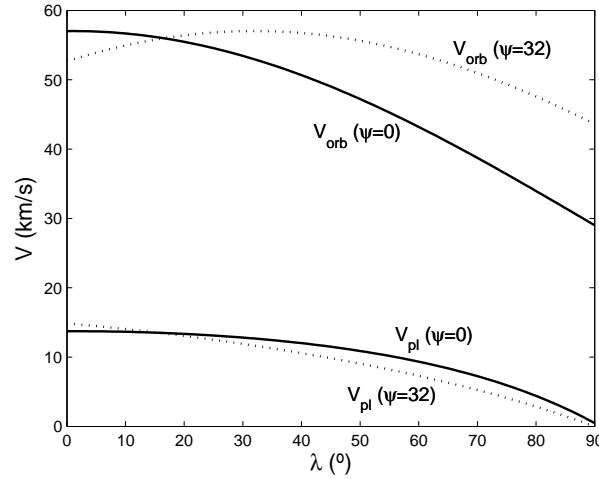


Figure 2.4: Both orbital and plasma velocities at a polar, parabolic,  $r_p = 1.09R_J$  orbit are shown. The orbital velocity is larger than  $V_{pl}$ . Plasma velocity vanishes at  $\lambda = \nu + \psi = \pi/2$  values.

The Alfvén velocity is represented for those first and last Juno-like orbits in Figure 2.5. We have  $V_A \sim c$  near  $\lambda = \pi/2$  in the first orbit, and the lower hybrid frequency then reads

$$\omega_{LH} \simeq \sqrt{\omega_{pi}^2 + \Omega_i^2},$$

whereas  $\omega_{LH} \simeq \omega_{pi}$  holds near  $\lambda \approx 0$  in the first orbit, as well as for the full arc of the last orbit ( $0 < \nu + \psi < \pi/2$ ), and for LJO. Notice that the ordering  $\Omega_e \gg \omega_{pe}$  also holds for Juno-like orbits.

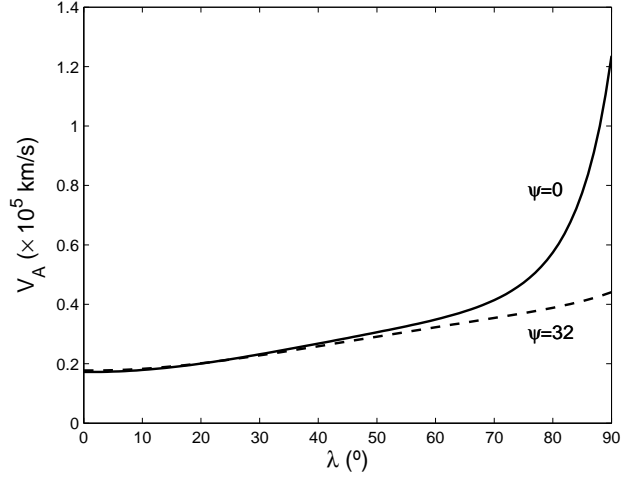


Figure 2.5: The Alfvén velocity is represented for both the first and last Juno-like orbit for a broad  $\lambda$  range. The Alfvén velocity increases sharply near  $\lambda \sim \pi/2$  values at the first orbit.

At a Juno orbit, the angle  $\beta$  between magnetic field  $\mathbf{B}$  and orbital velocity  $\mathbf{V}_{orb}$ , which will be later needed for impedance calculations, reads

$$\beta = \cos^{-1} \left[ \frac{2 \sin \nu \sin \lambda - (1 + \cos \nu) \cos \lambda}{\sqrt{2(1 + \cos \nu)} \sqrt{1 + 3 \sin^2 \lambda}} \right], \quad (2.6)$$

which is represented for  $\psi = 0$  and  $\psi = 32$  in Figure 2.6. For the first orbit the angle  $\beta$  is  $\pi$  and  $\pi/4$  for  $\lambda = 0$  and  $\lambda = \pi/2$ , respectively.

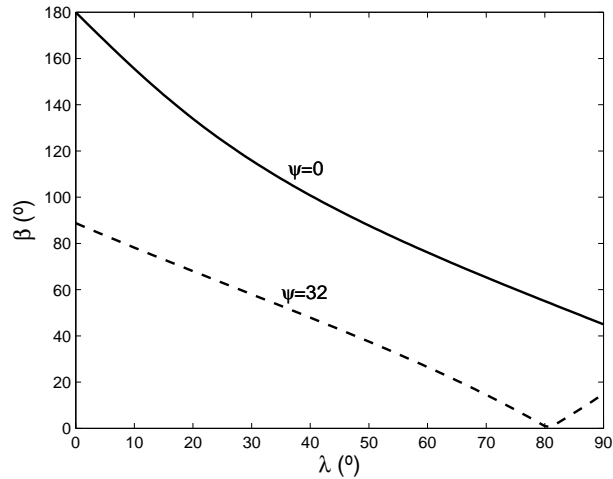


Figure 2.6: The angle  $\beta$  between the magnetic field and the orbital velocity is represented here for both Juno first and last orbits.

Finally, both in Juno and LJO we have  $V_A^2 \gg V_{rel}^2 m_i/m_e$ , which is equivalent to  $(c/\omega_{pe})^2 \gg (V_{rel}/\Omega_i)^2$ .

### 2.2.3 Cold-plasma model

For the description of the plasma oscillation of the plasma which is continue interacting with an external magnetic field  $\mathbf{B}$ , and neglecting the effect of the thermal motion of the particles on the wave propagation, we use the magnetohydrodynamic equations for two components [3]. Lorentz force reads

$$m_\alpha \frac{d_\alpha \mathbf{u}_\alpha}{dt} = e_\alpha \left\{ \mathbf{E} + \frac{1}{c} [\mathbf{u}_\alpha \wedge (\mathbf{B})] \right\}, \quad \frac{d_\alpha}{dt} = \frac{\partial}{\partial t} + \mathbf{u}_\alpha \cdot \nabla, \quad (2.7)$$

and the continuity equation is

$$\frac{\partial n_\alpha}{\partial t} + \text{div } n_\alpha \mathbf{u}_\alpha = 0, \quad (2.8)$$

where  $\alpha = i, e$  are ionic and electron components. The electromagnetic wave described by the electric field  $\mathbf{E}$  and the magnetic field  $\mathbf{B}$  is determined from the Maxwell equations. With source current density  $\mathbf{j}_s$  and density  $\rho$ , respectively,

$$\mathbf{j}_s = \sum_{\alpha} e_\alpha n_\alpha \mathbf{u}_\alpha, \quad (2.9)$$

$$\rho = \sum_{\alpha} e_\alpha n_\alpha, \quad (2.10)$$

and linearizing for small amplitude oscillations and assuming  $n_\alpha = n_0$  y  $\mathbf{u}_\alpha = \mathbf{E} = 0$  in the equilibrium state, we obtain

$$\frac{\partial \mathbf{u}_\alpha}{\partial t} = \frac{e_\alpha}{m_\alpha} \left\{ \mathbf{E} + \frac{1}{c} [\mathbf{u}_\alpha \wedge \mathbf{B}] \right\} \quad (2.11)$$

$$\frac{\partial n'_\alpha}{\partial t} + n_0 \text{div } \mathbf{u}_\alpha = 0, \quad (2.12)$$

where  $n'_\alpha = n_\alpha - n_0$  is the variable particle density.

Since variable elements are proportional to  $e^{i(\mathbf{k} \cdot \mathbf{r} - i\omega t)}$  for monochromatic waves, equations (2.11) and (2.12) give

$$-\frac{e_\alpha}{m_\alpha} \mathbf{E} = i\omega \mathbf{u}_\alpha + \frac{e_\alpha}{m_\alpha c} [\mathbf{u}_\alpha \wedge \mathbf{B}], \quad (2.13)$$

$$n'_\alpha = n_0 \frac{(\mathbf{k} \cdot \mathbf{u}_\alpha)}{\omega}. \quad (2.14)$$

Taking the  $z$ -axis along  $\mathbf{B}$  the velocity components for each species are

$$u_{\alpha x} = \frac{e_{\alpha} (i\omega E_x - \Omega_{\alpha} E_y)}{m_{\alpha} (\omega^2 - \Omega_{\alpha}^2)}, \quad u_{\alpha y} = \frac{e_{\alpha} (i\omega E_y + \Omega_{\alpha} E_x)}{m_{\alpha} (\omega^2 - \Omega_{\alpha}^2)}, \quad u_{\alpha z} = \frac{ie_{\alpha} E_z}{m_{\alpha} \omega} \quad (2.15)$$

The source current density  $\mathbf{j}_s = en_0 (\mathbf{u}_i - \mathbf{u}_e)$  expressed in function of the conductivity tensor  $\mathbf{j}_s = \sigma_{ij} \mathbf{E}$ , gives the dielectric tensor

$$\epsilon_{ij} = \begin{pmatrix} \epsilon_1 & i\epsilon_2 & 0 \\ -i\epsilon_2 & \epsilon_1 & 0 \\ 0 & 0 & \epsilon_3 \end{pmatrix}, \quad (2.16)$$

where the elements of the dielectric tensor are

$$\epsilon_1 = 1 - \sum_{\alpha} \frac{\omega_{p\alpha}^2}{\omega^2 - \Omega_{\alpha}^2}, \quad \epsilon_2 = - \sum_{\alpha} \frac{\omega_{p\alpha}^2 \Omega_{\alpha}}{\omega (\omega^2 - \Omega_{\alpha}^2)}, \quad \epsilon_3 = 1 - \sum_{\alpha} \frac{\omega_{p\alpha}^2}{\omega^2}. \quad (2.17)$$

For a cold plasma model of two components, the elements of the dielectric tensor are

$$\epsilon_1 = \frac{(\omega^2 - \omega_{UH}^2) (\omega^2 - \omega_{LH}^2)}{(\omega^2 - \Omega_e^2) (\omega^2 - \Omega_i^2)}, \quad (2.18)$$

$$\epsilon_2 \simeq \frac{\omega_{pe}^2}{\omega^2 - \Omega_e^2} \frac{\Omega_e \omega}{\omega^2 - \Omega_i^2}, \quad (2.19)$$

$$\epsilon_3 \simeq 1 - \frac{\omega_{pe}^2}{\omega^2}, \quad (2.20)$$

where  $\Omega_e > 0$  and both high and low hybrid frequencies are, respectively,

$$\omega_{UH}^2 \simeq \omega_{pe}^2 + \Omega_e^2, \quad (2.21)$$

$$\omega_{LH}^2 \simeq \Omega_e^2 \frac{\Omega_i^2 + \omega_{pi}^2}{\Omega_e^2 + \omega_{pe}^2}. \quad (2.22)$$

#### 2.2.4 The wave field from a tether current-density source

The equation for the Fourier transform of the electric field would be [3]

$$-\frac{\mathbf{k} \wedge (\mathbf{k} \wedge \mathbf{E})}{k^2} - \frac{\epsilon_{ij} \cdot \mathbf{E}}{n^2} = \frac{4\pi i \mathbf{j}_s}{\omega n^2}, \quad (2.23)$$

where  $\epsilon_{ij}$  is the dielectric tensor in equation 2.16. The Fourier transform of the electric field  $\mathbf{E}$  in (2.23) is decomposed into transverse and longitudinal parts,  $\mathbf{E}_t$  and  $\mathbf{E}_l \equiv -i\mathbf{k}\Phi$  following the formulation in [94], yielding

$$\mathbf{E}_t - \frac{\epsilon_{ij}}{n^2} \cdot (\mathbf{E}_t + \mathbf{E}_l) = \frac{4\pi i \mathbf{j}_s}{\omega n^2}. \quad (2.24)$$

Considering the  $\mathbf{E}_t$  components along  $z$  and perpendicular  $\perp$  to  $\mathbf{B}$ , we have

$$E_{tz} = \frac{\varepsilon_3 E_{lz} + 4\pi i j_{sz}/\omega}{n^2 - \varepsilon_3}, \quad (2.25)$$

$$n^2 \left[ \left(1 - \frac{\varepsilon_1}{n^2}\right)^2 - \frac{\varepsilon_2^2}{n^4} \right] \times \mathbf{E}_{t\perp} = \left( \mathbf{I} - \frac{\boldsymbol{\varepsilon}_\perp^*}{n^2} \right) \cdot \left[ \boldsymbol{\varepsilon}_\perp \cdot \mathbf{E}_{l\perp} + \frac{4\pi i}{\omega} \mathbf{j}_{s\perp} \right], \quad (2.26)$$

where

$$\boldsymbol{\varepsilon}_\perp \equiv \begin{pmatrix} \varepsilon_1 & i\varepsilon_2 \\ -i\varepsilon_2 & \varepsilon_1 \end{pmatrix}, \quad \boldsymbol{\varepsilon}_\perp^* \equiv \begin{pmatrix} \varepsilon_1 & -i\varepsilon_2 \\ i\varepsilon_2 & \varepsilon_1 \end{pmatrix}, \quad (2.27)$$

and  $\mathbf{I}$  is the two-dimensional unit tensor. Using  $\mathbf{k} \cdot \mathbf{E}_t = 0$ , the longitudinal field reads

$$\mathbf{E}_l = -\frac{4\pi i}{\omega} \frac{\mathbf{k}}{k^2 \mathcal{D}} \left[ \left\{ \left(1 - \frac{\varepsilon_1}{n^2}\right)^2 - \frac{\varepsilon_2^2}{n^4} \right\} k_z j_{sz} + \left(1 - \frac{\varepsilon_3}{n^2}\right) \mathbf{k}_\perp \cdot \left( \mathbf{I} - \frac{\boldsymbol{\varepsilon}_\perp^*}{n^2} \right) \cdot \mathbf{j}_{s\perp} \right], \quad (2.28)$$

with the Aström dispersion relation for the field reading

$$\mathcal{D}(k, \theta, \omega) \equiv \left(1 - \frac{\varepsilon_1}{n^2}\right) \mathcal{D}_\infty(k, \theta, \omega) + \left(\sin^2 \theta - \frac{\varepsilon_3}{n^2}\right) \frac{\varepsilon_2^2}{n^2} = 0, \quad (2.29)$$

$$\mathcal{D}_\infty \equiv \varepsilon_1 \sin^2 \theta + \varepsilon_3 \cos^2 \theta - \frac{\varepsilon_3 \varepsilon_1}{n^2}, \quad (2.30)$$

where  $\theta$  is the angle between  $\mathbf{k}$  and  $\mathbf{B}$ .

For any  $\mathbf{k}$ , the equation  $\mathcal{D} = 0$  determines five values of frequency  $\omega$ , though only the three lower frequency branches exhibit resonances, corresponding to the limit  $n \equiv ck/\omega \rightarrow \infty$ , with  $k \rightarrow \infty$  and  $\omega$  approaching finite values (Figure 2.2). The dispersion relation then reads  $\mathcal{D}_\infty = 0$ , with just the first two terms retained in  $\mathcal{D}_\infty$ . As readily seen, for  $n^2 \rightarrow \infty$  the square bracket in (2.28) reads  $\mathbf{k} \cdot \mathbf{j}_s$ , yielding  $\mathbf{E}_l \propto \mathbf{k} \cdot \mathbf{j}_s = \mathcal{O}(1)$ , while (2.25) and (2.26), give  $\mathbf{E}_t = \mathcal{O}(1/n^2)$ . This is the generic result. If  $\mathbf{k} \cdot \mathbf{j}_s$  vanishes identically, however,  $\mathbf{E}_l$  would also vanish as  $n \rightarrow \infty$ . Then, both  $\mathbf{E}_t$  and  $\mathbf{E}_l$  are  $\mathcal{O}(1/n^2)$ .

This applies in particular to analysis by Biancalani and Pegoraro [12], where the tether current  $\mathbf{j}_s$  considered did satisfy the restrictive condition  $i\mathbf{k} \cdot \mathbf{j}_s \equiv 0$  or  $\nabla \cdot \mathbf{j}_s \equiv 0$ . With the  $z$ -axis parallel to the ambient field  $\mathbf{B}$ , current was assumed to flow in an infinitely long and infinitely thin tether lying along the entire  $y$ -axis. This implied conditions  $j_{sx} \equiv j_{sz} \equiv 0$ , and  $k_y \equiv 0$ , and therefore  $i\mathbf{k} \cdot \mathbf{j}_s \equiv 0$ . Clearly the analysis by Biancalani and Pegoraro [12], which gives impedances too small by two orders of magnitude, cannot be posited as applying to a generic ‘realistic’ source current.

The matrix elements of the dielectric tensor for FM and both Juno and LJO read

$$\varepsilon_1 \approx 1 - \frac{\omega_{LH}^2}{\omega^2}, \quad \varepsilon_2 \approx -\frac{\omega_{pe}^2}{\omega\Omega_e}, \quad \varepsilon_3 = 1 - \frac{\omega_{pe}^2}{\omega^2}, \quad (2.31)$$

with all three ratios  $|\varepsilon_j/n^2|$ ,  $j = 1, \dots, 3$  small as in LEO. The dispersion relation then becomes

$$\mathcal{D}_{FM} \equiv \mathcal{D}_\infty(\infty, \theta, \omega) \simeq \varepsilon_1 \sin^2 \theta + \varepsilon_3 \cos^2 \theta = 0. \quad (2.32)$$

It can be shown that use of  $V_A^2 \gg V_{rel}^2 m_i/m_e$  yields  $\cos \theta \ll 1$  as advanced at the end of section 2.2.1, which is different from the LEO case. Notice that  $\cos^2 \theta$  must be retained in the dispersion relation, however.

For Alfven waves ( $\omega < \Omega_i$ ), the ratios  $\varepsilon_1/n^2$ ,  $\varepsilon_2/n^2$  are small, and  $|\varepsilon_3/n^2| \leq \mathcal{O}(1)$  as opposed to the LEO case. The dispersion relation is then

$$\mathcal{D}_A \simeq \mathcal{D}_\infty = 0. \quad (2.33)$$

Notice that  $\mathcal{D}_\infty$  retains here the three terms in (2.30). Wavevector  $\mathbf{k}$  is again nearly perpendicular to  $\mathbf{B}$ , i.e.  $\cos \theta \equiv k_z/k \ll 1$ .

In Juno, the tether, which is assumed rotating in the polar plane to keep it taut in the presence of the weak Jovian gravity gradient, will be at anytime at some angle  $\varphi(t)$  with the magnetic field. The tether can be made to spin using chemical thrusters at its ends with the angular momentum staying constant once the final velocity is attained. Typical spin period would be 10-12 minutes [18]. Figure 2.7 shows the coordinate reference system used to compute the tether impedance both in Juno-like orbit and LJO,  $\beta$  being the angle between  $\mathbf{V}_{orb}$  and  $\mathbf{B}$ . In LJO,  $\beta$  is  $\pi/2$ , whereas it changes with  $\lambda$  for Juno. Since the  $z$  component of the wave vector is small, (2.1) reads

$$\omega \approx \mathbf{k}_\perp \cdot (\mathbf{V}_{orb} - \mathbf{V}_{pl}) \simeq k_y V_{orb,y} - k_x V_{pl} \equiv \omega(\mathbf{k}_\perp), \quad (2.34)$$

where we take the  $y$ -axis in the orbital polar plane, as for both tether and magnetic field, with the  $x$ -axis then along the co-rotating plasma velocity  $V_{pl}$  (see Figure 2.7).

In LJO, the tether is moving in circular equatorial orbit with  $\mathbf{V}_{orb}$  and  $\mathbf{V}_{pl}$  parallel, the  $x$ -axis taken along  $\mathbf{V}_{orb}$ , the  $z$ -axis along  $\mathbf{B}$ , and the  $y$ -axis in the orbital plane, with the angle  $\varphi$  measured from  $\mathbf{V}_{orb}$  (Figure 2.7). The Doppler relation is then simply

$$\omega \equiv V_{rel}^{ret,pro} k_x = (V_{orb} \pm V_{pl}) k_x \quad (2.35)$$

for retrograde (+) and prograde (−) orbits.

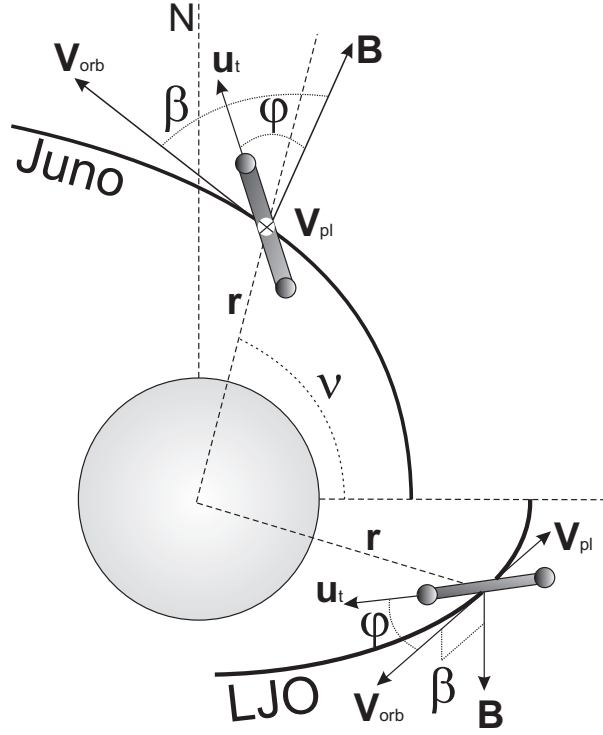


Figure 2.7: Coordinate reference system used to compute the tether impedance both in the first Juno-like orbit and LJO. Notice that in LJO the orbital velocity is in a prograde (retrograde) orbit;  $\mathbf{V}_{orb}$  is represented here in the retrograde case.

Using (2.28) and  $|\mathbf{E}_t| \ll |\mathbf{k}\Phi|$ , then determines the electric potential, which will be required for the impedance calculation in the next section, for either mode

$$\Phi(\mathbf{k}) \simeq \frac{4\pi}{\omega} \mathbf{k}_\perp \cdot \mathbf{j}_s G, \quad G \equiv \begin{cases} (1 - \varepsilon_3/n^2)/k_\perp^2 \mathcal{D}_A & \text{for A} \\ 1/k_\perp^2 \mathcal{D}_{FM} & \text{for FM} \end{cases}, \quad (2.36)$$

where  $\mathcal{D}_{FM}$  and  $\mathcal{D}_A$  are given by (2.32) and (2.33) respectively, and the Doppler relation is given by (2.34) and (2.35) for Juno and LJO, respectively.

### 2.2.5 Radiation impedance formulas

The power required to establish the radiated electromagnetic fields associated with charge and current density from plasma is determined by Poynting theorem

$$P = \dot{W}_{rad} - \dot{U} \quad (2.37)$$



where  $\dot{W}_{rad}$  and  $U$  is radiated power and radiative field energy, respectively.

$$\dot{W}_{rad} = - \int \mathbf{j}_s \cdot \mathbf{E} d\mathbf{r} \quad (2.38)$$

$$U = \frac{1}{8\pi} \int (E^2 + B^2) d\mathbf{r} \quad (2.39)$$

Since the fields are time independent, the power dissipated for a collisionless plasma reads

$$P = \dot{W}_{rad} = - \int \mathbf{j}_s \cdot \mathbf{E} d\mathbf{r}. \quad (2.40)$$

The power radiated, using the vanishing of the source current-density  $\mathbf{j}_s$  outside certain volume and  $|\mathbf{E}_t| \ll |\mathbf{E}_l|$ , reads

$$\begin{aligned} \dot{W}_{rad} &= - \int \mathbf{j}_s \cdot \mathbf{E} d\mathbf{r} = - \int \Phi(\mathbf{r}) \nabla \cdot \mathbf{j}_s d\mathbf{r} \\ &= - \int d\mathbf{r} \int \frac{d\mathbf{k}_1 d\omega_1}{4\pi^2} e^{i\mathbf{k}_1 \cdot \mathbf{r} - i\omega_1 t} \Phi(\mathbf{k}_1, \omega_1) \times \int \frac{d\mathbf{k} d\omega}{4\pi^2} e^{i\mathbf{k} \cdot \mathbf{r} - i\omega t} i\mathbf{k} \cdot \mathbf{j}_s(\mathbf{k}, \omega), \end{aligned}$$

which explicitly depends on the  $\mathbf{j}_s$  divergence and, again, indirectly through (2.36). We introduce a normalized (dimensionless) Fourier transform of the current-density divergence

$$g(\mathbf{k}) \equiv -i \int d\mathbf{r} \nabla \cdot \mathbf{j}_s(\mathbf{r}) e^{-i\mathbf{k} \cdot \mathbf{r}} / 2\pi I_s, \quad (2.41)$$

where  $I_s$  is the source current.

Since the time to describe a characteristic arc in both parabolic Juno-like and circular LJO orbits will be reasonably large compared with a the spin period, the angle-averaged impedance reads [94]

$$\dot{W}/I_s^2 = Z \equiv \int_0^{2\pi} \frac{d\varphi}{2\pi} \int \frac{2i |g(\mathbf{k})|^2 d\mathbf{k}}{\omega} G. \quad (2.42)$$

The current divergence  $\nabla \cdot \mathbf{j}_s(\mathbf{r})$  for an insulated tether is assumed to occur on spherical surfaces at end-contactors of dimension  $R$  small compared with tether length  $L$ ,

$$\nabla \cdot \mathbf{j}_s(\mathbf{r}) = \frac{I_s}{4\pi R^2} \left[ \delta \left( \left| \frac{L}{2} \mathbf{u}_t + \mathbf{r} \right| - R \right) - \delta \left( \left| -\frac{L}{2} \mathbf{u}_t + \mathbf{r} \right| - R \right) \right],$$

(2.41) then yielding for the full divergence above

$$g(\mathbf{k}_\perp) \simeq 2 \times \frac{1}{2\pi} \sin \left( \frac{L}{2} \mathbf{k}_\perp \cdot \mathbf{u}_t \right) \frac{\sin(k_\perp R)}{k_\perp R}, \quad (2.43)$$

where  $\mathbf{k}_\perp \cdot \mathbf{u}_t$  is approximately  $k_y \sin \varphi + k_x \cos \varphi$  and  $k_y \sin \varphi$  for the LJO and Juno cases respectively, and  $\mathbf{u}_t$  is the unit vector along the tether for each rotation angle  $\varphi$  for either case (see Figure 2.7).

It was suggested by Estes [33], Donohue et al. [29] and Sanmartin et al [94] that the characteristic lengths of the cloud emitted by an active contactor or the sheath radius on a passive contactor might be larger than the dimensions of the end-contactor itself; nonlinear effects would adjust contactor areas to an effective value [94]

$$4\pi R^2 = \frac{I_s}{j_{th}}, \quad (2.44)$$

where  $j_{th} \equiv eN_e(k_B T_e/2\pi m_e)^{1/2}$  is the unperturbed random current density, with  $T_e \simeq 46$  eV and the density profile  $N_e$  in the inner plasmasphere given by (2.2).

### Fast Magnetosonic Mode

Using  $\sin^2 \theta \simeq 1$  and  $\cos^2 \theta \simeq k_z^2/k_\perp^2$  in  $D_{FM}$  at (2.32), equation (2.36) becomes

$$G = \frac{1}{\varepsilon_3} \left\{ k_z^2 + \frac{\varepsilon_1}{\varepsilon_3} k_\perp^2 \right\}^{-1}.$$

Using (2.31) for  $\varepsilon_3$ , (2.42) reads

$$Z_{FM} = \int_0^{2\pi} \frac{d\varphi}{2\pi} \int \frac{2i |g(\mathbf{k})|^2 d\mathbf{k}}{\omega} \frac{-\omega^2}{\omega_{pe}^2 - \omega^2} \left\{ k_z^2 - \frac{\varepsilon_1 \omega^2 k_\perp^2}{\omega_{pe}^2 - \omega^2} \right\}^{-1},$$

where  $\omega$  is the frequency given by (2.34) and (2.35) for Juno and LJO, respectively. We use  $\mathbf{k} \simeq \mathbf{k}_\perp$  ( $k_x, k_y$ ) except at  $\mathcal{D}_{FM}$ , allowing to integrate over  $k_z$  poles at  $\mathcal{D}_{FM} = 0$ , with  $\omega \rightarrow \omega + i\delta$  ( $\delta \rightarrow 0^+$ )

$$Z_{FM} = 2\pi \int_0^{2\pi} \frac{d\varphi}{2\pi} \int \frac{d\mathbf{k}_\perp |g(\mathbf{k}_\perp)|^2}{\mathbf{k}_\perp \sqrt{\omega_{pe}^2 - \omega^2}} \frac{\omega}{\sqrt{\omega^2 - \omega_{LH}^2}}. \quad (2.45)$$

### Alfven Mode

For the Alfven branch, we similarly have

$$G = \frac{1 + (\omega_{pe}/ck)^2}{\varepsilon_3 \left\{ k_z^2 + k_\perp^2 [1 + (\omega_{pe}/ck)^2] \varepsilon_1/\varepsilon_3 \right\}}, \quad (2.46)$$

with  $k^2 \simeq k_\perp^2$ , as for the FM mode. Then equation (2.42) finally reads

$$Z_A = \frac{2\pi V_A}{c^2 \sqrt{1 + (V_A/c)^2}} \int_0^{2\pi} \frac{d\varphi}{2\pi} \int \frac{|g(\mathbf{k}_\perp)|^2 d\mathbf{k}_\perp}{k_\perp^2} \frac{\sqrt{1 - \omega^2/\Omega_i^2} \sqrt{1 + c^2 k_\perp^2/\omega_{pe}^2}}{\sqrt{1 - V_A^2 \omega^2/(V_A^2 + c^2) \Omega_i^2}}, \quad (2.47)$$

where the frequency  $\omega$  is again taken from either (2.34) or (2.35).

### 2.2.6 The FM radiation impedance

Using equations (2.43) and (2.45), and (2.34), (2.35) for Juno and LJO, respectively, the FM impedance in polar coordinates  $(k_\perp, \alpha)$  becomes

$$Z_{FM} = \frac{2}{\pi^2 R^2 \omega_{pe}} \int_0^{2\pi} \frac{d\alpha}{k_{LH}} \int_{k_{LH}}^{k_{pe}} \frac{dk_\perp}{k_\perp} \frac{1}{\sqrt{1 - k_\perp^2/k_{pe}^2} \sqrt{k_\perp^2/k_{LH}^2 - 1}} \times \sin^2(k_\perp R) \times \begin{cases} \mathcal{Z}_\varphi^J & \text{for Juno} \\ \mathcal{Z}_\varphi^{LJO} & \text{for LJO} \end{cases}, \quad (2.48)$$

where

$$\mathcal{Z}_\varphi^J \equiv \int_0^\pi d\varphi \sin^2 \left( k_\perp \frac{L}{2} \sin \varphi \sin \alpha \right), \quad (2.49)$$

$$\mathcal{Z}_\varphi^{LJO} \equiv \int_0^\pi d\varphi \sin^2 \left[ k_\perp \frac{L}{2} (\sin \alpha \sin \varphi + \cos \alpha \cos \varphi) \right], \quad (2.50)$$

and  $k_{pe}$  and  $k_{LH}$  are defined by  $|V_{orb,y} \sin \alpha - V_{pl} \cos \alpha| \times k_{pe} \ (k_{LH}) = \omega_{pe} \ (\omega_{LH})$  for Juno and by  $|V_{rel}^{ret,pro} \cos \alpha| \times k_{pe} \ (k_{LH}) = \omega_{pe} \ (\omega_{LH})$  for LJO.

Using  $k_{LH}L, k_{pe}L \gg 1$ , the  $\varphi$ -integral in both (2.49) and (2.50) yields  $\pi/2$ , and using similarly  $k_{LH}R, k_{pe}R \gg 1$ , we set  $\sin^2(k_\perp R) \approx 1/2$  in the  $k_\perp$ -integral, which then yields  $\pi/4$ . We can write  $|V_{orb,y} \sin \alpha - V_{pl} \cos \alpha|$  as  $\sqrt{V_{orb,y}^2 + V_{pl}^2} \cdot |\cos(\zeta - \alpha)|$  with  $\zeta = \tan^{-1}(V_{pl}/V_{orb,y})$ . Finally, evaluating the  $\alpha$ -integral we obtain  $4\tilde{V}_{rel}/\omega_{LH}$  where  $\tilde{V}_{rel}$  is  $\sqrt{V_{orb,y}^2 + V_{pl}^2}$  for Juno and  $V_{rel}^{ret,pro} \equiv V_{orb} \pm V_{pl}$  for LJO. The FM impedance then takes a very simple form,

$$Z_{FM} = \frac{\tilde{V}_{rel}}{R^2 \omega_{pe} \omega_{LH}}. \quad (2.51)$$

Notice that  $V_{orb,y} = V_{orb} \sin \beta$ , with  $\beta$  the angle given in (2.6), in Juno and  $\omega_{LH} \simeq \omega_{pi}$  in LJO.

Using (2.44), the FM voltage drop becomes independent of the contactor model  $R$ -value, at difference with impedance itself,

$$\Delta V_{FM} = Z_{FM} I_s \sim \frac{4\pi \tilde{V}_{rel} j_{th}}{\omega_{pe} \omega_{pi} \sqrt{1 + \Omega_i^2/\omega_{pi}^2}} = \sqrt{\frac{m_i \tilde{V}_{rel}^2 k_B T_e}{2\pi e^2 [1 + (V_A/c)^2]}}, \quad (2.52)$$

with the power radiated in the FM mode  $Z_{FM}I_s^2$  increasing just linearly with  $I_s$  [94]. Using local values of ambient plasma properties and the orbits considered, the voltage drop  $\Delta V_{FM}$  is shown in Figures 2.8 and 2.9 for Juno and LJO, respectively. Figure 2.8 shows the Juno voltage drop maximum reaching  $\sim 90$  V for both the first and last orbit. The voltage drop in LJO is given by (2.52) with  $V_A^2 \ll c^2$  and  $\tilde{V}_{rel} = V_{rel}^{ret,pro}$ . Since  $V_{rel}^{ret}$  is near constant during a retrograde LJO mission, the voltage drop  $\Delta V_{FM} \propto V_{rel}^{ret}$  is practically invariable, whereas  $\Delta V_{FM}$  increases noticeably for a prograde evolution mission from  $1.4R_J$  down to  $1.05R_J$  (see Figure 2.9). FM impedances for both Jovian missions and LEO, which are given by (2.51) and equation (23) from [94], respectively, are similar except for the relative velocities involved.

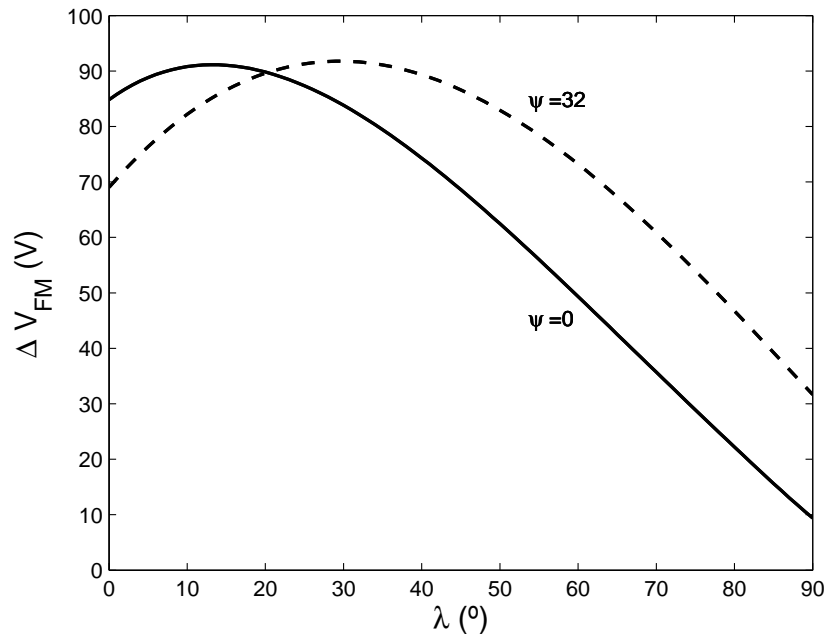


Figure 2.8: Voltage drop  $\Delta V_{FM}$  in Juno for the  $\psi = 0$  and  $\psi = 32$  orbits.

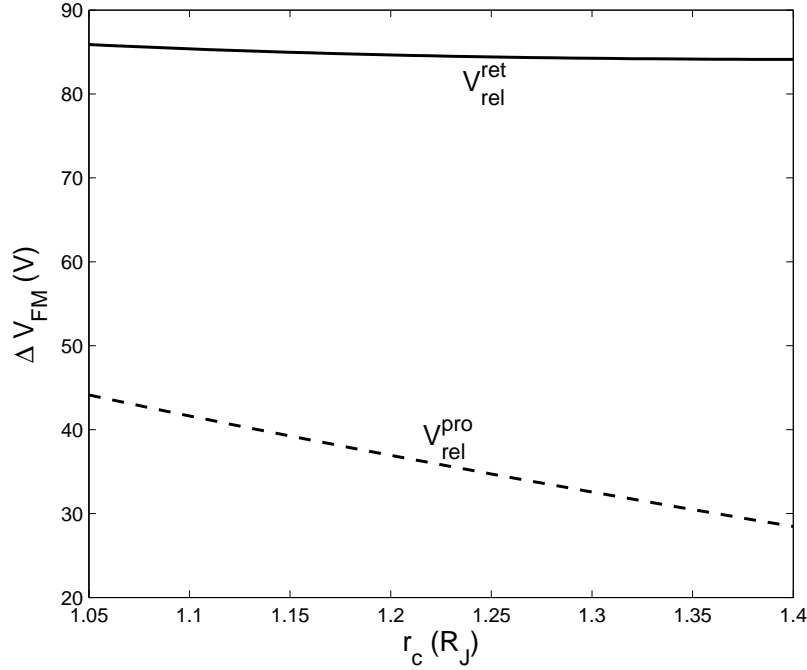


Figure 2.9: Voltage drop  $\Delta V_{FM}$  for both prograde ( $V_{rel}^{pro}$ ) and retrograde ( $V_{rel}^{ret}$ ) Low Jovian Orbit.

### 2.2.7 The Alfven radiation impedance

For Juno, considering (2.43) and (2.47) again, the Alfven radiation impedance in polar coordinates reads

$$\begin{aligned}
 Z_A = & \frac{2V_A}{\pi^2 c^2 \sqrt{1 + (V_A/c)^2}} \int_0^{2\pi} d\alpha \int_0^{k_M^*} \frac{dk_\perp}{k_\perp} \frac{\sqrt{1 - k_\perp^2/k_M^{*2}}}{\sqrt{1 - k_\perp^2/\tilde{k}_M^2}} \\
 & \times \sqrt{1 + \frac{k_\perp^2}{k_m^2} \frac{\sin^2(k_\perp R)}{(k_\perp R)^2}} \times \mathcal{Z}_\varphi^J, \quad (2.53)
 \end{aligned}$$

where  $k_M^* \equiv \Omega_i / |V_{orb,y} \sin \alpha - V_{pl} \cos \alpha|$ ,  $\tilde{k}_M \equiv k_M^* \sqrt{1 + \omega_{pi}^2 / \Omega_i^2}$  and  $\mathcal{Z}_\varphi^J$  is again given by (2.49). Since the integrand of Eq. (2.53) is difficult to be carried out analytically, firstly, we focus the analysis at the equator and polar caps for the first Juno orbit ( $\Psi = 0$ ).

#### 2.2.7.1 The Alfven radiation impedance at the equator

For convenience we change here from polar to cartesian coordinates with  $k_x = k_\perp \cos \alpha$  and  $k_y = k_\perp \sin \alpha$ . In the equatorial case the  $k_x$  wave vector is limited to values  $k_x \leq k_M$ ,

and we have  $V_A^2 \ll c^2$ . The impedance in Eq. (2.53) can now be written as

$$Z_A = \frac{8V_A}{\pi c^2} \times \int_0^{\pi/2} \frac{d\varphi}{\pi/2} \mathcal{Z}_A \quad (2.54)$$

$$\mathcal{Z}_A \simeq \int_0^{k_M} dk_x \sqrt{1 - \frac{k_x^2}{k_M^2}} \int_0^\infty \frac{dk_y}{k_\perp^2} \sin^2 \left( k_y \frac{L}{2} \sin \varphi \right) \sqrt{1 + \frac{k_\perp^2}{k_m^2}} \frac{\sin^2(k_\perp/k_R)}{(k_\perp/k_R)^2} \quad (2.55)$$

where

$$k_m \equiv \frac{\omega_{pe}}{c} \sim \frac{1}{73.2m}, \quad k_M \equiv \frac{\Omega_i}{V_{pl}} \sim \frac{1}{14.2m}, \quad k_R \equiv \frac{1}{R} \sim \frac{1}{2m} \quad (2.56)$$

with the following ordering

$$\frac{1}{L} \ll k_m \ll k_M \ll k_R \quad (2.57)$$

In Eq. (2.55), the  $k_x$  integrand can be divided into two regions (assuming  $1/L \ll k_a \ll k_m$ )

1. Region 1 ( $\mathcal{Z}_{A1}$ ):  $k_a < k_x \leq k_M$ .
2. Region 2 ( $\mathcal{Z}_{A2}$ ):  $0 \leq k_x \leq k_a$ .

For the first region, changing the integration from  $k_y$  to  $k_\perp \equiv \sqrt{k_x^2 + k_y^2}$ , at fixed  $k_x$ ,  $\mathcal{Z}_{A1}$  reads

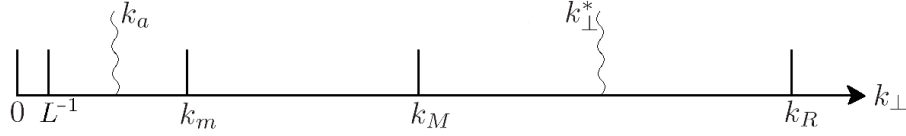
$$\mathcal{Z}_{A1} \simeq \int_{k_a}^{k_M} dk_x \sqrt{1 - \frac{k_x^2}{k_M^2}} I \quad (2.58)$$

where

$$I = \int_{k_x}^\infty \frac{dk_\perp}{2k_\perp} \frac{\sqrt{1 + k_\perp^2/k_m^2} \sin^2(k_\perp/k_R)}{\sqrt{k_\perp^2 - k_x^2} (k_\perp/k_R)^2} \quad (2.59)$$

and we set  $\sin^2(\frac{1}{2}k_y L \sin \varphi) \approx 1/2$ . Introducing  $k_\perp^*$ , such that  $k_a \leq k_x \leq k_M \ll k_\perp^* \ll k_R$ , the  $I$  integral can itself be divided into two parts (see Fig. 2.10):

1.  $I_a$ :  $k_x \leq k_\perp < k_\perp^*$ . We can here use  $\sin^2(k_\perp/k_R) / (k_\perp/k_R)^2 \approx 1$  for this zone.
2.  $I_b$ :  $k_\perp^* < k_\perp < \infty$ . In this broad range, we use the approximations  $k_\perp \gg k_x$  and  $k_\perp \gg k_m$ .

Figure 2.10: Characteristic regions for  $k_\perp$ .  $1/L \ll k_a \ll k_m \ll k_M \ll k_\perp^* \ll k_R$ .

For integrals  $I_a$  and  $I_b$ , we readily find

$$\begin{aligned} I_a &\simeq \int_{k_x}^{k_\perp^*} \frac{dk_\perp}{2k_\perp} \frac{\sqrt{1 + k_\perp^2/k_m^2}}{\sqrt{k_\perp^2 - k_x^2}} \\ &\simeq \frac{1}{2k_x} \cot^{-1} \left( \frac{k_x}{k_m} \right) + \frac{1}{4k_m} \left[ 2 \ln k_\perp^* + \ln \left( \frac{4}{k_m^2 + k_x^2} \right) \right] \end{aligned} \quad (2.60)$$

and

$$I_b \simeq \int_{k_\perp^*}^{\infty} \frac{dk_\perp}{2k_m k_\perp} \frac{\sin^2(k_\perp/k_R)}{(k_\perp/k_R)^2} \simeq \frac{1}{2k_m} \left[ \frac{3}{2} - \gamma - \ln \left( \frac{2k_\perp^*}{k_R} \right) \right] \quad (2.61)$$

Adding equations (2.60) and (2.61) we have

$$I \simeq \frac{1}{2k_m} \left\{ \frac{k_m}{k_x} \cot^{-1} \left( \frac{k_x}{k_m} \right) + \frac{3}{2} - \gamma + \ln \left[ \frac{k_R/k_m}{\sqrt{1 + (k_x/k_m)^2}} \right] \right\} \quad (2.62)$$

Introducing Eq. (2.62) in Eq. (2.58), and calling  $\bar{k} \equiv k_x/k_M$ , with  $\bar{k}_m \equiv k_m/k_M$  and  $\bar{k}_a \equiv k_a/k_M \ll \bar{k}_m$ , we can write

$$\begin{aligned} \mathcal{Z}_{A1} &\approx \frac{1}{2} \int_{\bar{k}_a}^1 \frac{d\bar{k}}{\bar{k}} \sqrt{1 - \bar{k}^2} \cot^{-1} \left( \frac{\bar{k}}{\bar{k}_m} \right) \\ &\quad + \frac{1}{2\bar{k}_m} \int_0^1 d\bar{k} \sqrt{1 - \bar{k}^2} \ln \left[ \frac{k_R e^{3/2 - \gamma}}{k_m \sqrt{1 + (\bar{k}/\bar{k}_m)^2}} \right] \end{aligned} \quad (2.63)$$

where we included the range  $0 \leq \bar{k} \leq \bar{k}_a$  in the second integral, where it makes a negligible contribution of order  $\bar{k}_a$ . Evaluating the  $\bar{k}$  integrals yields

$$\mathcal{Z}_{A1} \simeq \frac{\pi}{4} \left\{ \ln \left[ \frac{2\bar{k}_m}{\bar{k}_a (1 + \sqrt{1 + \bar{k}_m^2})} \right] + \frac{1}{2\bar{k}_m} \ln \left[ \frac{2\bar{k}_m e^{2 - \gamma} k_R}{k_m (1 + \bar{k}_m)} \right] \right\} \quad (2.64)$$

For the region 2 ( $0 \leq k_x \leq k_a$ ), introducing  $\kappa \equiv k_y/k_x$  and using  $k_z \ll k_M$ , we find

$$\mathcal{Z}_{A2} \approx \int_0^{\bar{k}_a} \frac{d\bar{k}}{\bar{k}} \int_0^\infty \frac{d\kappa}{1 + \kappa^2} \sin^2 \left( \frac{\bar{k} \Lambda \kappa}{2} \right) \quad (2.65)$$

where  $\Lambda \equiv k_M L \sin \varphi$ . We readily find

$$\int_0^\infty \frac{d\kappa}{1 + \kappa^2} \sin^2 \left( \frac{\bar{k} \Lambda \kappa}{2} \right) = \frac{\pi}{4} (1 - e^{-\bar{k} \Lambda}) \quad (2.66)$$

With  $1/L \ll \bar{k}_a$ , the resultant integral is

$$\mathcal{Z}_{A2} = \frac{\pi}{4} \int_0^{\bar{k}_a} \frac{d\bar{k}}{\bar{k}} \left(1 - e^{-\bar{k}\Lambda}\right) \simeq \frac{\pi}{4} [\ln(\Lambda e^\gamma) + \ln(\bar{k}_a)] \quad (2.67)$$

Adding equations (2.2.8) and (2.67) we have

$$\mathcal{Z}_A \simeq \frac{\pi}{4} \left[ \ln(\bar{k}_m \Lambda e^\gamma) + \frac{1}{2\bar{k}_m} \ln \left( \frac{2\bar{k}_m e^{2-\gamma} k_R}{k_m (1 + \bar{k}_m)} \right) \right] \quad (2.68)$$

To obtain the Alfven impedance radiation for a spinning tether, we now averaging  $\mathcal{Z}_A$  over one revolution. Using Eq. (2.68) in Eq. (2.54) and  $\Lambda \propto \sin \varphi$ , yielding

$$\frac{2}{\pi} \int_0^{\pi/2} d\varphi \ln(k_M L \sin \varphi) = \ln \left( \frac{k_M L}{2} \right) \quad (2.69)$$

the averaged impedance has the final compact form

$$Z_A \approx \frac{2V_A}{c^2} \left\{ \ln \left[ \frac{e^\gamma L \omega_{pe}}{2c} \right] + \frac{1}{2} \frac{\Omega_i c}{V_{pl} \omega_{pe}} \ln \left[ \frac{2V_{pl} e^{2-\gamma}}{R \Omega_i} \right] \right\} \quad (2.70)$$

To compare the impedance above with equation (19') in [94],

$$Z_A = \frac{2V_A}{c^2} \ln \left( \frac{2e^{\gamma-1} L \Omega_i}{V} \right) \quad (2.71)$$

for the impedance at LEO, note first that in Eq. (2.70), the ratio  $(c/\omega_{pe}) / (V_{pl}/\Omega_i) \simeq 73.2\text{m}/14.2\text{m} \simeq 5.2$  is moderately large. In LEO, however, it is two orders of magnitude smaller because  $\Omega_i$  and  $N_e$  are about 10 times smaller and  $10^2$  times larger, respectively; this made the R-logarithm term, which was actually ignored in [94], negligible. Secondly, if one moved from condition  $\omega_{pe}/c \ll \Omega_i/V_{pl}$  to  $\Omega_i/V_{pl} \ll \omega_{pe}/c$ , the length ratio entering the first logarithm for  $Z_A$  in Eq. (2.70) would change from  $L\omega_{pe}/c$  to  $L\Omega_i/V_{pl}$ . In addition, in Eq. (2.71) for LEO, the relative orbital velocity (which is about the orbital velocity  $V$ ) does figure instead of  $V_{pl}$  because of the differences in orbital geometry, i. e., equatorial instead of polar (at  $\lambda = 0^\circ$ ). Finally, the factor  $2/e$  in the logarithm of Eq. (2.71), i. e., the small  $\ln(2/e)$  contribution to the large logarithm in  $Z_A$ , which is missing from Eq. (2.70), was lost in the approximation leading to Eq. (2.86); on the other hand, the  $1/2$  factor in Eq. (2.70) is due to the spinning tether, not used in LEO.



### 2.2.7.2 The radiation impedance at the polar caps

In the polar Jovian case, we have  $\omega = k_y V_{orb}/\sqrt{2} < \Omega_i$ ,  $k_y$  thus being less than a maximum  $k_M = \sqrt{2}\Omega_i/V_{orb}$ . The integral in Eq. (2.47) is here written as

$$Z_A = \frac{8V_A}{\pi c^2 \sqrt{1 + (V_A/c)^2}} \int_0^{\pi/2} \frac{d\varphi}{\pi/2} \mathcal{Z}_A \quad (2.72)$$

where

$$\mathcal{Z}_A = \int_0^{k_M} dk_y \frac{\sqrt{1 - k_y^2/k_M^2} \sin^2(\frac{1}{2}k_y L \sin \varphi)}{\sqrt{1 - \tilde{V}_A^2 k_y^2/k_M^2}} \int_0^\infty \frac{dk_x}{k_\perp^2} \sqrt{1 + \frac{k_\perp^2}{k_m^2}} \frac{\sin^2(k_\perp/k_R)}{(k_\perp/k_R)^2} \quad (2.73)$$

$$k_m \equiv \frac{\omega_{pe}}{c} \simeq \frac{1}{2.37 \text{ Km}} \quad (2.74)$$

$$k_M \equiv \sqrt{2} \frac{\Omega_i}{V_{orb}} \simeq \frac{1}{118.24 \text{ m}} \quad (2.75)$$

$$\tilde{V}_A^2 \equiv \frac{V_A^2}{V_A^2 + c^2} \simeq 0.18 \quad (2.76)$$

Using the same procedure as in the equatorial case, we change the integration from  $k_x$  to  $k_\perp = \sqrt{k_y^2 + k_x^2}$  at fixed  $k_y$ , and evaluate first the  $k_\perp$  integral, which reads

$$\mathcal{Z}_A \simeq \int_0^{k_M} dk_y \frac{\sqrt{1 - k_y^2/k_M^2}}{\sqrt{1 - \tilde{V}_A^2 k_y^2/k_M^2}} \sin^2\left(k_y \frac{L}{2} \sin \varphi\right) \cdot I(k_y) \quad (2.77)$$

where

$$I(k_y) \simeq \frac{1}{k_m} \left[ \frac{k_m}{k_y} \cot^{-1}\left(\frac{k_y}{k_m}\right) + \ln \left\{ \frac{k_R/k_m e^{3/2-\gamma}}{\sqrt{1 + (k_y/k_m)^2}} \right\} \right] \quad (2.78)$$

where  $I(k_y)$  is just two times  $I$  as given in Eq. (2.62) with a  $k_x \rightarrow k_y$  change.

Calling  $\mathcal{Z}_{AI}$  and  $\mathcal{Z}_{AII}$  the contributions of the first and second terms in the bracket of Eq. (2.78) to the impedance in Eq. (2.77), we readily find

$$\mathcal{Z}_{AII} \simeq \frac{k_M}{2k_m} \int_0^1 d\bar{k} \frac{\sqrt{1 - \bar{k}^2}}{\sqrt{1 - \tilde{V}_A^2 \bar{k}^2}} \ln \left\{ \frac{k_R/k_m e^{3/2-\gamma}}{\sqrt{1 + (k_y/k_m)^2}} \right\} \quad (2.79)$$

where we set  $\sin^2(\frac{1}{2}k_y L \sin \varphi) \simeq 1/2$  and wrote  $k_y/k_M \equiv \bar{k}$ . With the approximation  $1/\sqrt{1 - \tilde{V}_A^2 \bar{k}^2} \approx 1 + \tilde{V}_A^2 \bar{k}^2/2$ , Eq. (2.79) yields

$$\mathcal{Z}_{AII} \simeq \frac{\pi k_M}{8 k_m} \left\{ \ln \left( \frac{2 e^{2-\gamma}}{R k_M} \right) + \frac{\tilde{V}_A^2}{8} \ln \left( \frac{2 e^{\frac{5}{4}-\gamma}}{k_M R} \right) \right\} \quad (2.80)$$

For  $\mathcal{Z}_{AI}$ , where small  $k_y/k_M$  values are dominant, we must retain the full square sine factor. Defining  $\tilde{k} \equiv \frac{1}{2}k_y L \sin \varphi$ , we have

$$\mathcal{Z}_{AI}(\tilde{k}_m) \simeq \int_0^\infty \frac{d\tilde{k}}{\tilde{k}} \sin^2 \tilde{k} \cdot \cot^{-1} \left[ \frac{\tilde{k}}{\tilde{k}_m} \right] \quad (2.81)$$

As this integral converges rapidly at large  $\tilde{k}$  values, we set  $\tilde{k}_M \simeq \infty$ , and approximated the square root factors in Eq. (2.77) by unity. From Eq. (2.81) and using  $\mathcal{Z}_{AI}(0) = 0$ , we find

$$\frac{d\mathcal{Z}_{AI}}{d\tilde{k}_m} = \int_0^\infty d\tilde{k} \frac{\sin^2 \tilde{k}}{\tilde{k}_m^2 + \tilde{k}^2} = \frac{\pi}{4\tilde{k}_m} (1 - e^{-2\tilde{k}_m}) \quad (2.82)$$

$$\mathcal{Z}_{AI} = \frac{\pi}{4} \left\{ \ln(2\tilde{k}_m) + \gamma + E_1(2\tilde{k}_m) \right\} \simeq \frac{\pi}{4} \ln(Le^\gamma k_m \sin \varphi) \quad (2.83)$$

where we used an approximation of the exponential integral roughly valid for its argument above unity.

Introducing Eq. (2.83) and Eq. (2.80) in Eq. (2.72), and averaging over a spin period, we finally find

$$\begin{aligned} Z_A \simeq & \frac{2V_A}{c^2 \sqrt{1 + V_A^2/c^2}} \left\{ \ln \left( \frac{Le^\gamma \omega_{pe}}{2c} \right) \right. \\ & \left. + \frac{\Omega_i c}{\sqrt{2}\omega_{pe} V_{orb}} \left[ \ln \left( \frac{\sqrt{2}V_{orb} e^{2-\gamma}}{R \Omega_i} \right) + \frac{\tilde{V}_A^2}{8} \ln \left( \frac{\sqrt{2}V_{orb} e^{5/4-\gamma}}{R \Omega_i} \right) \right] \right\} \quad (2.84) \end{aligned}$$

One would recover Eq. (2.70) by first setting  $V_A^2/c^2$  small and replacing  $V_{orb}/\sqrt{2}$  with  $V_{pl}$ . Table 2.1 shows a summary of characteristic values of the ambient plasmas and several parameters for LEO, and Jovian equator and polar caps.

### 2.2.8 The general Alfvén radiation impedance

Both sections 2.2.7.1 and 2.2.7.2, give the Alfvén radiation impedance at equator and polar caps, respectively, and suggest the appropriate technique to determine the general

Alfven radiation impedance. As a summary, results of impedance versus tether length for LEO, and Jovian equator and polar cases are illustrated in Fig. 2.11. In the present section, the Alfven radiation impedance is determined for Low Jovian Orbit and we find a general law for Juno.

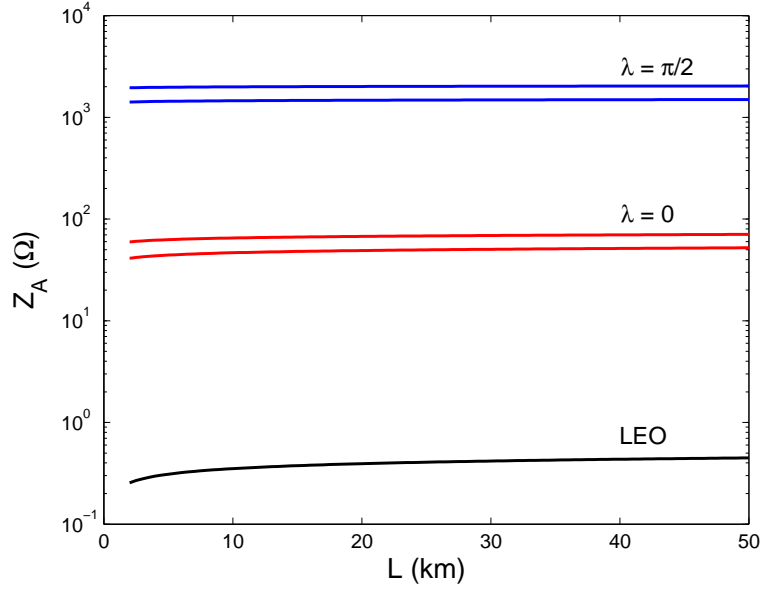


Figure 2.11: Impedance versus tether length for the LEO, and Jovian equatorial and polar cases. We use values given in Table 2 for  $R = 0.5$  and 4 m for the upper and lower curves, respectively.

| Parameters             | LEO              | Jupiter ( $\lambda = 0^\circ$ ) | Jupiter ( $\lambda = 90^\circ$ ) |
|------------------------|------------------|---------------------------------|----------------------------------|
| $V_{orb} (km/s)$       | 7.3              | 56.9                            | 40.2                             |
| $V_{pl} (km/s)$        | -                | 13.9                            | 0                                |
| $V_A (km/s)$           | 300              | $17.3 \cdot 10^3$               | $14.6 \cdot 10^4$                |
| $\Omega_i (s^{-1})$    | $2.0 \cdot 10^2$ | $9.4 \cdot 10^2$                | $2.3 \cdot 10^2$                 |
| $\Omega_e (s^{-1})$    | $5.9 \cdot 10^6$ | $5.6 \cdot 10^7$                | $1.4 \cdot 10^7$                 |
| $\omega_{pi} (s^{-1})$ | $1.2 \cdot 10^3$ | $1.6 \cdot 10^4$                | $4.8 \cdot 10^2$                 |
| $\omega_{pe} (s^{-1})$ | $3.4 \cdot 10^7$ | $3.9 \cdot 10^6$                | $1.2 \cdot 10^5$                 |
| $k_m^{-1}(m)$          | 8.8              | 73.2                            | $2.37 \cdot 10^3$                |
| $k_M^{-1}(m)$          | 35.6             | 14.2                            | 118.24                           |

Table 2.1: Summary of plasma and velocity characteristic values for LEO and the first orbit in Juno ( $\Psi = 0$ ). We use  $r_p = 1.09 R_J$ .

For Low Jovian Orbit, considering (2.43) and (2.47), and assuming  $V_A^2 \ll c^2$ , the Alfven radiation impedance reads

$$Z_A = \frac{V_A}{\pi^2 c^2} \int \frac{d\mathbf{k}_\perp}{k_\perp^2} \sqrt{1 - \frac{k_x^2}{k_M^2}} \sqrt{1 + \frac{k_\perp^2}{k_m^2} \frac{\sin^2(k_\perp R)}{(k_\perp R)^2}} \times \int_0^{2\pi} d\varphi \sin^2 \left[ \frac{L}{2} (k_y \sin \varphi + k_x \cos \varphi) \right], \quad (2.85)$$

where  $k_m \equiv \omega_{pe}/c$ ,  $k_M \equiv \Omega_i/\tilde{V}_{rel}$ , and  $\tilde{V}_{rel}$  is  $V_{rel}^{ret,pro}$  here again. Since the  $\varphi$ -integral is  $\pi \cdot [1 - J_0(k_\perp L)]$ , equation (2.85) yields

$$\frac{\pi c^2}{4V_A} Z_A \equiv \mathcal{Z}_A = \int_0^{k_M} dk_x \sqrt{1 - \frac{k_x^2}{k_M^2}} \times \int_0^\infty \frac{dk_y}{k_\perp^2} \sqrt{1 + \frac{k_\perp^2}{k_m^2} \frac{\sin^2(k_\perp R)}{(k_\perp R)^2}} [1 - J_0(k_\perp L)].$$

Following a procedure used in section 2.2.7, we use the ordering  $1/L \ll k_m \ll k_M \ll 1/R$  to divide the  $k_x$  integrand into two regions:

1. Region 1 ( $\mathcal{Z}_{A1}$ ):  $k_{int} < k_m < k_x \leq k_M$ .
2. Region 2 ( $\mathcal{Z}_{A2}$ ):  $0 \leq k_x \leq k_{int}$ .

with the intermediate value  $k_{int}$  satisfying  $1/L \ll k_{int} \ll k_m$ .

For the first region, we use equations (2.58-2.2.8) from section 2.2.7, with  $1 - J_0(k_\perp L) \approx 1$  and  $\bar{k} \equiv k_x/k_M$ , yielding

$$\mathcal{Z}_{A1} \simeq \frac{\pi}{2} \left\{ \ln \left[ \frac{2\bar{k}_m}{\bar{k}_{int} (1 + \sqrt{1 + \bar{k}_m^2})} \right] + \frac{1}{2\bar{k}_m} \ln \left[ \frac{2\bar{k}_m e^{2-\gamma}}{k_m R (1 + \bar{k}_m)} \right] \right\},$$

where  $\bar{k}_m = k_m/k_M$  and  $\bar{k}_{int} = k_{int}/k_M$ .

For region 2 ( $0 \leq k_x \leq k_{int}$ ), introducing  $\kappa \equiv k_y/k_x$  and using  $k_x \ll k_M$ , we find

$$\mathcal{Z}_{A2} \approx \int_0^{\bar{k}_{int}} \frac{d\bar{k}}{\bar{k}} \times I(\bar{k}\Lambda), \quad I(\bar{k}\Lambda) = \int_0^\infty \frac{d\kappa}{1 + \kappa^2} \left[ 1 - J_0(\bar{k}\Lambda \sqrt{1 + \kappa^2}) \right], \quad (2.86)$$

where  $\Lambda \equiv k_M L$ . Using  $I(0) = 0$ , we find

$$\frac{dI}{d(\bar{k}\Lambda)} = \int_0^\infty \frac{d\kappa}{\sqrt{1 + \kappa^2}} J_1(\bar{k}\Lambda \sqrt{1 + \kappa^2}) = \frac{1}{\bar{k}\Lambda} \sin(\bar{k}\Lambda),$$

$$I = Si(\bar{k}\Lambda) ,$$

where  $Si$  is the sine integral. Carrying out the  $\bar{k}$ -integral approximately, (2.86) yields

$$\mathcal{Z}_{A2} \simeq \frac{\pi}{2} \left\{ \ln(\Lambda e^\gamma) + \ln(\bar{k}_{int}) \right\} .$$

Adding  $\mathcal{Z}_{A1}$  and  $\mathcal{Z}_{A2}$ , the impedance finally reads

$$Z_A \approx \frac{2V_A}{c^2} \left\{ \ln\left(\frac{Le^\gamma\omega_{pe}}{2c}\right) + \frac{\Omega_i c}{2\tilde{V}_{rel}\omega_{pe}} \ln\left(\frac{2\tilde{V}_{rel}e^{2-\gamma}}{R\Omega_i}\right) \right\} , \quad (2.87)$$

independent of  $k_{int}$  choice.

For Juno, recalling Eq. (2.53), can be solved by a general law. Note that  $k_\perp$  in the integral in (2.53) here ranges all the way down to zero, as opposite the  $k_\perp$ -integral in Eq. (2.48). Carrying out the integral given by (2.49) we obtain  $\mathcal{Z}_\varphi^J = [1 - J_0(k_\perp L \sin \alpha)] \pi/2$ . The FM radiation impedance result for Juno in section 2.2.6 showed a dependence on a relative velocity  $\tilde{V}_{rel} = \sqrt{V_{orb,y}^2 + V_{pl}^2}$ . This suggests that some effective relative velocity  $\tilde{V}_{rel}$  should appear in a general Alfven radiation impedance, using again  $\sqrt{V_{orb,y}^2 + V_{pl}^2} |\cos(\zeta - \alpha)|$ , in Juno. Complete numerical results fit (within 10%, roughly) an analytical law

$$Z_A \simeq \frac{2V_A}{c^2 \sqrt{1 + (V_A/c)^2}} \left\{ \ln\left(\frac{Le^\gamma\omega_{pe}}{2c}\right) + \frac{\Omega_i c}{2\omega_{pe}\tilde{V}_{rel}} \left(1 + \frac{V_A^2/8}{V_A^2 + c^2}\right) \ln\left(\frac{2\tilde{V}_{rel}e^{2-\gamma}}{R\Omega_i}\right) \right\} . \quad (2.88)$$

This law, which is shown in Figure 2.12, recovers previous results for  $\psi = 0$ , and  $\lambda = 0$  and  $\pi/2$ , where  $\tilde{V}_{rel} = V_{pl}$  and  $V_{orb}/\sqrt{2}$  respectively [87]. At moderate  $\lambda$  values, the Alfven impedance in Figure 2.12 shows close results for first and last orbit. For large  $\lambda$  values, the impedance for  $\psi = 0$  increases more sharply than the last orbit case.

The Alfven radiation impedances for Juno and LJO given by (2.87) and (2.88), respectively, are also similar except for the relative velocities involved, and they show a dominant  $R$ -logarithmic dependence, whereas in LEO, the Alfven impedance in equation (19') from [94] was independent of  $R$ . Notice that the ratio  $\Omega_i c / 2\omega_{pe} \tilde{V}_{rel}$  in (2.87) and (2.88) makes the contribution of the  $R$ -logarithm term larger than the  $L$ -logarithm

term. This result was not apparent in the particular results for Juno in reference [87]. Figure 2.13 shows the Alfven radiation impedance for both prograde and retrograde LJO. Since  $V_{rel}^{pro} < V_{rel}^{ret}$ , the Alfven impedance is largest in a prograde orbit.

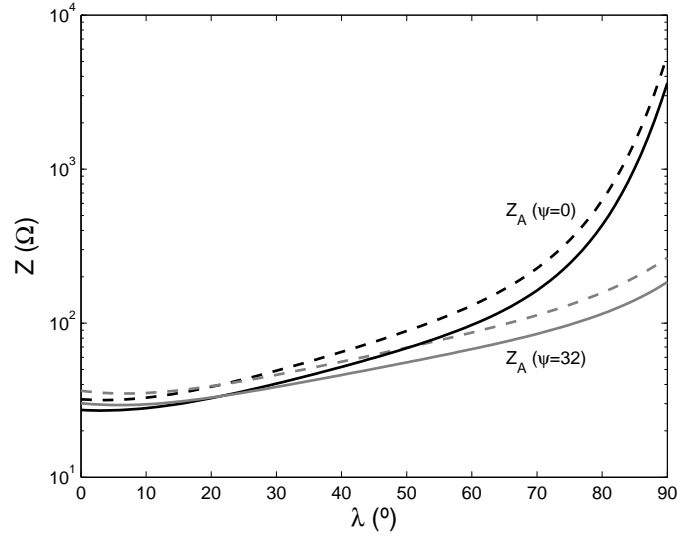


Figure 2.12: Alfven radiation impedance from (2.88) for the first orbit (black) and the last Juno-like orbit (gray). Considering  $L = 10$  km, the impedance for  $R = 4$  m and  $R = 0.5$  m is represented by solid and dashed line, respectively.

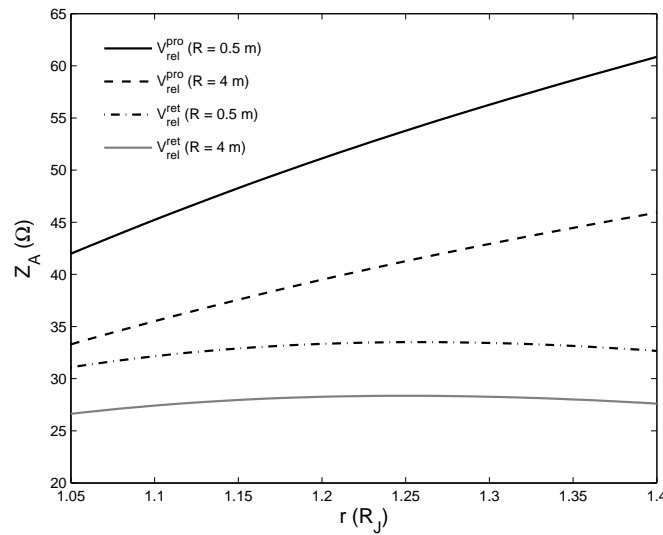


Figure 2.13: The Alfven radiation impedance is represented for both prograde ( $V_{rel}^{pro}$ ) and retrograde ( $V_{rel}^{ret}$ ) Low Jovian Orbit, considering 10 km tether for  $R = 4$  m and 0.5 m.

The ion composition close to Jupiter is not well-known. Considering an hypothetical hydrogen-dominated inner plasmasphere, the Alfven impedance would increase two orders of magnitude whereas FM impedance would weakly decrease as a function of  $\sqrt{m_i}$ .

### 2.2.9 Bare tether radiation impedance

We had considered insulated tethers throughout the analysis. We will now briefly discuss a bare tether impedance. An optimal anodeless bare-tether generator collects electrons along some anodic (positively biased) segment of length  $l_a \sim \frac{1}{7}L$  [93]. To just estimate the bare tether impedance both in Juno and LJO we keep a spherical contactor of radius  $R$  model at the cathodic end, while considering a cylindrical sheath of size  $b$  surrounding the anodic segment. The single (cathodic) contactor here contributes half the FM impedance in (2.51). The anodic segment in turn yields a term smaller by the factor  $R^2/bl_a$ . In equation (2.44), the current source also reads  $I_s \sim I_{OML} \sim l_a 2r_t e N_e \sqrt{2e\Phi_p/m_e}$ , where  $r_t$  is tether radius and tether bias  $\Phi_p \sim V_{rel}Bl_a$  varies along the segment. With  $b \sim \lambda_D \sqrt{e\Phi_p/k_B T_e}$  and a Jovian  $\lambda_D$  much greater than any reasonable tether radius [34][95], equation (2.44) itself yields  $R^2 \sim l_a r_t \sqrt{e\Phi_p/k_B T_e} \ll l_a b$ . The FM impedance in equation (2.51) is then roughly reduced by half. For Alfven waves, the R-logarithm term in equations (2.87) and (2.88) is similarly reduced, while the small L-logarithm term, written approximately as  $\ln(l_a e^\gamma \omega_{pe}/2c) \simeq \ln(Le^\gamma \omega_{pe}/2c) - \ln 7$ , just keeps a small correction. The bare-tether impedance can thus be taken as reduced by half for either mode in both LJO and Juno.

### 2.2.10 Discussion

In addition to its use for generating electric power, a tether can serve as antenna to communicate information to some orbiter-link. The tether conductor can be a good signal emitter. Additionally, the large radiative impedance of the tether will affect substantially the current in its overall circuit.

The Alfven radiation impedance, for the first Juno-like orbit, at both Jovian equator and polar caps was recently calculated in reference [87]. In Ref. [90] we carried out a broader analysis of the radiation impedance of a tether, considering both Alfven and FM modes and a range conditions: characteristic arc of two Juno-like orbits, and a prograde or retrograde Low Jovian Orbit (LJO). In all cases, the Alfven velocity is large when compared to the LEO case, because of the low dense, highly-magnetized Jovian plasma; this results in a much larger Alfven impedance. Additionally, a logarithmic term depending on plasma contactor size  $R$ , which does not appear in the LEO case, contributes dominantly to the impedance, as against a logarithmic term dependent on tether length  $L$ , which is the only one in LEO. The large contribution of the  $R$ -logarithm term to the Alfven impedance was showed in Figure 4 in reference [87], and it was not noticeable there. Additionally, in section 2.2.6 is shown that the analytical law given in (2.88) recovers results of [87] for the two extreme cases studied there (the equations (56) and (70) in reference [87]).

In both missions, the FM voltage drop given by equation (2.51) is also much larger than in the LEO case, because of both orbital and Jovian plasma parameters, i.e. both  $T_e$  and the relative velocity  $\tilde{V}_{rel}$  are much larger, and sulphur ions prevailing in Jupiter are heavier than oxygen ions. The typical FM voltage drop for both Juno and LJO would be two orders higher than in LEO ( $\Delta V_{FM}^{LEO} \sim 0.4$  V). The FM radiation power  $Z_{FM} I_s^2$  will dominate Alfven-mode power, except at large currents.

In LJO, the Alfven radiation impedance is higher for a prograde orbit ( $V_{rel}^{pro}$ ) as against a retrograde orbit, whereas the opposite applies to the FM impedance, as shown in Figures 2.9 and 2.13. The radiation impedance for both missions is mainly dependent on the relative velocities which are characterized by the orbital plane where the tether lies: polar for Juno and equatorial for LJO. Results on the LEO case for slow-extraordinary (SE) impedance suggest that the SE contribution will be negligible in both Juno and LJO [94]. Regarding bare tether impedance, it is reduced by about half in both Jovian missions.

In Juno-like orbit, power generation results for bare-tether mission with  $r_p = 1.06R_J$  and eccentricity  $e = 0.947$  were given in Bombardelli et al., 2008 [14]. For a  $L = 10$



km tape-tether of 5 cm width, the maximum power generated would be  $\sim 10^2$  kW at the Jovian equator. The power decreases with  $\nu$ , vanishing at  $\nu = \pi/2$ . In LJO, power below  $1.4 R_J$  is determined by [18]; for a  $L = 3$  km tape-tether with a 3 cm width, the maximum load-power is  $\sim 0.3$  kW at  $1.4 R_J$  and  $\sim 4$  kW at  $1.1 R_J$ .

Radiated power will be  $P_{rad} = Z_A I_s^2 + \Delta V_{FM} I_s$ . For 1 A of current flowing in an active tether of 10 km length and a contactor radius  $R \sim 2$  m, the radiated power, mostly in Alfvén waves, would be  $P_{rad} \sim 4$  kW at  $\psi = 0$  and  $\lambda = \pi/2$ . An onboard power supply is required to produce current in opposition to the motional potential ( $E_m L \sim VBL \sim 10$  kV),  $E_m$  being the motional electric field. For 10 A of current flowing in the conductor, the power radiated would be  $\sim 0.4$  MW at  $\psi = 0$  and  $\lambda = \pi/2$ . Similarly, in LJO, 1 A of current flowing along the tether would produce  $\sim 100$  W of radiated power for both retrograde and prograde orbits.

Switching the cathodic contactor off, a tether floats electrically, current vanishing at each end. A tether is then negatively biased except over a small fraction of its length, so as to allow enough ion current to balance electron collection. Ambient sulphur/oxygen ions impacting the tape both leave as neutrals and liberate additional secondary electrons, which are accelerated along magnetic field lines and could excite neutral molecules in the upper Jovian atmosphere, generating auroral emissions. Additionally, switching the contactor off would produce a large surge in both current and radiated power, setting up bias/current pulses along its length which are capable of emitting signals under a transmission line modeling [103]. It was recently suggested that current modulation in tethers might generate nonlinear, low frequency wave structures attached to the spacecraft. A magnetic pumping mechanism, through magnetic oscillations in the near field of the radiated wave, would result in a parametric instability [83].

There are three main results obtained here. First, the voltage drop for FM emission in Jupiter is 30-100 times greater than in LEO. Secondly, Alfvén impedance in Jupiter is several orders of magnitude greater than in LEO. Finally, impedance of Jovian tethers are reduced by about one half if stripped of insulation. Thermal effects in the Alfvén radiation impedance are briefly studied in appendix A.

## 2.3 Generation of auroral effects in Jupiter and grain-tether interaction

### 2.3.1 Introduction

In references [66] and [98] the use of a conductive bare tape electrically floating in Low Earth Orbit as an effective electron beam source to produce artificial auroral effects was considered. In reference [18], a two-stage two-tether mission was considered. Following capture as described in [100], the SC tether would have its apoapsis progressively lowered to finally reach a circular orbit at the periapsis of the capture orbit, about  $1.3 - 1.4$  times the Jovian radius  $R_J$ , skipping moon flybys as considered in [101] to reduce dose accumulation. In the second stage, a short segment of the original tether makes its SC to slowly spiral inward, in a controlled manner, keeping below the belts throughout while generating power on board for science applications, for which the proximity to Jupiter, under the evolving in-situ conditions surrounding the SC, offers a world of opportunities [102].

A basic mission goal would be determining the structure and dynamics of the Jovian atmosphere, which is actually one goal of the Europa Jupiter System Mission (EJSM) too. Space and time resolved observations, essential for understanding transport processes, would be possible. Data registered over many months would allow studying atmospheric variability over different time scales. This includes clarifying how and why the stratospheric thermal structure varies with time, and tracking the evolution of lightning storms [5]. Measurements so close to Jupiter's surface would also allow increasing our knowledge of its interior. This would include accurate, high resolution determination of gravity and magnetic fields, and determining the bulk abundance of water. Accurate mapping of the gravity field could show non-hydrostatic pressure effects where water was absent. Measuring brightness temperature at millimeter wavelengths at close range would give water abundance without the ambiguity of remote sensing [5].

The radial range  $1.3 - 1.4R_J$  contains both the inner region of the Halo ring and the 2:1 Lorentz resonance ( $\Omega_{orb} = 2\Omega_j$  or  $a = a_s/2^{2/3}$ ). The 2:1 Lorentz resonance, basically due to a Schmidt coefficient  $g_2^2 \sim 0.4 - 0.5$  Gauss, is the strongest by far and is



Under the impact of attracted ions, the tether will emit secondary electrons at certain yield  $\gamma$  and form a beam traveling along magnetic field lines, with particle and energy flux growing with distance  $l$  from tether top [98]. The beam electron flux reads

$$\Phi_b(l) = N_e \Omega_e w \sqrt{\frac{m_e}{m_i}} \frac{\gamma (e E_t l)}{2\pi \cos(dip)}, \quad (2.89)$$

which is much weaker than the ambient thermal flux; the beam/ambient density ratio is also very small. The dip of a simple-dipole vanishes at the Equator but the angle  $\varphi$  of the rotating tether away from the vertical plays the role of the dip; orbit and spin periods (over 3 hours and, say, around 10 minutes respectively) are reasonably disparate. The pitch-angle  $\alpha$  distribution is then [98]

$$\frac{\Phi_b(h, \alpha)}{\Phi_b(h)} = \frac{2}{\pi \sqrt{\sin^2 \alpha - \sin^2 dip(\varphi)}}. \quad (2.90)$$

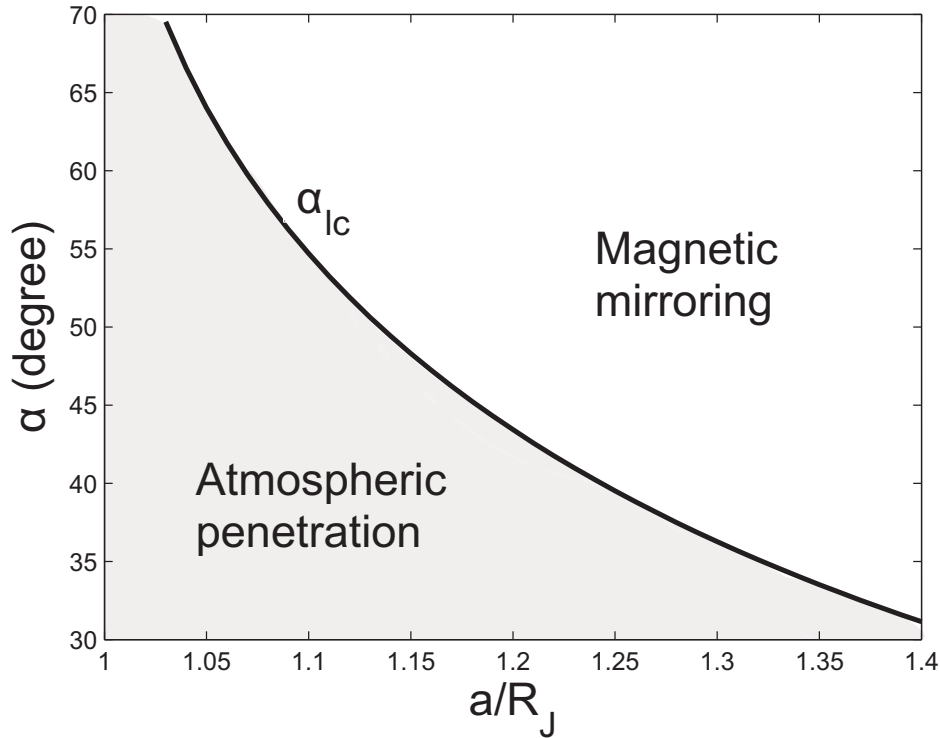


Figure 2.15: Loss-cone pitch angle  $\alpha_{lc}$  versus  $a/R_J$ , here representing magnetic-shell parameter.

For the high altitudes of interest, beam electrons with high pitch would bounce back as trapped electrons whereas low-pitch electrons would imprint auroral lights along a

beam track at the upper atmosphere. The pitch range in the beam is  $dip(\varphi) < \alpha < \alpha_{lc}$  where the loss-cone pitch  $\alpha_{lc}(a)$  shown in Figure 2.15 follows from the no-tilt, dipole  $B$  model

$$\sin^4 \alpha_{lc} = \frac{R_J^6}{a^5 (4a - 3R_J)}. \quad (2.91)$$

For the high altitudes of interest, beam electrons with high pitch would bounce back as trapped electrons whereas low-pitch electrons would imprint auroral lights along a beam track at the upper atmosphere. Bare tethers at Jupiter would require spinning because of the weak gravity gradient. During each half spin-period with the hollow cathode at the anodic end, the tether will be electrically floating, with current vanishing at both ends. This would result a periodic generation of auroral effects in the upper Jovian atmosphere (Ref. [93]). In general, the dip in Eq. (2.89) is the angle between magnetic field and plane perpendicular to the tether, satisfying

$$\sin dip = \frac{\mathbf{u}_t \cdot \mathbf{B}}{B}, \quad (2.92)$$

where  $\mathbf{u}_t = \mathbf{u}_t \cos \phi + \mathbf{u}_\Lambda \sin \phi$ , being  $\phi$  the angle of the rotating tether away from the vertical; orbit and spin periods (over 3 hours and around 10 minutes respectively) are reasonably disparate. Using the VIP4 Jovian magnetic-field model, the spherical harmonic expansion for the magnetic field reads

$$\mathbf{B} \approx -\nabla \left\{ R_J \sum_{m=0}^s P_s^m(\cos \theta) [g_s^m \cos(m\Lambda) + h_s^m \sin(m\Lambda)] \right\}, \quad (2.93)$$

with  $g/h$ , Schmidt coefficients determined from in-situ observations on past missions (see table 24.1 in reference [5]);  $P_s^m$ , Schmidt-normalized associate Legendre functions; and  $\Lambda$ , longitude in Jupiter System III reference system. Here dip angle varies because both the tether rotates and the multipole  $\mathbf{B}$  field varies along the orbit,

$$dip = \sin^{-1} \left[ \frac{B_r \cos \phi + B_\Lambda \sin \phi}{B} \right]. \quad (2.94)$$

Figure 2.16 shows how the penetration range in the e-beam changes with both Jovian longitude and  $\phi$ .

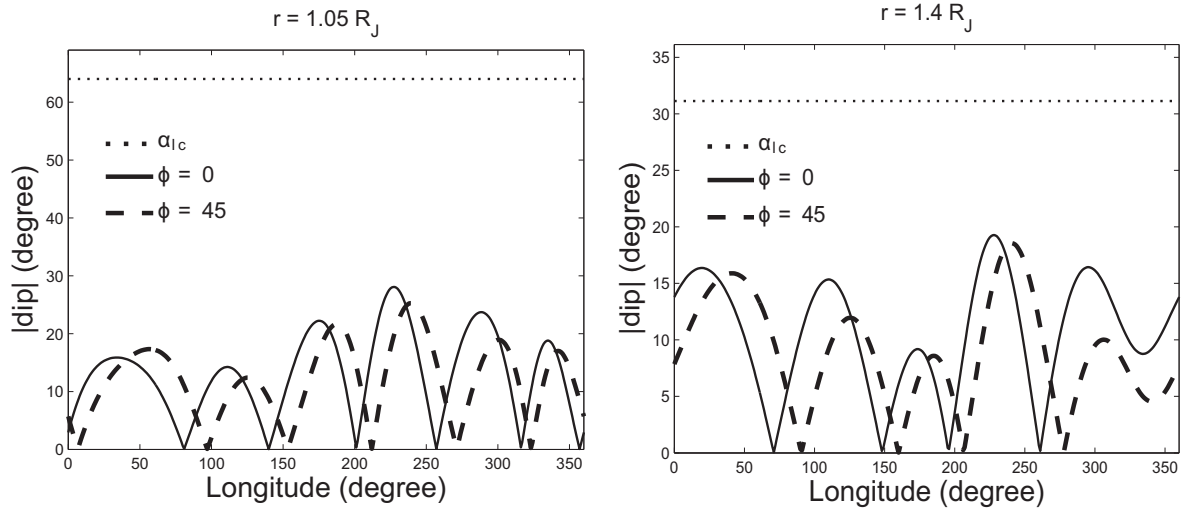


Figure 2.16: Left and right figures represent the dip angle for  $1.05 R_J$  and  $1.4 R_J$  respectively; e-beam penetration occurs for range  $|dip(\phi)| < \alpha < \alpha_{lc}$ .

### 2.3.3 Discussion

In the first stage of LJO mission, a 50 km tether length might get a spacecraft to a circular orbit below the radiation belts with a reasonable radiation dose. A characteristic value for the electromotive force would reach near 0.25 MV for  $L = 50$  km. Attracted electrons would reach the anodic segment of the tether with relativistic velocities. The Orbital Motion Limited theory for tether current collection was recently extended to the relativistic regime [85]. In the capture stage, too many passes around the perijove are required to reduce the apojove. This may result in high belt-electron fluxes and accumulated radiation dose. The penetration depth of 0.2 MeV electrons in aluminum is about 0.25 mm [43] for a 50 km tether length, which clearly exceeds over the 0.05 mm of the thickness suggested. For  $L = 10$  km the maximum electron energy would be reduced to about 0.04 MeV, and the penetration depth is just 0.01 mm [84].

In the second stage of the proposed LJO mission, the tether is cut, retaining a segment that is one order of magnitude smaller, which makes the SC to slowly spiral inward over many months while generating large power on board; with single hollow-cathode operation, the tether will electrically float every half spin period. Interesting science opportunities arise for missions below  $1.4 R_J$ , where radiation poses no problem. These include nearby high-resolution observations, over long times, of Jupiter's

atmosphere and interior; in situ measurements of charged grains by a dust detector; and auroral sounding of Jupiter's upper atmosphere. Both figures 2.15 and 2.16 show the range more effective to produce atmosphere penetration of the e-beam for  $a$  and Jovian longitude, respectively. .

## 2.4 Stability analysis for dusty plasmas under grain charge fluctuations

### 2.4.1 Introduction

A dusty plasma can be roughly defined as a normal electron-ion plasma with an additional charged, micro-sized grains component. Dusty plasmas appear in a great variety of systems in space. The presence of charged grains in interstellar clouds, comets, planetary rings and Earth's atmosphere are well-known [111]. The exploration of outer planets has revealed these charged grains; both Cassini and Galileo missions reveal a vast information of Jovian dust stream particles. Additionally, as it is mentioned in the previous section 2.3, interplanetary meteoroids and charged grains pose a problem for both interplanetary missions and planetary exploration. The potential impact risks might be reduced if we know both their population and behavior. The large data collected shown the relevance of the dust charge, which controls a set of both collective and individual behaviors of the whole plasma [5]. Dust charging has been intensively studied by several authors with the OML theory [2, 19, 75, 115]. As it is shown in the previous chapter the OML theory has been extended to cylindrical symmetries by others authors [33, 56, 57, 59, 95, 99]. Recently, some works have reported the importance of the electron and ion velocity distribution functions in addressing the description of plasma stability analysis under the frame of plasma fluid description including dust charge fluctuation [65, 117]. In several plasma scenarios where the existence of a high electric field may accelerate electrons up superthermal velocities, a non-Maxwellian distribution function might give the correct description [72]. We analyze the effect of kappa distribution function on the collective plasma behavior [30, 89]. A linear analysis of perturbed fluid equations with dust charge fluctuation is considered for both infinite

and finite grain mass.

### 2.4.2 Non-Maxwellian distributions and charging model

A dusty plasma could be described by its species distribution functions  $f_j(\mathbf{v}, \mathbf{r})$  for electrons ( $j = e$ ) and ions ( $j = i$ ), each one governed by a kinetic Vlasov-Boltzmann like equation with source/sink contributions. The charged process involved in the dust contributes to the fluid equations for each species, with several terms proportional to both, the charging currents  $I_j$  and the dust density  $n_d$ . This contribution should be correctly modeled before carrying out a stability analysis. For the charging process we consider Maxwellian ions and non-Maxwellian electron distribution  $f_e$  which would satisfy the unperturbed steady state Vlasov equation. Hence, we would have  $f_e(v) = f_{e0}(\sqrt{|v^2 - 2e\phi/m_e|})$  if a plasma potential perturbation  $\phi$  is considered. As a simple application, we have used the well-known kappa-distribution function [27, 64, 72]

$$f_{e0} = n_{e0} N_\kappa [1 + (m_e v^2 / T_{e0}) \cdot (2\kappa - 3)]^{-\kappa-1}, \quad N_\kappa \equiv \frac{\Gamma(\kappa + 1)}{\kappa^{3/2} (\kappa - 1/2)}, \quad (2.95)$$

where  $\kappa > 3/2$ . This function becomes to the Maxwellian distribution for  $\kappa \rightarrow \infty$ . Using kappa distribution function we find electron density and temperature

$$n_e = n_{e0} \xi_\phi^{1/2-\kappa}, \quad T_e = T_{e0} \xi_\phi, \quad \text{with} \quad \xi_\phi = 1 - 2e\phi/T_{e0}(2\kappa - 3). \quad (2.96)$$

Notice that  $n_e = n_{e0} \exp(e\phi/T_e)$  and  $T_e = T_{e0}$  are recovered for large  $\kappa$ . The dust charge currents  $I_j$  is determined with the OML current collection model, which shows the dependence on dust charge fluctuation and dust density on both electron and ion fluid equations. Using the unperturbed function  $f_{j0}$  of species  $j$ , the current given by the OML effective charging cross section  $\sigma_c$  for grains of radius  $a$ , is then

$$I_j = q_j \pi a_d^2 \int_{v_{mj}\epsilon_j}^{\infty} v \left(1 - 2 \frac{q_j \varphi_d}{m_j v^2}\right) f_{j0} 4\pi v^2 dv, \quad (2.97)$$

where  $\varphi_d \approx q_d/a_d$  is the potential at the surface of the spherical grain,  $\epsilon_j = (\text{sign}(q_j \varphi_d) + 1)/2$  and  $v_{mj}^2 = 2|\varphi_d q_j|/m_j$ . Considering the charge conservation equation for an isolated plasma

$$\frac{\partial}{\partial t} (en_i - en_e + q_d n_d) + \nabla \cdot (en_i \mathbf{u}_i - en_e \mathbf{u}_e + q_d n_d \mathbf{u}_d) = 0, \quad (2.98)$$



for a fluctuating dust charge  $q_d = -eZ$ , ( $\epsilon_e = 1, \epsilon_i = 0$ ) the dust charging equation is

$$\partial q_d / \partial t + \mathbf{u}_d \cdot \nabla q_d = I_e + I_i = [-en_e V_{T_e} \zeta_e(T_e, Z) + en_i V_{T_i} \zeta_i(T_i, Z)] \pi a^2, \quad (2.99)$$

where the dimensionless functions

$$\zeta_j(T_j, Z) = \int_{\epsilon_j w_{mj}}^{\infty} w \left(1 - \frac{w_{mj}^2}{w^2}\right) \hat{f}_j(w) 4\pi dw, \quad (2.100)$$

have been defined in terms of the dimensionless distribution  $\hat{f}_j(w) = V_{T_j}^3 f_{j0}(V_{T_j} w) / n_{j0}$  with  $w_j = v_{mj} / V_{T_j}$  for species  $j$  with thermal velocity  $V_{T_j} = \sqrt{T_j / m_j}$ . From these expressions, and because the dependence on  $I_i n_d$  ( $I_e n_d$ ) on the fluid equations sink terms, it is convenient to define a characteristic frequency  $\omega_i$ . With the characteristic frequency  $\omega_i = \partial I_i / \partial n_i = I_i / n_i = \omega_i e / n_d$ , the term  $\partial I_e / \partial n_e$  can be expressed as  $-e \omega_i n_{i0} / (n e_{e0} n_{d0})$ . Additionally, with the charging frequencies  $\nu_{qj} \partial I_j / \partial q_j$  for both electrons and ions, the effects of the charging currents and dust charge fluctuations in the perturbed equations can be included by means of these three frequencies as  $\delta I = I_{i0} (\delta n_i / n_i - \delta n_e / n_e) - (\nu_{qe} + \nu_{qi}) \delta q_d$ .

### 2.4.3 Fluid model for electrons and ions

In this section we establish the fluid model for the stability analysis of a partially ionized complex plasma considering the dust charging process. For positive charged ions the ion continuity equation is

$$\frac{\partial}{\partial t} n_i + \nabla \cdot (n_i \mathbf{u}_i) = -\frac{I_i}{e} \frac{n_d}{n_e} + \nu_I n_e - \nu_l n_i, \quad (2.101)$$

where the source of ions for ionization is considered proportional to the electron density  $n_e$ , although the frequency  $\nu_I$  can be also a function of  $n_e$  [22]. The sink term with frequency  $\nu_l$  accounts itself with the ion losses due to several mechanisms, such as recombination. The remaining sink comes from the dust charging and it explicitly depends on both dust and ion densities, the latter is included on  $I_i$ . The time evolution equation for the ion momentum density  $n_i \mathbf{u}_i$ , taking into account the frequencies  $\nu_{ij}$  for collisions between species  $i$  and  $j$  and the previous discussion on kinetic descriptions, reads

$$\frac{\partial n_i \mathbf{u}_i}{\partial t} + \nabla \cdot (n_i \mathbf{u}_i \mathbf{u}_i) = -e \nabla \phi / m_i - I_i n_d \mathbf{u}_d / e - n_i \sum_j \nu_{ij} (\mathbf{u}_i - \mathbf{u}_j), \quad (2.102)$$

where  $j$  is referred to electrons, dust grains and neutrals. The prevailing collision frequency  $\nu_i = \nu_{ia}$  is considered here due to the interaction of ions with cold neutrals at rest.

Although similar equations hold for the electrons, the electron population do satisfy the relations  $n_e(\phi)$  and for  $T_e(\phi)$  directly derived from the non-Maxwellian distribution in Eq. (2.96) that should replace the usual Maxwellian representation. The electron density  $n_e$  can be approximated by a linear function of the perturbation plasma potential  $\delta\phi$  as

$$n_e = \int f_e d\mathbf{v} \approx \int (f_{e0} - \frac{e \delta\phi}{m_e} \frac{1}{v} \frac{\partial}{\partial v} f_{e0}) 4\pi v^2 dv \quad \text{giving} \quad \delta n_e \approx -n_{e0} \frac{e\delta\phi}{m_e} 4\pi \int f_{e0} dv, \quad (2.103)$$

where  $f_{e0}$  is assumed to be isotropic, giving

$$n_e - n_{e0} = \delta n_e \approx -n_{e0} \frac{e\delta\phi}{m_e} 4\pi \int f_{e0} dv. \quad (2.104)$$

For the kappa distribution, these relations can be obtained by Taylor expansion of (2.96) up to first order in  $\phi = \delta\phi$ , giving  $n_e - n_{e0} = \delta n_e = n_{e0} e\delta\phi (2\kappa - 1)/(2\kappa - 3)T_{e0}$  which, if compared with the usual Maxwellian relation  $n_{e0} e\delta\phi/T_e$ , we find that an effective electron temperature can be defined as  $T'_e = (2\kappa - 3)T_{e0}/(2\kappa - 1) < T_{e0}$ . For vanishing ion-electron and dust-electron collision terms and neglecting also the electron inertia, the electron equations can be decoupled from the others, entering into the analysis through  $\delta n_e$ . Since several collective effects involve grains oscillations, it is worthy to consider dust and momentum density fluctuation in the linear stability analysis. With the same reasoning leading to (2.99), an equivalent relation holds for the dust mass  $m_d$  variation as

$$\partial m_d / \partial t + \mathbf{u}_d \cdot \nabla m_d = (m_e |I_e| + m_i I_i) / e, \quad (2.105)$$

meaning that the grain mass still increases although the charging equilibrium  $I_e + I_i = 0$  is reached. The momentum equation for grains is

$$m_d d(n_d \mathbf{u}_d) / dt = -q_d n_d \nabla \phi - m_d \nu_d \mathbf{u}_d, \quad (2.106)$$

where the collision frequencies between grains and the other lighter species have been dropped. For simplicity, we assume here the grains to satisfy a continuity equation with

no source-sink terms. The linearized equations for finite mass oscillating grains, with constant charge sign, are then

$$\frac{\delta n_d}{\partial t} + n_{d0} \nabla \cdot \delta \mathbf{u}_d = 0, \quad \text{and} \quad m_{d0} n_{d0} \frac{\partial \delta \mathbf{u}_d}{\partial t} + q_{d0} n_{d0} \nabla \delta \phi = 0. \quad (2.107)$$

The set of equations is closed by Poisson's equation for the plasma potential

$$\nabla^2 \phi = 4\pi e(n_e + Zn_d - n_i). \quad (2.108)$$

Finally, dropping the zero subscript for noting equilibrium values, with dimensionless parameters  $\delta$  and  $\tau$  derived from  $n_i = (1 + \delta)n_e$ ,  $T_i = \tau T_e$  and the grain mass-to-charge ratio  $\gamma_d = m_d/Zm_i$  and plasma ion and dust frequencies related by  $\gamma_d \omega_{pd}^2 = \omega_{pi}^2 \delta / (1 + \delta)$ , and linearizing equations we have the following matrix

$$\begin{pmatrix} -i\omega + \nu_l + \omega_i & ikn_e(1 + \delta) & \nu_{qi} n_e \frac{\delta}{Z} & -n_e \left[ \nu_I \tau + \frac{k^2}{\omega^2} \frac{1 + \delta}{\gamma_d} V_{Ti}^2 \omega_i \right] \\ ik \frac{V_{Ti}^2}{n_e(1 + \delta)} & \nu_i - i\omega & 0 & ikV_{Ti}^2 \left[ 1 + i \frac{\omega_i}{\omega} \frac{1}{\gamma_d} \right] \\ \frac{\omega_i}{n_e} \frac{Z}{\delta} & 0 & -i\omega + \nu_{qe} + \nu_{qi} & -\omega_i \tau (1 + \delta) \frac{Z}{\delta} \\ -1 & 0 & n_e \frac{\delta}{Z} & n_e \left[ \tau + k^2 \frac{V_{Ti}^2}{\omega_{pi}^2} (1 + \delta) \left( 1 - \frac{\omega_{pd}^2}{\omega^2} \right) \right] \end{pmatrix} \begin{pmatrix} \tilde{n}_i \\ \tilde{u}_i \\ \tilde{Z} \\ \tilde{\phi} \frac{e}{T_i} \end{pmatrix} = 0, \quad (2.109)$$

from which the wave dispersion relation can be extracted, after linearizing and Fourier transforming by the phasor  $e^{-i\omega t + kx}$ .

#### 2.4.4 Discussion

Carrying out the determinant in Eq. (2.109) we obtain a polynomial dispersion relation, which can be solved for a range of wavelengths. Figure 2.17 shows the stability branches for large  $m_d$ . In agreement with previous works [32] for infinitely massive grains ( $1/\gamma_d = 0$ ) an instability emerges in one of the three modes because of the non zero ionization which has to satisfy  $\nu_I = (1 + \delta)(\nu_l + \omega_i)$  because of the initial equilibrium condition. For  $\nu_i > \nu_{qe} + \nu_{qi} + \omega_i$  the unstable-stable mode disappears and new stable-stable one emerges as shown in Figure 2.18. Two new branches appears for  $m_d$  finite and  $\gamma_d < \infty$ , giving a bifurcation at the origin ( $\text{Im}(\omega) = 0$ ,  $k = 0$ ), which is illustrated in Figure 2.19.

Figures 2.19 and 2.20 show a remarkable behavior which does not allow to cross the  $\omega = 0$  axis with continuity, as in the case of Figure 2.17. The unstable mode length for

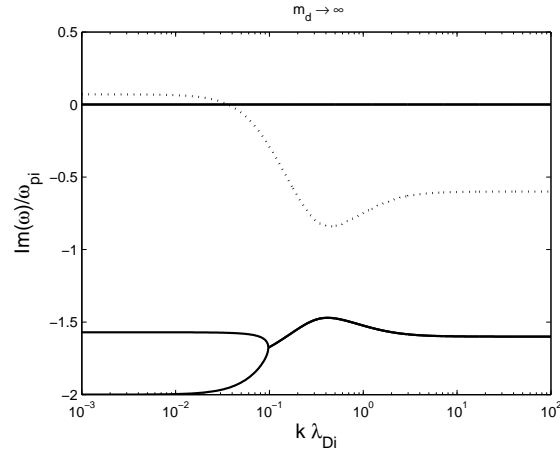


Figure 2.17: Stability diagram for large mass. An instability appears without any bifurcation.

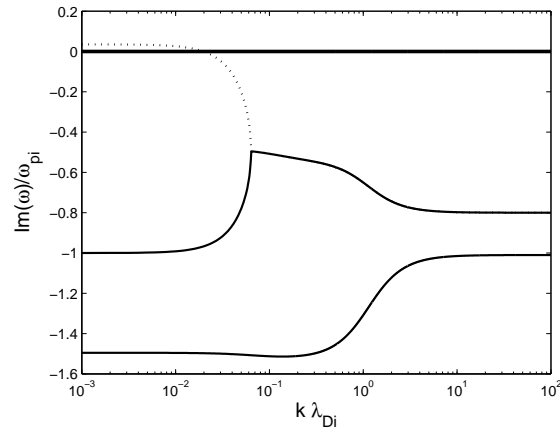


Figure 2.18: Stability diagram for large mass. An instability appears with a new stable-stable mode for  $\nu_i > \nu_{qe} + \nu_{qi} + \omega_i$ .

low  $k$  is controlled by both  $\nu_l$  and  $\nu_{qe}$  with no significant change for different electron distributions. For large  $k$  there are always two (or three) stable modes corresponding to the asymptotic values  $\nu_i$  and  $\nu_{qe} + \nu_{qi}$  for  $\text{Im}(\omega)$ . There is always an instability due to charging that would only disappear for vanishing values of  $\omega_i$  and  $\nu_l$ .

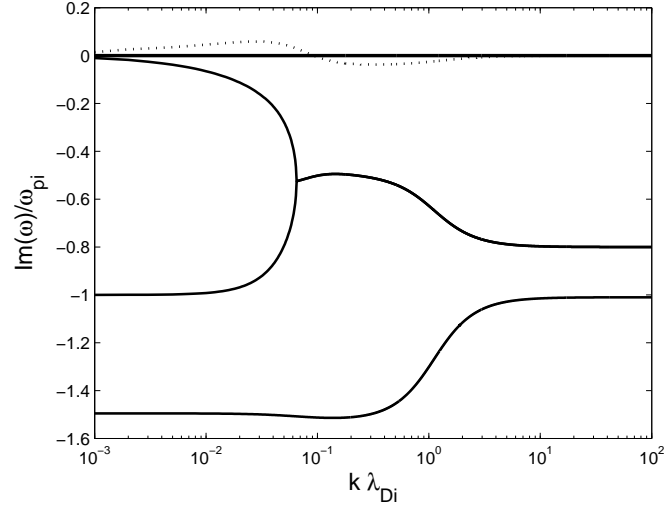


Figure 2.19: Stability diagram for finite grain mass. An instability appears with a bifurcation for the upper branch. Figure 2.20 shows a focus of this bifurcation for several values of  $\nu_l$ .

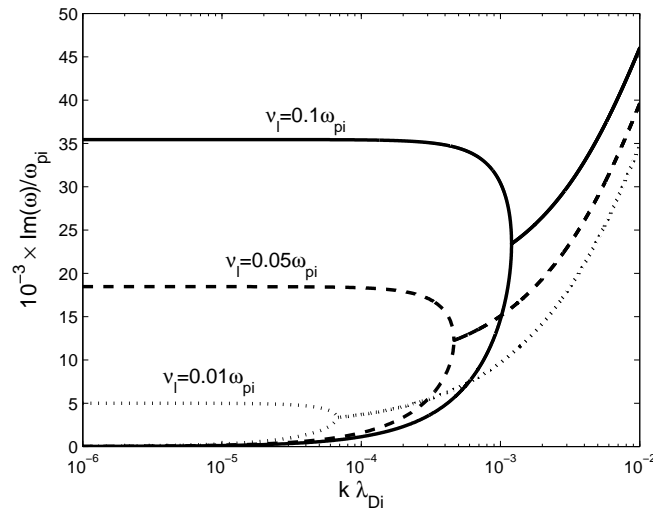


Figure 2.20: Instability variation for finite grain mass and several  $\nu_l$  values.



## CHAPTER 3

# DE-ORBITING SATELLITES AT END OF MISSION WITH ELECTRODYNAMIC TETHERS

### 3.1 Introduction

The work presented in chapters 1 and 2 relate to assessment of mission risk in Jupiter as a result of ejecta from meteoroid impacts on the moons and from collisions between ring particles. The present chapter analyzes the tether design problem for de-orbiting satellites at end of mission [108]. Chapter 1 showed that both ESA/NASA Interplanetary Meteoroid models should be used to know the meteoroid population for near-Earth space. The first model for micro-meteoroid flux was developed by Grün et al. (1985) [39]. NASA's Meteoroid Engineering Model (MEM, 2007) is applicable to missions from 0.2 to 2.0 AU near the ecliptic plane, providing meteoroid fluxes and speeds in the mass range from  $10^{-6}$  to 10 g [63]. MEM is based on the the sporadic meteor observations of the Canadian Meteor Orbit Radar CMOR. The range of applicability of ESA's Interplanetary Meteoroid Environment Model (IMEM, 2005, 2011) is from 0.1 to 5.0 AU and with non latitude restrictions [26]. IMEM provides meteoroid fluxes, densities and speeds for a range of masses of  $10^{-18}$ -1 g. Both IMEM densities and fluxes are determined by the COBE DIRBE thermal radiation measurements and in-situ observations by the Galileo and Ulysses dust instruments. These instruments showed the

meteoroid population for the Jovian system. Both modern ESA/NASA models are based on approximations and simplifying assumptions, and predict potential impact risk against the spacecraft for a specific mission.

Space debris remains a constant menace to the operative satellites in the Earth. High risk to produce the well-known Kessler cascade increases with time [53]. Future satellites should incorporate a de-orbit system just used at end of mission. Electrodynamic tethers might remove both future and current not-active satellites [4, 35, 36, 76, 77, 116]. To remove present inoperative satellites some hook-type technique to capture the debris is also necessary. In the tether experiment SEDS-2 a 19.7 km long, round tether was cut about 4 days after deployment at 350 km altitude, whereas the remaining 7.2 km survived 54 days of its observable orbital life [16]. Unlike SEDS-2, a 4 km long tether survived about 10 years in TiPS mission. This period is about one order of magnitude larger than the characteristic time needed by an electrodynamic tether to complete a full de-orbiting mission, which is typically few months.

At the ambient plasma there is a motional electric field  $E_m = v_{orb} \wedge B$  in the orbiting-tether frame, which reaches values of order 100 V/km and drives a current that results in Lorentz drag. The large electromotive force  $E_m L$ , which involves the component  $E_m$  along a tether of length  $L$ , produces orbital drop from its initial altitude. Cathodic exchange uses a plasma contactor that creates a low impedance pathway for electron current to flow from tether to ambient plasma.

A tether system requires very small probability  $N_c$  of tethers cuts by small debris and very small tether-to-satellite mass ratio  $m_t/M_s$ . These opposing requirements correspond to short and long de-orbit operations, respectively. Tether design involves deriving an equation for the product  $N_c \times m_t/M_s$  for any given initial orbit. A simple circular orbit model with the Lorentz force as the unique orbital perturbation is here considered. Secondly, a complex orbital model including both aerodynamic and Earth's non-sphericity perturbation is also studied. Earth's non-spherical mass distribution produces a secular variation in both argument of perigee  $\omega$  and longitude of the ascending node  $\Omega$ . Using approximations for the first order of the zonal harmonic



coefficient  $J_2$ , both variations are

$$\dot{\omega} = \frac{3}{4}\sqrt{\mu_e}J_2R_e^2\frac{4-5\sin^2 i}{(1-e^2)^2}(R_e+H)^{-7/2} \quad (3.1)$$

$$\dot{\Omega} = -\frac{3}{2}\sqrt{\mu_e}J_2R_e^2\frac{\cos i}{(1-e^2)^2}(R_e+H)^{-7/2} \quad (3.2)$$

where  $R_e$  and  $\mu_e$  are Earth's radius and standard gravitational constant, respectively. For a critical angle  $i_c = \sin^{-1}(2/\sqrt{5}) \approx 63.4$  deg the rate of the argument of perigee vanishes in Eq. (3.1). For  $i < i_c$  the rotation of apsidal line is in direction of the orbit, whereas for  $i > i_c$  the rotation is opposite. For prograde and retrograde orbits, the longitude of ascending node rate  $\dot{\Omega}$ , is negative and positive, respectively. For sun-synchronous orbits the rate is  $\dot{\Omega} = 360$  deg/year. Most of all satellites following sun-synchronous orbits are slightly retrograde. In particular, Envisat, an inoperative Earth-observing satellite follows a near-circular, sun-synchronous orbit at  $H \approx 768$  km. From Eq. (3.2) the inclination for Envisat is about 98.5 deg. De-orbiting Envisat with a passive tape-tether might be considered.

Cryosat, an operative Earth-observing satellite of about 10 m<sup>2</sup>, was launched in April 2010 to measure arctic sea-ice thickness. Unlike the weighty Envisat satellite, which is about 8100 kg, the lighter Cryosat satellite of about 720 kg follows a non-synchronous orbit at 720 km altitude with inclination of 92 degrees. The end of mission for Cryosat is scheduled on October 2015. Preliminary results of tape-tether design for de-orbiting Cryosat and Envisat are here presented.

### 3.2 Survival against debris

Long thin geometry of tethers make them prone to fatal impacts by abundants small debris. Following the results found by Khan and Sanmartin [52] thin-tape tethers have much greater survival probability than round tethers of equal length/mass. High survival probability requires low fatal-impact count  $N_c$  in Poisson's distribution

$$P = e^{-N_c} \approx 1 - N_c, \quad (3.3)$$

where  $N_c$  may be given by simple approximation to fatal count-rate  $\dot{n}_c = N_c/L\Delta t_d$ . Two models may be used to determine the cumulative-flux  $F(\delta)$  for the debris size  $\delta$ .

Models from NASA (ORDEM) and ESA (MASTER) presents particular type of flux for each debris size. For a round tether, the fatal impact rate reads

$$\frac{dN_c}{dt} = - \int_{\delta_m(D)}^{\delta_{max}} \frac{dF}{d\delta} d\delta \times L D_{eff}(D, \delta), \quad (3.4)$$

where  $\delta_{max}$  is the largest size of interest, say 1 m, and  $\delta_m(D)$  is the minimum size that may sever tether. Energy considerations suggest  $\delta_m \sim D/3$ . The effective diameter,  $D_{eff} = D + \delta - \delta_c$ , with  $\delta_c \sim \delta_m$ , takes into account that debris have macroscopic size and that severing requires some overlap of tether and debris volumes.

For tapes, the fatal impact rate involves an additional integral over impact angle between debris velocity and tape normal. Using NASA's ORDEM for a conservative approach and tape-tether of length  $L$ , width  $w$  and thickness  $h$ , Khan and Sanmartin [52], making simple approximations for  $w \lesssim 6$  cm, found

$$\frac{dN_c}{dt} \simeq A(n_1) L w^{-n_1/2} h^{1-n_1/2} \delta_*^{n_1} F_*, \quad (3.5)$$

$$A = \frac{8}{\pi^2} \left( 3\sqrt{\frac{\pi}{4}} \right)^{n_1} \frac{3n_1 + 2}{6(n_1 - 2)}, \quad (3.6)$$

where  $n_1$  is a slope in the flux versus debris size curve found from Figure 3 in reference [52]. Both  $F_*$  and  $\delta_*$  are the intersection of two power laws in  $\delta$  ranges from Figure 3 in reference. [52]. In all cases debris diameter  $\delta_*$  is close to 2 cm which is about the maximum tape width for OML collection. In general, the altitude-dependent  $n_1(H)$  takes values larger than 3. A value  $N_c = 0.05$ , say, means that 5 among 100 tethers would be cut while de-orbiting. For MASTER, the debris flux rate would roughly be smaller by one order of magnitude.

### 3.3 Current model in tape-tethers

A tether, stripped of insulation, collects electron in OML regime. The tether collects electrons (ions) over a segment polarized positive (negative),

$$\Delta V \equiv \phi_t - \phi_{pl} > 0 (< 0). \quad (3.7)$$

In the simple case of weak ohmic effects tether potential is uniform, whereas  $\phi_{pl}$  in the ambient plasma varies linearly. Both  $\Delta V$  and current  $I$  do vary too. Current is

negligible when  $E_m$  points to the hollow cathode (HC), where electrons are emitted (see Figure 3.1). At high inclinations, the motional field  $E_m$  changes sign as the Earth rotates under the orbital plane; only for the daily fraction where it has the right direction does the tether work (sensible current). Most of the time  $E_m$  is positive (negative) for prograde (retrograde) orbits. Figure 3.1 shows a schematic of tether operation with the motional field reversing direction during near polar orbits.

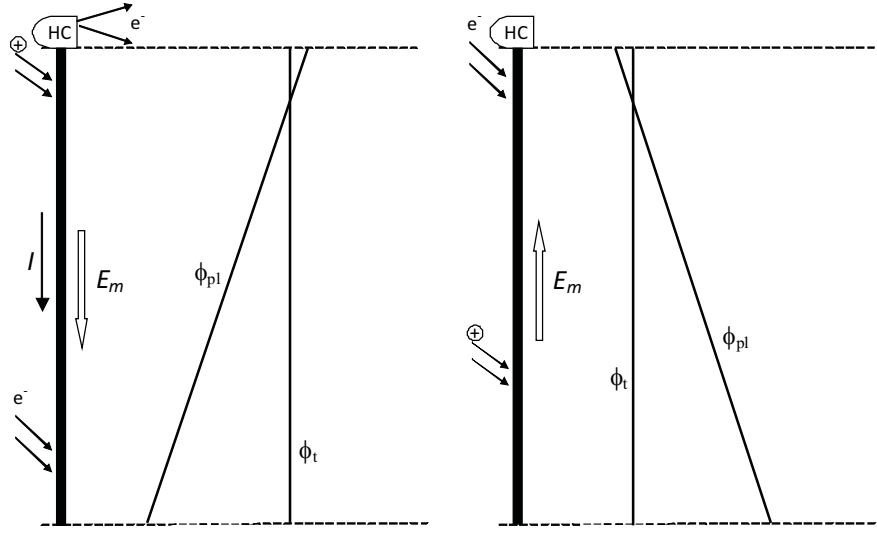


Figure 3.1: Schematic of tether operation with the motional field reversing direction during near polar orbits. For prograde and retrograde orbit, the hollow-cathode should be correctly posed downward and upward, respectively.

For negligible ohmic effects and no sensible power load, bias  $\Delta V$  varies linearly from a maximum  $E_m L$  at the anodic end to near zero at an efficient hollow cathode at the opposite end. For simplicity, the tether is assumed perfectly aligned with the local vertical along the orbit. The length-averaged current,  $I_{av}$ , is  $2/5$  of the value if bias was uniform at maximum

$$I_{av} \approx \frac{2}{5} \times e N_e L \frac{2w}{\pi} \sqrt{\frac{2e E_m L}{m_e}}, \quad (3.8)$$

where  $N_e$  is the ionospheric electron density. Ohmic effects do limit the current to the short-circuit value,  $I_{sc} = \sigma_c h w E_m$ . The normalized length-averaged current [93]

$$\frac{I_{av}}{I_{sc}} \equiv i_{av}(\xi), \quad (3.9)$$

that gauges ohmic effects, being a definite function of a ratio involving tether and

ambient parameters,

$$\xi \equiv \frac{L}{h^{2/3}l^{1/3}}, \quad l \approx 2.38 \cdot 10^{18} \times \frac{E_m / (150\text{V/km})}{(N_e / 10^5\text{cm}^{-3})^2}. \quad (3.10)$$

For  $0 < \xi < 4$ , the  $i_{av}(\xi)$  is implicitly given by the equation

$$i_{av} = 1 - \left[ \int_0^1 \frac{d\varphi}{\sqrt{1 + (1 - i_{av})^{3/2} \xi^{3/2} (\varphi^{3/2} - 1)}} \right]^{-1}. \quad (3.11)$$

which approaches  $i_{av} = 0.3\xi^{3/2}$  for  $\xi$  vanishing (no ohmic-effects), Eq. (3.8) being roughly accurate up to  $\xi = 1$ , while it is accurately given as  $i_{av} = 1 - 1/\xi$  for  $2 < \xi < 4$ . This last expression is exact for  $\xi > 4$ . Figure 3.2 shows  $i_{av}(\xi)$  from the numerical solution of Eq. (3.11) and from the above approximations [104].

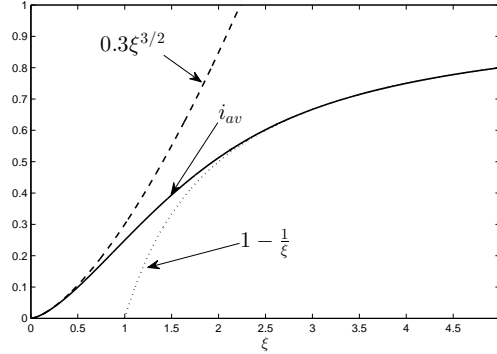


Figure 3.2: Exact and approximate solutions for the dimensionless average current  $i_{av}$ .

### 3.4 Conductive tether design for a generic mission

For given tape dimensions, the orbital evolution under tether drag will involve multiple effects. Among all possible orbit perturbations, larger contribution are given by both Lorentz and aerodynamic forces, and oblateness effects. For a satellite of mass  $M_s$ , the orbital equation is

$$M_s \frac{d\mathbf{v}}{dt} + M_s \frac{\mu_e \mathbf{r}}{r^3} = LI_{av} \mathbf{u}_t \wedge \mathbf{B} + \mathbf{F}_{J_2} + \mathbf{F}_a, \quad (3.12)$$

where  $\mathbf{u}_t = (\cos \omega t, \cos i \sin \omega t, \sin i \sin \omega t)$  for circular orbit, being  $\omega = \sqrt{\mu_e / r^3}$  the orbit angular velocity. A point-like mass is assumed for the orbital evolution around the

Earth. The Lorentz force will be actually dominant against oblate-Earth ( $J_2$ ) effects that slightly modify orbital inclination, and the air-drag force  $\mathbf{F}_a$  that would slightly increase the orbital drop rate at not too low altitudes. Perturbations due to the Earth's non-asphericity produce the following force

$$\mathbf{F}_{J_2} = M_s \nabla \phi_{J_2}, \quad \phi_{J_2} = -\frac{\mu_e J_2}{r} \frac{1}{2} \left( \frac{R_e}{r} \right)^2 (3 \sin^2 \lambda - 1), \quad (3.13)$$

where  $\lambda$  is the geocentric latitude. Finally, the aerodynamic force,

$$\mathbf{F}_a = -\frac{1}{2} \rho_n C_D A |v| \mathbf{v}, \quad (3.14)$$

is generally presented below 300 km. Drag acceleration depends on both atmospheric density  $\rho_n$  of neutral elements and dimensionless drag coefficient  $C_D$ , which is associated with the front area  $A$  of the tether-satellite combination. The values of  $C_D$  is generally in the range of 1.6-2.2. For small values of mass-to-area ratio, aerodynamic drag might manifest at upper altitude.

For tether design we just retain here the Lorentz force, which, for conditions of interest, is itself weak. This results in the orbit slowly evolving through a long, spiraling sequence of quasi-circular orbits. Carrying out the scalar product with  $\mathbf{v}$  in Eq. (3.12) we have

$$-M_s v \frac{dv}{dt} = -\sigma_c E_m^2 w h L i_{av}. \quad (3.15)$$

Equation (3.15) can be rewritten as an equation for orbit-altitude  $H$  evolution by using  $v^2 \approx v_{orb}^2 = GM_e / (R_e + H)$  and introducing tether mass  $m_t = \rho_t w h L$ ,

$$\frac{M_s}{m_t} \left( \frac{dH}{dt} \right) = -2 (R_e + H) \frac{\sigma_c E_m^2}{\rho_t v^2} \times i_{av}(\xi). \quad (3.16)$$

which will hold over the fraction  $f_\tau$  of orbital period having the motional field pointing away from the tether end that holds the hollow cathode. We will take this into account by averaging (3.16) over the orbits given for a day and introducing a factor  $f_\tau$  on the right hand side.

Introducing  $s \equiv L^3/h^2$  and using Eqs. (3.7) and (3.16) to divide  $dN_c/dt$  by  $dH/dt$ , there a results an equation for the rate  $dN_c/dH$ ,

$$\frac{m_t}{M_s} \frac{dN_c}{dH} = -\frac{L}{R_e + H} \frac{\rho_t v^2}{\sigma_c E_m^2} \frac{1}{i_{av}} \times A(n_1) \times w^{-n_1/2} h^{1-n_1/2} \delta_*^{n_1} F_*, \quad (3.17)$$

where  $A$  is given by Eq. (3.6). Finally integrating Eq. (3.17) above from the initial altitude  $H_0$  to a final altitude  $H_f$  an equation for the product of  $N_f$  and  $m_t/M_s$ , which must be minimized [108],

$$\frac{m_t}{M_s} \times N_f = \Pi(w, s [L/h^{2/3}]), \quad (3.18)$$

$$\begin{aligned} \Pi \equiv & \frac{4}{\pi^2} \int_{H_f}^{H_0} \frac{dH (R_e + H_f)}{(R_e + H)^2} \times \frac{\xi(s^{1/3}, H)}{i_{av}[\xi(s^{1/3}, H)]} \times \frac{\rho_t v_f^2}{f_\tau \sigma_c E_m^2[H]} (y) \\ & \times [l^{1/3}[H] \cdot h^{(10-3n_1)/6} \cdot w^{-n_1/2} (m^2)] \cdot A(n_1) \times \delta_*^{n_1} \times F_* (m^{-2} y^{-1}). \end{aligned} \quad (3.19)$$

We consider de-orbiting down to  $H_f = 300$  km, where air-drag on the reasonably large tether surface area  $Lw$  typically results in rapid reentry, while plasma density rapidly decreases below the  $F$  layers. For prograde and retrograde orbit, the tether correctly works when  $E_m$  is positive and negative, respectively. The  $f_\tau$  gives the daily fraction when  $E_m$  is positive or negative. Additionally, electron density  $N_e$  is also averaged for the same daily fraction. De-orbit efficiency depends on altitude/inclination though plasma density  $N_e$  and  $E_m$  component of motional field along the tether. Both  $E_m(H)$  and  $l(E_m, N_e)$  profiles are determined for initial altitude  $H_0$  and given inclination. One may choose  $w$ , and  $s(L, h)$  to make Eq. (3.19) minimum for given ambient profiles. Figure 3.3 shows curves of  $\xi$ ,  $i_{av}$  and  $\xi/i_{av}$  for a range of  $\xi$  values.

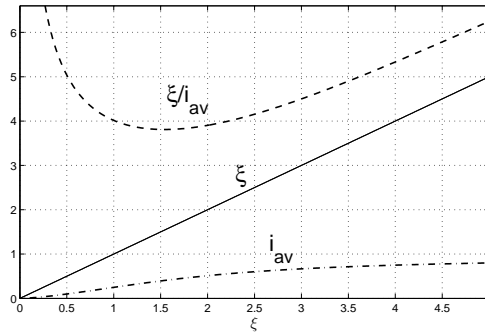


Figure 3.3: Curves of  $\xi$ ,  $i_{av}$  and  $\xi/i_{av}$  are represented for a range of  $\xi$  values.

### 3.5 Results

Several daily-averaged profiles in altitude are needed in designing a tether for de-orbiting: motional field component along the tether  $E_m(H)$ , ambient characteristic length  $l \propto E_m/N_e^2(H)$ , and the family of flux values at debris size  $\delta = w, F(w, H)$ . For any given altitude  $H$  the orbital period is  $T = 2\pi\sqrt{(R_e + H)^3/\mu_e}$ .

The Lorentz force causes a drop from upper altitude to a lower orbit. Daily-averaged profiles of motional electric field, density, and debris flux are determined for each orbital decay for several revolutions of period  $T$ .

As example, we consider the simple model for a Cryosat-like orbit ( $H_0 = 720$  km and  $i = 92$  deg). IGRF and IRI ambient models determine Earth's magnetic field and electron density, respectively. An averaged solar flux of several 11-years cycles is considered for the ambient models. Notice that higher (lower) solar flux would make increase (decrease) electron density. The averaged current  $I_{av} \propto N_e$  would then increase and decrease for high and low solar flux, respectively.

Figure 3.6 shows the electron density map from 200 to 800 km in function of the latitude for maximum, medium and minimum solar flux. Figure 3.7 shows the electron density map from 200 to 800 km in function of the longitude for maximum, medium and minimum solar flux.

For the retrograde Cryosat-like orbit here studied the daily-averaged field  $E_m$  is negative about 53 %, and  $n_1(H)$  varies in the range 3.6-4.1. The daily-averaged profiles of  $E_m$ ,  $l$ ,  $n$ , and  $f_\tau$  are shown in Figure (3.4). With the daily-averaged profiles of  $E_m$ ,  $l$ ,  $n$ , and  $f_\tau$ , the integrand in Eq. (3.19) may be carried out for a range of  $w$  and  $s(L, h)$  values. Numerical results are shown in Figure 3.5. Notice that the daily-averaged field  $E_m$  is negative about 53 %. With  $m_t = \rho_{tc}whL$  and given a satellite mass  $M_s$ , the tether-to-satellite mass ratio for minimum  $L/h^{2/3} = s_m^{1/3}$  is

$$\frac{m_t}{M_s} = \frac{\rho_{tc}wh^{5/3}s_m^{1/3}}{M_s}, \quad (3.20)$$

where  $s_m$  is the value of  $s$  in which Eq. (3.19) reaches the minimum,  $\Pi_m$ . Introducing

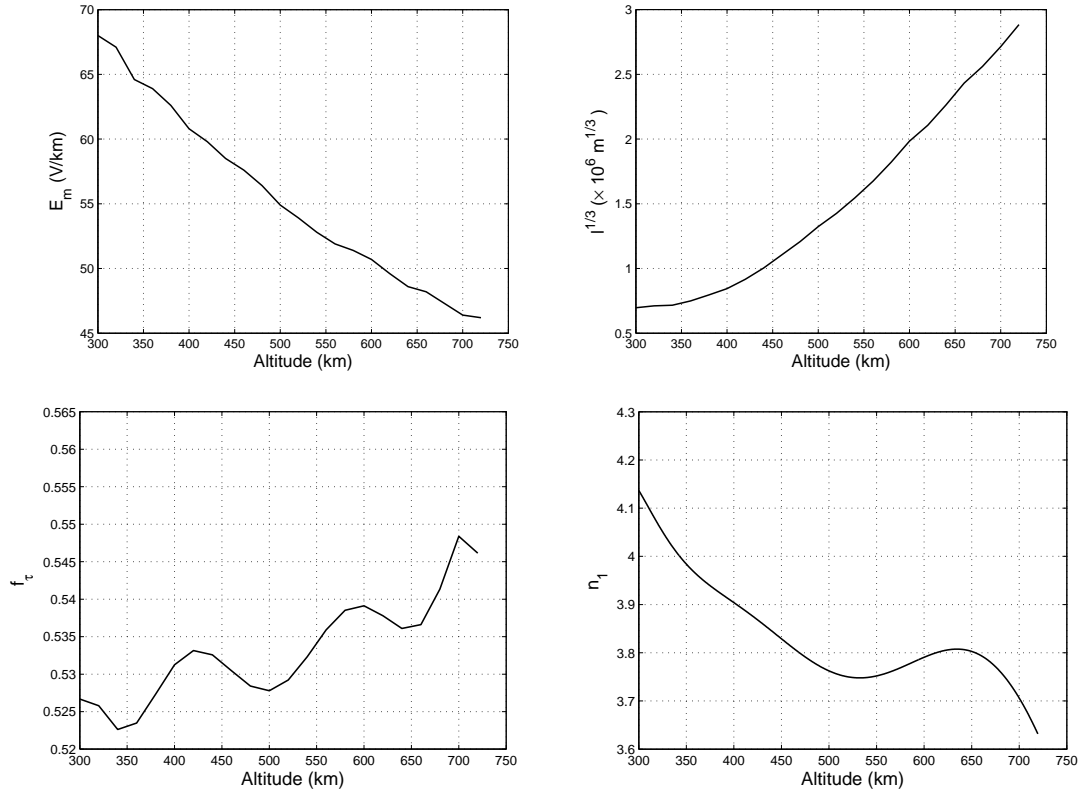


Figure 3.4: Profiles of  $E_m$ ,  $l^{1/3}$ ,  $f_\tau$  and  $n$  for Cryosat ( $H_0 = 720$  km,  $i = 92$  deg). The daily-averaged field  $E_m$  is negative about 53 %, and  $n_1(H)$  varies in the range 3.6-4.1. Note that the ambient profiles are not dependent on satellite mass and tether design.

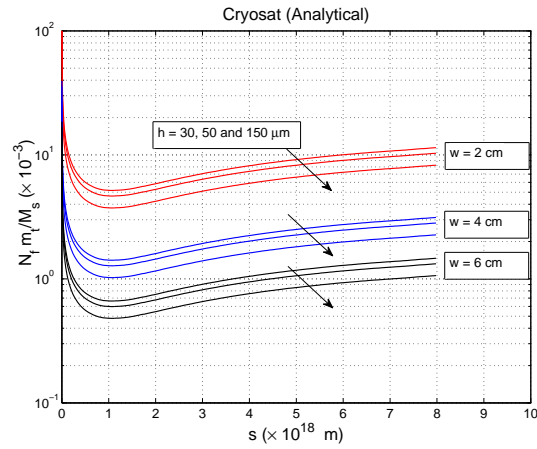


Figure 3.5: Numerical results of  $N_f m_t / M_s = \Pi$  for Cryosat. Minimum  $\Pi$  value is found for  $w = 6$  cm and  $h = 300$   $\mu\text{m}$ .



Eq. (3.20) in Eq. (3.18), the sever probability will be then

$$N_f = \frac{M_s}{\rho_{tc} w h^{5/3} s_m^{1/3}} \times \Pi_m(w, s_m). \quad (3.21)$$

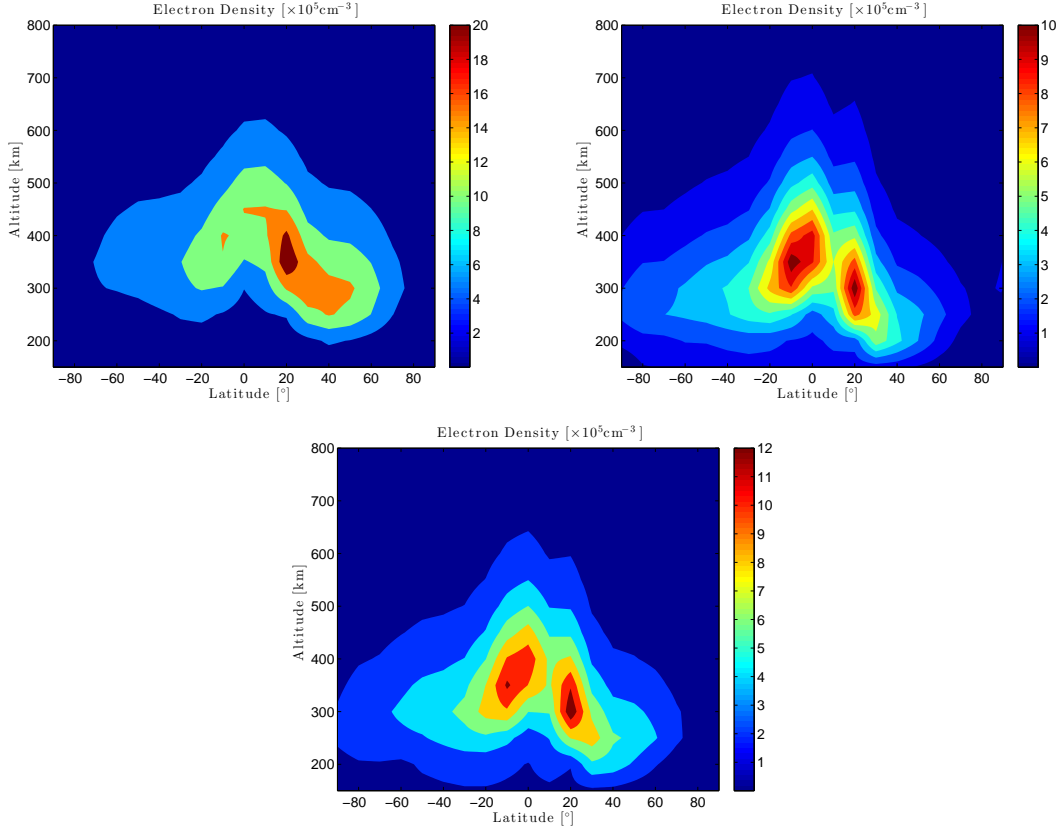


Figure 3.6: Electron density map from 200 to 800 km in function of the latitude. The two upper figures represent the density for maximum and minimum solar flux from left to right, respectively. The last figure illustrates the density for medium solar flux.

For  $M_s = 720$  kg for Cryosat, Figure 3.8 shows both  $m_t/M_s$  and  $N_f$  results for a range of  $h$  values. The probability of cuts and the tether-to-satellite mass ratio decreases and increases, respectively, for  $h$  increasing. One should select  $h$  with the lower values which compromise both  $N_f$  and  $m_t/M_s$ . The compromise of both quantities depends on the requirements in the mission, however. The minimum of both values would occur at the intersection of full and dashed lines as it is shown in Figure 3.8, i.e. where  $N_f = m_t/M_s$ . With  $L = h^{2/3} s_m^{1/3}$ , optimal lengths of the tether are shown in Figure 3.9 for a range of  $N_f$  values.

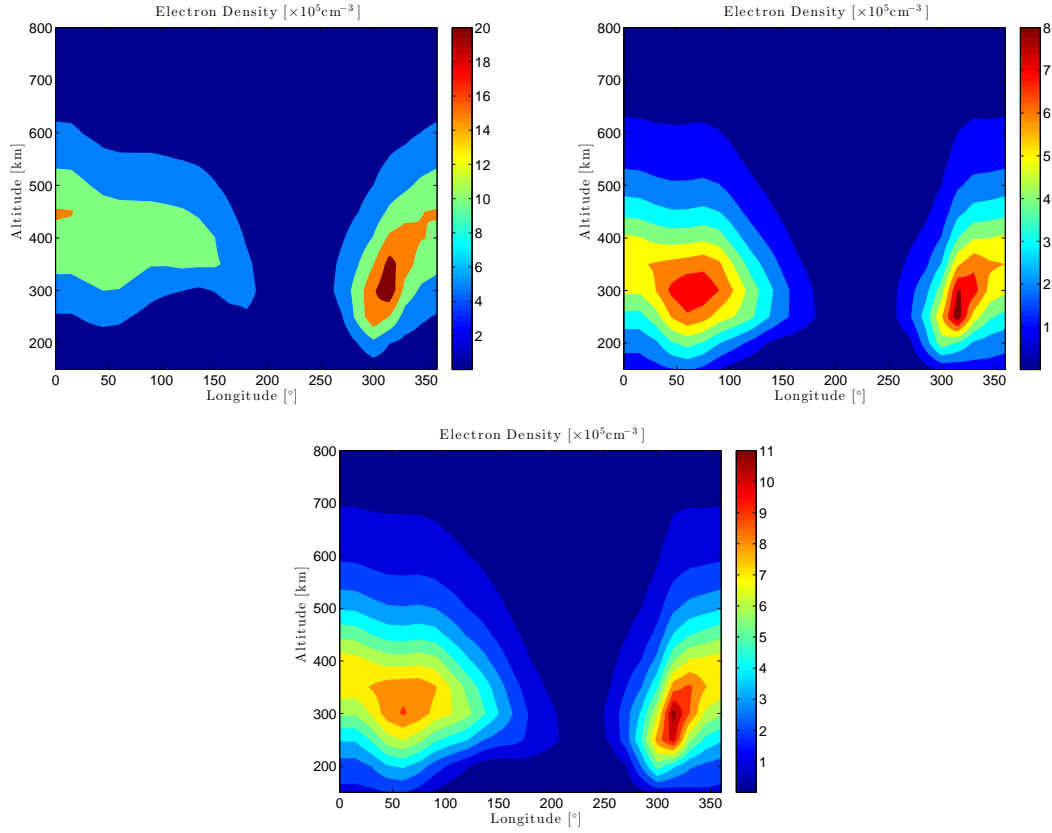


Figure 3.7: Electron density map from 200 to 800 km in function of the longitude. The two upper figures represent the density for maximum and minimum solar flux from left to right, respectively. The last figure illustrates the density for medium solar flux.

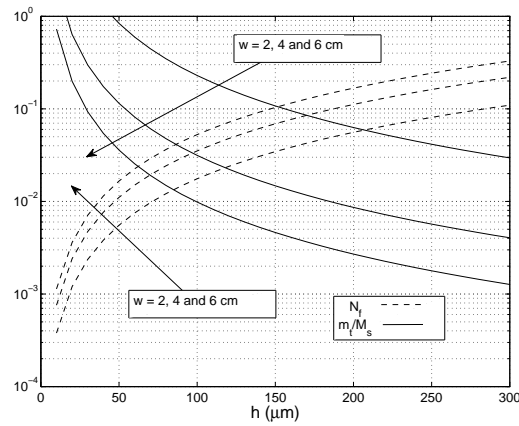


Figure 3.8: Considering Cryosat mass ( $M_s = 720\text{kg}$ ), results of  $m_t/M_s$  and  $N_f$  are found for a range of  $h$  values and three widths.

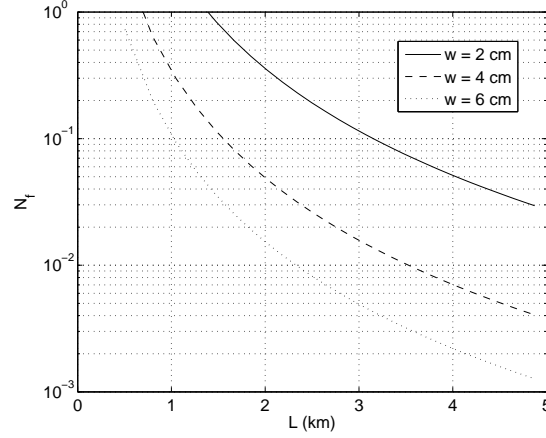


Figure 3.9: Considering a Cryosat-like orbit, optimal values of  $L$  are found for a range of  $N_f$  values and three widths.

Regarding the de-orbit time, notice that carrying out the integral in Eq. (3.16) gives

$$t_f = \int_{H_0}^{H_f} \frac{M_s}{2m_t} \frac{\rho_t v_f^2}{\sigma_c E_m^2(H)} \frac{(R_e + H_f)}{(R_e + H)^2} \frac{dH}{i_{av}(\xi_*)}, \quad (3.22)$$

where  $\xi_* \equiv L/h^{2/3}l_*^{1/3}$ , being  $l_*$  a mean value of  $l(H)$ . For Cryosat a de-orbit time of about 138 days is found for  $w = 6$  cm,  $L = 1.76$  km and  $h = 65 \mu m$ . The sever probability will be  $N_f \approx 0.022$ .

Considering now the full model of Eq. (3.12), total de-orbit time  $t_f$  may be numerically determined. Cowell's method for two-body problem with perturbations is here applied [119]. Second-order differential equation in  $\mathbf{r}$  is then reduced to first-order differential equation system,

$$\frac{d\mathbf{r}}{dt} = \mathbf{v}, \quad (3.23)$$

$$\frac{d\mathbf{v}}{dt} = -\frac{\mu_e}{r^3}\mathbf{r} + \frac{1}{M_s} (LI_{av}\mathbf{u}_t \wedge \mathbf{B} + \mathbf{F}_{J_2} + \mathbf{F}_a). \quad (3.24)$$

To determine numerical solutions, Eqs. (3.23) and (3.24) are integrated with a variable time step Runge-Kutta method [17]. For aerodynamic drag, the density  $\rho_n$  of neutral elements is determined with NRLMSISE-00 atmosphere model. As regards of survival probability, note that integrating Eq. (3.7) gives

$$N_f \approx L \int_0^{t_f} A(n_1) w^{-n_1/2} h^{1-n_1/2} \delta_*^{n_1} F_* dt. \quad (3.25)$$

The de-orbit time found with the full model will be about 130 days for Cryosat and tether dimensions of  $w = 6$  cm,  $L = 1.76$  km and  $h = 65 \mu m$ . Considering Eq. (3.25) the total sever probability is  $N_f \approx 0.016$ . Figure 3.10 shows the changes of altitude,  $N_f$ , inclination and eccentricity along the time.

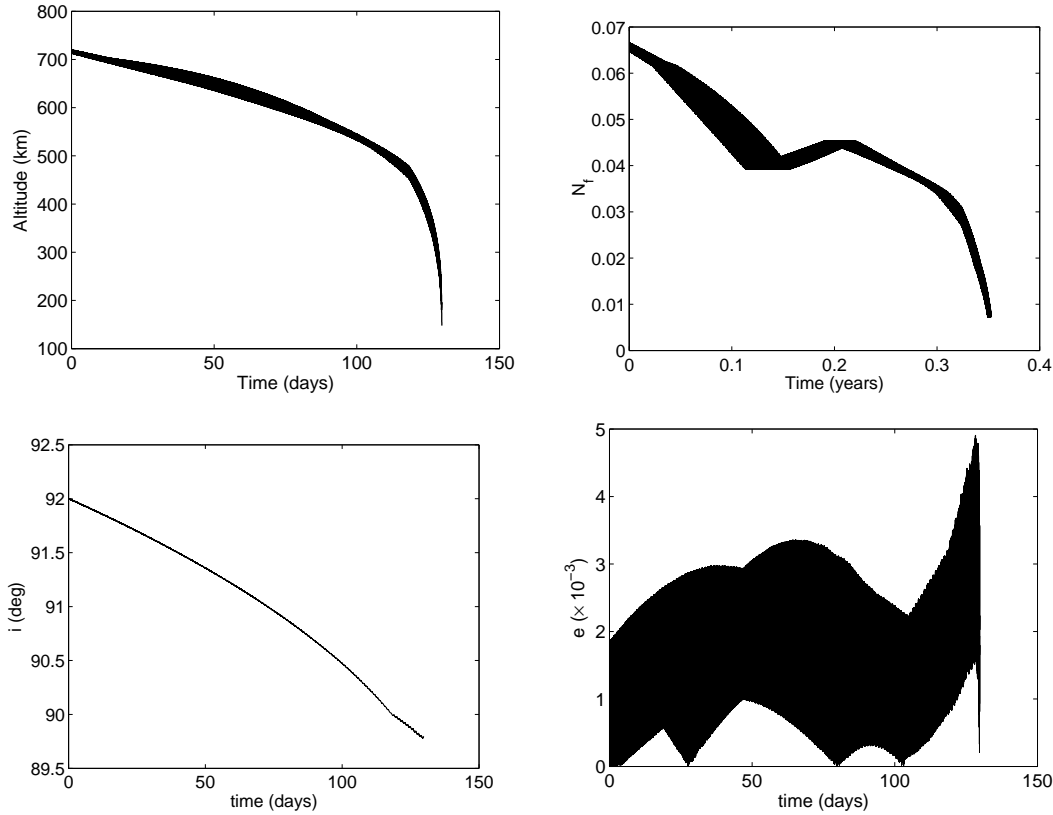


Figure 3.10: Variation in altitude,  $N_f$ , inclination and eccentricity versus time for de-orbiting Cryosat with a tether of  $w = 6$  cm,  $L = 1.76$  km and  $h = 65 \mu m$ .

Optimal values of tether dimensions for Envisat are also determined. Following the same procedure as before we found  $t_f \approx 166$  days and  $N_f = m_t/M_s \approx 0.020$  for a tether of  $w = 6$  cm,  $L \approx 4$  km,  $h \approx 260 \mu m$ . In the next section 3.6 we consider de-orbiting Envisat with a rocket strategy.

### 3.6 De-orbiting large satellites with rockets

For very large and weight satellites, like Envisat, a controlled strategy with rocket might be also considered. With one-impulse Hohmann, the initial cuasi-circular orbit becomes

to an elliptical orbit. Since the aerodynamic force will be reasonably large under 300 km, a large satellite passing near the perigee  $r_p$  does reduce the apogee  $r_a$  for each orbit. As example, for Envisat we may consider a slightly elliptical orbit of  $r_p = 200 + R_e$  km and  $r_a = 780 + R_e$  km, with a eccentricity of  $e = (r_a - r_p) / (r_a + r_p) \approx 0.044$  and 98.5 deg inclination. Assuming  $c_D \approx 2.2$ , an effective area of about 70 m<sup>2</sup> and  $M_s = 8100$  kg, the deorbit will be very rapid. This type of method would provide a controlled re-entry orbit with a low perigee with a final impulse below an altitude of about 120 km. The modified equinoctial equations for orbital determination is now considered (see Appendix B). This generic method avoids several singularities for the planetary Lagrange equations. Considering mid-cycle solar flux in the NRLMSISE-00 atmospheric model, the de-orbit time and both inclination and eccentricity variation are shown in figure 3.11.

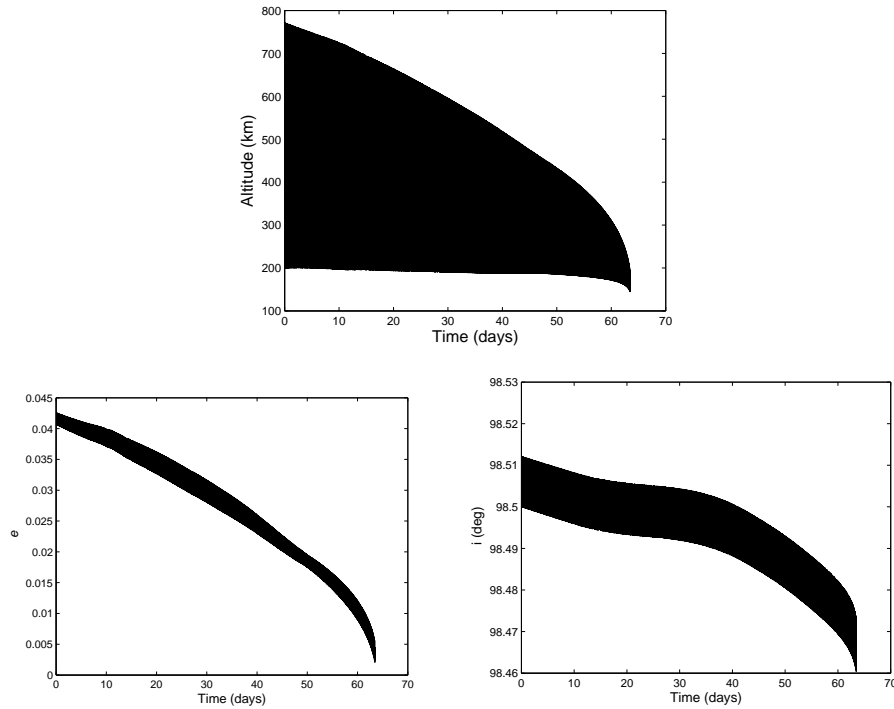


Figure 3.11: Upper figure represents the altitude variation versus time for Envisat-like satellite following an elliptical orbit. Below are represented both inclination and eccentricity variation versus time.

### 3.7 Discussion

Preliminary results of tape-tether lengths have been determined with an optimization of the simple model of Eq. (3.18). The values of the three tape-tether lengths are found with the minimum in Eq. (3.19) for Cryosat; with the minimum values of  $\Pi_m$ ,  $w_m$  and  $s_m$ , Eq. (3.21) gives the probability of cuts for a range of  $L$  (or  $h$ ) values. Results in Figure 3.5 for de-orbiting Cryosat suggest larger widths to minimize the  $N_f \times m_t/M_s$  product. The range of the width is delimited to collect in OML regime ( $w < 6$  cm), however. Lengths and thickness selection is completely connected to both  $N_f$  and  $m_t/M_s$  values. The compromise of both  $N_f$  and  $m_t/M_s$  values will depend of the type of mission; for missions where give more importance to the probability of cuts,  $L$  (or  $h$ ) should be selected to make  $N_f$  minimum with also  $m_t/M_s$  moderately low; just the opposite should occur when the mission specially takes care of the tether-to-satellite mass ratio. The results focus in the case of  $N_f = m_t/M_s$  for Cryosat.

Regarding the full model of Eq. (3.12), numerical solutions for Cryosat of  $t_f$  and  $N_f$  give similar results to the simple model of Eq. (3.15).

Recalling that MASTER model would yield rates  $dN_c/dt$  one order of magnitude smaller, and using  $N_c \sim m_t/M_s$ , MASTER would yield a mass fraction about 3 times smaller.

For very large  $M_s$  and near polar orbits, tethers might not be highly efficient. As it is shown in section 3.6, tethers might not be enough competitive against rocket for these extreme conditions; mainly, because of their uncontrolled behavior at the reentry for a very large structure.

This thesis analyzed: (1) a simple 2D orbital transfer mission from Earth to Jupiter with a set of parallel, cylindrical tethers, (2) several scientific missions to Jupiter with a single electrodynamic tether, and (3) a tape-tether design for de-orbiting satellites in Low Earth Orbit.

Chapter 1 shows the potential use of electric solar sail to reach Jupiter with no gravity assists. A highly negative bias produces ion scattering at some distance from the tethers. A simple approximation of symmetric potential profiles, which are exact for the infinite-cylinder stationary (non-moving) case, is here considered. Considering solar flow parallel to the e-sail motion, the stationary potential profile is determined with the numerical solution of Poisson-Vlasov coupled equations. An approximated model of the potential profile for a solar wind stream flowing against the tether gives the thrust. The force produced is moderately large for larger values of  $\Phi_p$ . The thrust varies with the distance from the Sun with a law of  $\beta$  exponent. Since ion flow condition reduces the reach of the potential, the resulting thrust is also reduced. A non-stationary potential profile for moving tether should be studied to obtain a detailed potential profile. Results of the interplanetary mission show that electric solar sail is particularly effective for high potential bias and small masses. For very large masses a parallel design of e-sail should require a very large number of long tethers. Since the range of the potential produced by a single tether varies along the orbit trajectory consid-

ered in this thesis (Earth-Jupiter orbit transfer), the distance between parallel tethers should be accommodated to evade interference effects. An starfish-like design might be inefficient due to interference effects; i.e. the potential of the tethers will interfere at points closer to the spacecraft. An hybrid strategy with a combination of gravity assists might be considered in a future work for interplanetary missions. This hybrid strategy should allow increasing payload masses. For an interplanetary mission meteoroid population models should be considered to analyze the sever probability in the whole e-sail. Both ESA/NASA Interplanetary Meteoroid models should be considered to know the meteoroid population. NASA's Meteoroid Engineering Model (MEM) is applicable to missions from 0.2 to 2.0 AU near the ecliptic plane, whereas the range of ESA's Interplanetary Meteoroid Environment Model (IMEM) is from 0.1 to 5.0 AU with non latitude restrictions.

Regarding the scientific mission to Jupiter considered in Chapter 2, several applications have been studied. Firstly, the radiation impedance for Juno-like mission and following a circular orbit below Jovian radiation belts (LJO) is determined in section 2.2. Both Alfven and Fast Magnetosonic waves modes of radiation were analyzed. Unlike LEO case, the impedance for Alfven and voltage drop for Fast Magnetosonic waves (FM) were found large. There are three main results obtained here. First, the voltage drop for FM emission in Jupiter is 30-100 times greater than in LEO. Secondly, Alfven impedance in Jupiter is several orders of magnitude greater than in LEO. Finally, impedance of Jovian tethers are reduced by about one half if stripped of insulation. A briefly discussion above the radiation impedance with thermal effects is considered in Appendix A.

Ambient conditions in Jupiter allow natural generation of aurora emission. Jovian radio emissions were detected during the Voyager's flybys in 1979. Jupiter exhibit several emission ovals which are aligned along both north and south magnetic poles and co-rotate with the planet. Jupiter's moon, Io, interacts with the Jovian magnetosphere, resulting Alfven waves which may accelerate energetic electrons. This plasma acceleration process may generate auroral emission in IR, UV, and Radio wavelengths. Short (radio) bursts have been observed from the decametric emissions recorded at the



Kharkov UTR-2 radio-telescope. In NASA's Juno mission the spacecraft will orbit in the polar region to observe in-situ both Jupiter's main auroral oval and the footprint aurora emissions in the Io-Jupiter interaction. Tethers in LJO might generate aurora artificially. The suggested application of an orbiting bare tether for generation of aurora in Jupiter is shown in section 2.3. The electrically floating bare tether will produce secondary electrons. For a range of values below the loss-cone pitch angle will produce atmosphere penetration of these electrons in the Jovian upper atmosphere which produce auroral effects. Since the loss-cone pitch angle  $\alpha_{lc}$  is larger for regions close to Jupiter and the dip-angle  $\phi$  along Jovian longitude is similar for  $r < 1.4 R_J$ , the range of e-beam penetration ( $\alpha_{lc} - \phi$ ) is larger for  $r = 1.05 R_J$  than  $r = 1.40 R_J$ .

In both jovian and Earth ambient, several plasma instabilities could occur. In the Earth's ionosphere several instability mechanisms may explain ionospheric disturbances at low latitude and mid-latitudes. The Rayleigh-Taylor instability describes an instability between two fluids of diverse densities. A slight perturbation at the interface, light and heavy fluid will rise and sink, respectively. These fluids will interchange whereas the system becomes unstable. In the ionosphere the heavy component of the fluid would be the dense plasma in the night-time  $F$  region and the light fluid should be localized under the  $F$  layer, where the plasma density will be lower. The inclusion of charged grains in the plasma should produce another instability mechanism. In section 2.4 the instability mechanism in dusty plasma with charged, light grains is analyzed. Additionally, the non-Maxwellian function distribution for electrons, slightly affect to the instability. A new branch of instability appears for charged, lightweight grains. This study will be extended in a future work to explain the large electron density peak on the M2 layer of Mars's atmosphere; an sporadic upsurge of the meteoric plasma below the ionospheric M1 layer might be explained by high growth of charged particle production caused by a ionization instability in the local weakly-ionized dusty plasma.

As it is mentioned in section 2.3 and chapter 1, interplanetary meteoroids and charged grains pose a problem for both interplanetary missions and planetary exploration. The potential impact risks might be reduced if we clearly know both their population and behavior. The accumulation of space debris around the Earth has be-

come critical for Space security too. Preventing generation of new debris by de-orbiting satellites at end of mission concerns all Space Agencies. The de-orbiting system here considered, involving an electrodynamic bare tape-tether, uses no propellant and no power supply, while generating power for on-board use during de-orbiting. A de-orbit tether system must present small tether-to-satellite mass ratio and very small sever probability too. Chapter 3 showed how to select tape dimensions so as to minimize the product of those two magnitudes. Preliminary results of tape-tether design have been here discussed to minimize that function. Results for de-orbiting Cryosat suggest larger widths to minimize the  $N_f \times m_t/M_s$  product. The range of the width is delimited to collect in OML regime ( $w < 6$  cm), however. Widths might be delimited by the deployer mechanism and stability criteria. Tethers might not be enough competitive against rockets for high inclination orbits and very large  $M_s$ , mainly, because of the uncontrolled reentry for a very large structure, such as Envisat.

---

## BIBLIOGRAPHY

- [1] Alfven, H., Spacecraft Propulsion: New Methods, *Science*, vol. 176, pp. 167-168, 1972.
- [2] Allen, J. E., Probe theory - the orbital motion approach, *Phys. Scripta*, 45, 5, 497-503, 1992.
- [3] Akhiezer, A. I., Polovin, R. V., Sitenko A. G., and Stepanov, K. N., Plasma Electrodynamics, vol.1, Pergamon, New York, 1975.
- [4] Ahedo, E. and Sanmartin, J. R., Analysis of Bare-Tether Systems for Deorbiting LEO Satellites, *Journal of Spacecraft and Rockets*, Vol. 39, No. 2, pp. 198-205, 2002. Doi:10.2514/2.3820
- [5] Bagenal, F., Dowling, T., and McKinnon, W., Jupiter, the Planet, Satellite, and Magnetosphere, Cambridge. U.K., Cambridge University Press, 2004.
- [6] Barnett, A. and Olbert, S., Radiation of plasma waves by a conducting body moving through magnetized plasma, *J. Geophys. Res.* 91, 10117-10135, 1986.
- [7] Battin, R. H., An Introduction to the Mathematics and Methods of Astrodynamics, Revised Edition, AIAA Education Series, Reston, Virginia, 1999.
- [8] Bergman, J., The magnetized plasma permittivity tensor, *Phys. Plasmas*, 7, 3476-3479, 2000.

- 
- [9] Brown, C. D., AIAA Education Series, American Institute of Aeronautics and Astronautics, 370 L'Engant Promenade, SW, Washinton DC, 1992.
- [10] Bryson, A. E., and Ho, Y. C., Applied Optimal Control, Hemisphere Publishing Corporation, New York, NY, 1975.
- [11] Burns, J. A., Schaffer, L. E., Greenberg, R. J. and Showalter, M. R., Lorentz resonances and the structure of the jovian ring, *Nature*, Vol. 316, pp. 115-119, 1985.
- [12] Biancalani, A. and Pegoraro, F., Radiation of plasma waves by a conducting body moving through a magnetized plasma, *J. Geophys. Res.* 115, A03302, 2010. Doi:10.1029/2009JA014812.
- [13] Biancalani, A. and Pegoraro, F., Cherenkov emission of electron-cyclotron waves by a magnetized satellite orbiting the ionosphere, *J. Geophys. Res.* 115, A09330, 2010. Doi:10.1029/2009JA015230.
- [14] Bombardelli, C., Lorenzini, E. C., and Sanmartin, J. R., Jupiter Power Generation with Electrodynamic Tethers at Constant Orbital Energy, *J. of Propulsion and Power*, 25, 2, 2009.
- [15] Bombardelli, C., Sánchez-Torres, A., Charro, M., Sanmartin J. R., and Lorenzini, E.C., A low-orbit, science mission at Jupiter, European Planetary Science Congress, Postdam, Germany, September 13-18, 2009.
- [16] Carrol, J. A. and Oldson, J. C., Tethers for Small Satellite Applications, *AIAA/USU Small Satellite Conference*, Logan, Utah, 1995.
- [17] Cash, J. R. and Karp, A. H., A variable order Runge-Kutta Method for initial value problems with rapidly varying right-hand sides, *ACM Transactions on Mathematical Software*, Vol. 16, No. 3, 201-222, 1990.
- [18] Charro, M., Sanmartin J.R., Bombardelli, C., Sanchez-Torres, A., Lorenzini, E.C., Garrett, H. B. and Evans, R. W., A proposed Two-Stage Two-Tether Scientific Mission at Jupiter, *IEEE Trans. Plasma Sci.*, vol. 40, no. 2, pp. 274-280, 2012.
- [19] Chen, F. F., Plasma Diagnostic Techniques, ed R H Huddleston and S L Leonard, New York, 1965.
-

- [20] Choniere, E., Theory and experimental evaluation of a consistent steady-state kinetic model for two-dimensional conductive structures in ionospheric plasmas with application to bare electrodynamic tethers in space, Ph.D. dissertation, University of Michigan, 2004.
- [21] Choiniere, E., and Gilchrist, B., Selfconsistent 2-D kinetic simulations of high-plasma sheaths surrounding ion-attracting conductive cylinders in flowing plasmas, *IEEE Trans. Plasma Sci.*, vol. 35, no. 1, pp. 7-22, 2007. Doi: 10.1109/TPSS.2006.889300
- [22] Conde, L., The ionization instability and resonant acoustic modes suppression by charge space effects in a dusty plasma, *Phys. Plasmas*. **13**, 032104, 2006.
- [23] Conde, L., Donoso, J.M., Sanchez-Torres, A, Tkachenko, I.M., de la Cal, E., Carralero, D., and Pablos, J.L., Plasmas Granulares, *Real Sociedad Española de Física*, Vol. 25-3. Julio-Septiembre, 2011.
- [24] Danilov, V. V., Elgin, B. A., Grafodatsky, O. S., and Mirnov, V. V., High-Voltage Satellite Tethers For Active Experiments in Space, *Proceedings of the 6th Spacecraft Charging Conference*, p.165-168, November 2-6, 1998.
- [25] Deux, J.M.A., Kinetic modeling of electrodynamic space tethers, M. S. thesis, MIT, Massachusetts, 2005.
- [26] Dikarev, V., Grün, E., Baggaley, J., Galligan, D., Landgraf, M., and Jehn, R., The new ESA meteoroid mode, *Advances in Space Research*, 35, 7 1282-1289, 2005.
- [27] Divine, N. T. and Garrett, H. B., Charged Particle Distributions in Jupiter's Magnetosphere, *J. Geophys. Res.*, 88, 6889-6903, 1983.
- [28] Dobrowolny, M. and Veltri, P., MHD power radiated by a large conductor in motion through a magnetoplasma, *Nuovo Cimento Soc. Ital. Fis. C.*, 9, 27-38, 1986. Doi: 10.1007/BF02508050.
- [29] Donohue, D. J., Neubert, T., and Banks, P. M., Estimating Radiated Power From a Conducting Thethered Satellite System, *J. Geophys. Res.*, 96, 21245-21253, 1991.

- [30] Donoso, J. M., Sanchez-Torres, A., and Conde, L., Stability analysis for dusty plasma under grain charge fluctuations due to non-Maxwellian electron distributions, 37th EPS Conference on Plasma Physics, Dublin, Ireland, June 2010.
- [31] Drell, S. D., Foley, H. M., and Ruderman, M. A., Drag and propulsion of large satellites in the ionosphere: An Alfven propulsion engine in space, *J. Geophys. Res.*, 70, 13, 3131-3145, 1965.
- [32] Else, D., Kompaneets, K., and Vladimirov, S.V., Instability of the ionization-absorption balance in a complex plasma at ion time scales, *Phys. Rev. E*, 80, 016403, 5, 2009.
- [33] Estes, R. D., Alfven waves from an electrodynamic tethered satellite system, *J. Geophys. Res.*, 93, 945-956, 1988.
- [34] Estes R. D. and Sanmartin, J. R., Cylindrical Langmuir probes beyond the orbital-motion-limited regime, *Phys. Plasmas*, 7, 4320-4325, 2000. Doi: 10.1063/1.1288400
- [35] Forward, R. L., Hoyt, R. P., and Uphoff, C., The Terminator Tether: A Near-Term Commercial Application of the NASA/MSFC ProSEDS Experiment, *Proceeding of the Tether Technology Interchanging Meeting*, NASA CP-1998-206900, p. 109, 1998.
- [36] Gilchrist, B., Lim, B., Meckol, N., Masse, R., and Williams, S., The Use of Electrodynamic Tethers for Orbit Maintenance and Deorbit of Large Spacecraft: A Trade Study of the NASA GLAST Mission, *38th AIAA/ASMESAE/SEE Joint Propulsion Conference Meeting and Exhibit*, AIAA Paper 2002-4044, July 2002.
- [37] Godard, R. and Laframboise, J. G., Total current to cylindrical collectors in collisionless plasma flow, *Planetary and Space Science*, 31, 275-283, 1983.
- [38] Grard, R. J. L., Properties of the Satellite Photoelectron Sheath Derived from Photoemission Laboratory Measurements, *Journal of Geophysical Research*, vol. 78, 16, 2885-2906, 1973.
- [39] Grün, E., Zook, H. A., Fechtig, H., and Giese, R. H., Collisional balance of the meteoritic complex, *Icarus*, 62, 2, 244-272, 1985.

- 
- [40] Gurevich, A. V., Distribution of captured particles in a potential well in the absence of collisions, *Soviet Physics JETP*, vol. 26. No. 3, 575-580, March, 1968.
- [41] Hastings, D. E. and Wang, J., The radiation impedance of an electrodynamic tether with end connectors, *J. Geophys. Res. Lett.*, 14, 519-522, 1987.
- [42] Hastings, D. E. and Wang J., Induced emission of radiation from a large space-station-like structure in the ionosphere, *AIAA J.*, 27, 438-445, 1989. Doi: 10.2514/3.10131.
- [43] Hastings, D. E. and Garret, H., *Spacecraft-Environment Interactions*, Cambridge University Press, 1996.
- [44] Hoegy, W. R. and Wharton, L. E., Current to a moving cylindrical electrostatic probe, *Journal of Applied Physics*, 44, 12, 5365, 1973.
- [45] Hoyt, R. P. and Forward, R. L., Performance of the terminator tether for autonomous deorbit of LEO spacecraft, 35th AIAA Joint Propulsion Conference and Exhibit, Los Angeles, June 1999.
- [46] Janhunen, P., Electric Sail for Spacecraft Propulsion, *J. of Propulsion and Power*, 20, 4, 2004.
- [47] Janhunen, P. and Sandroos, A., Simulation study of solar wind push on a charged wire: basis of solar wind electric sail propulsion, *Ann. Geophys.*, 25, 755-767, 2007.
- [48] Janhunen, P., Increased electric sail thrust through removal of trapped shielding electrons by orbit chaotisation due to spacecraft body, *Ann. Geophys.*, 27, 3089-3100, 2009.
- [49] Janhunen, P., On the feasibility of a negative polarity electric sail, *Ann. Geophys.*, 27, 1439-1447, 2009.
- [50] Janhunen, P., et al., Invited Article: Electric solar wind sail: Toward test missions, *Review of Scientific Instruments*, 81, 111301, 2010. Doi: 10.1063/1.3514548
- [51] Kanal, M., Theory of current collection of moving cylindrical probes, *Journal of Applied Physics*, 35, 6, 1964.
-

- [52] Khan, S.B. and Sanmartin, J., Comparison of probability of survival for round and tape tethers against debris impact, *Journal of Spacecraft and Rockets*, 50, 3, 603-608, 2013. Doi: 10.2514/1.A32383
- [53] Kessler, D.J. and Cour-Palais, B.G., Collision Frequency of Artificial Satellites: The Creation of a Debris Belt, *Journal of Geophysical Research*, Vol. 83, No. A6, pp. 2637-2646 1995, 1978.
- [54] Khrapak, S. A., et. al., Ion drag force in complex plasmas, *Phys. Rev. E*, 66, 046414, 1-4, 2002. Doi: 10.1103/PhysRevE.66.046414
- [55] Khrapak, S.A., et al., Scattering in the Attractive Yukawa Potential in the Limit of Strong Interaction, *Phys. Rev. Lett.*, 90, 22, 225002-1, 2003. Doi: 10.1103/PhysRevLett.90.225002
- [56] Laframboise, J. G., Theory of spherical and cylindrical Langmuir probes in a collisionless, Maxwellian plasma at rest, Ph.D. dissertation, Univ. Toronto, Toronto, ON, Canada, Jun. 1966.
- [57] Laframboise, J. G. and Parker, L. W., Probe design for orbit-limited current collection, *Phys. Fluids*, 16, 629, 1973.
- [58] Lam, S. H. and Greenblatt, M., *On the interactions of a solid body with a flowing collisionless plasma, Rarefied Gas Dynamics, Volume 2. Proceedings of the Fourth International Symposium held at the Institute for Aerospace Studies, Toronto, 1964. Edited by J.H. de Leeuw. New York: Academic Press*, pp 45-61, 1965.
- [59] Lam, S. H., Unified Theory for the Langmuir Probe in a Collisionless Plasma, *Phys. Fluids*, 8, 73-87, 1965.
- [60] Landau, L.D. and Lifshitz, E. M., Course of Theoretical physics, Physical Kinetics, vol. 10, Pergamon, GB, 1981.
- [61] Lawden, D. F., Optimal trajectories for space navigation, pp. 54-68, Butterworths, London, 1963.
- [62] Leblanc, Y., Dulk, G. A., and Bougeret, J., Tracing the Electron Density from the Corona to 1 AU, *Solar physics*, 183, 1, 165-180, 1998. Doi: 10.1023/A:1005049730506



- [63] McNamara, H., Jones, J., Kauffman, B., Suggs, R., Cooke, W., and Smith, S. Meteoroid Engineering Model (MEM): A Meteoroid Model for the Inner Solar System. *Earth, Moon, and Planets*, 95, 123-139, 2004.
- [64] Maksimovic, M., Pierrard, V., and Lemaire, J. F., A kinetic model of the solar wind with Kappa distribution functions in the corona, *Astronomy and Astrophysics*, 324, 725-734, 1997.
- [65] Mamun, A. A. and Shukla, P. K., The role of dust charge fluctuations on nonlinear dust ion-acoustic waves, *IEEE Transactions on Plasma Science*, 30, 2, 720-724, 2002.
- [66] Martinez-Sanchez, M. and Sanmartin J. R., Artificial auroral effects from a bare conducting tether, *J. Geophys. Res.*, 102, 27257-27263, 1997.
- [67] Matousek, S., The Juno New Frontiers mission, *Acta Astronautica*, 61, 923-939, 2007.
- [68] McMahon, J. C., Xu, G. Z. and Laframboise, J. G., The effect of ion drift on the sheath, presheath, and ion-current collection for cylinders in a collisionless plasma, *Physics of Plasmas*, 12, 062109-1 -062109-11, 2005.
- [69] Mengali, G., Quarta, A. Q., and Janhunen, P., Electric Sail Performance Analysis, *J. of Spacecraft and Rockets*, 45, 1, 2008.
- [70] Mengali, G. and Quarta, A. Q., Non-Keplerian orbits for electric sails, *Celest. Mech. Dyn. Astr.*, 105, 179-195, 2009. Doi 10.1007/s10569-009-9200-y.
- [71] Meyer-Vernet, N. and Issautier, K., Electron temperature in the solar wind: Generic radial variation from kinetic collisionless models, *J. Geophys. Res.*, 103, 12, 29705-29717, 1998. Doi: 10.1029/98JA02853
- [72] Rubab, N. and Murtaza, G., Dust-charge fluctuations with non-Maxwellian distribution functions *Phys. Scr.*, 73, 178-183, 2006.
- [73] Onishi, T., Numerical Study of Current Collection by an Orbiting Bare Tether, Ph.D. thesis, MIT, Massachusetts, 2002.

- [74] Onishi, T., Martínez-Sánchez, M., Cooke, D. L., Sanmartín, J. R., PIC computation of Electron Current Collection To a Moving Bare Tether In the Mesothermal Condition, *27 th IEPC*, Pasadena, California, USA, October 15-19, 2001.
- [75] Bhatt, J. R. and Pandey, B. P., Self-consistent charge dynamics and collective modes in a dusty plasma, *Phys. Rev. E* **50**, 3980, 1994.
- [76] Pardini, C., Hanada, T., and Krisko, P. H., Potential Benefits and Risks of Using Electro-Dynamic Tethers for End-of-Life De-Orbit of LEO Spacecraft, *Final Rept. of IADC Action Item19.1*, IADC-06-02, 27 April 2006.
- [77] Pardini, C., Hanada, T., and Krisko, P. H., Benefits and Risks of Using Electro-Dynamic Tethers to De-Orbit Spacecraft, *Acta Astronautica*, 64, 571-588, 2009. Doi:10.1016/j.actaastro.2008.10.007
- [78] Parker, E. N., Dynamics of the Interplanetary Gas and Magnetic Fields, *Astrophysical Journal*, 128, 664-676, 1958.
- [79] Parker, L. W. and Murphy, B. L., Potential Buildup on an Electron-Emitting Ionospheric Satellite, *J. Geophys. Res.*, 72, 5, 1631-1636, 1967.
- [80] Quarta, A. A., Mengali, G., and Janhunen, P., Optimal interplanetary rendezvous combining electric sail and high thrust propulsion system, *Acta Astronautica*, 68, 603-621, 2011.
- [81] National Academy of Sciences, Radioisotope Power Systems: An imperative for Maintaining U.S. Leadership in Space Exploration, <http://books.nap.edu/catalog/12653.html>
- [82] Russell, R. P., Primer vector theory applied to global low-thrust trade studies, *Journal of Guidance, Control, and Dynamics*, 30, 2, 460-472, 2007.
- [83] Sanchez-Arriaga, G. and Sanmartin, J. R., Magnetic pumping of whistler waves by tether current modulation, *J. Geophys. Res.*, 115, A02311, 2010.
- [84] Sanchez-Arriaga, G., Charro, M., and Sanmartin, J. R., A corrected tether-mission to Jupiter, European Planetary Science Congress 2012, Madrid, Spain, 23-28 Sept. 2012.

- [85] Sanchez-Arriaga, G. and Sanmartin, J. R. Relativistic current collection by a cylindrical Langmuir probe, *Physics of plasmas*, 19, 063506-1,8, 2012.
- [86] Sanchez-Torres, A., Sanmartin J. R., and Donoso, J. M., The radiation impedance of electrodynamic tethers in Jupiter, *37th Cospar Scientific Assembly*, Montreal, Canada, July 2008.
- [87] Sanchez-Torres, A., Sanmartin J.R., Donoso, J.M., and Charro, M., The radiation impedance of electrodynamic tethers in a polar Jovian orbit, *Advances in Space Research*, 2010, Doi:10.1016/j.asr.2009.12.007.
- [88] Sanchez-Torres, A. and J. R. Sanmartin, The radiation impedance of a current-carrying conductor in a JUNO-like Jovian orbit, *38th Cospar Scientific Assembly*, Bremen, Germany, July 2010.
- [89] Sanchez-Torres, A., L. Conde, and J. M. Donoso, The ionization instability of a weakly ionized dusty plasma with grain charge fluctuations, *38th Cospar Scientific Assembly*, Bremen, Germany, July 2010.
- [90] Sanchez-Torres, A. and Sanmartin J.R., Tether radiation in Juno-type and circular-equatorial Jovian orbits, *Journal of Geophysical Research*, 116, A12, A12226, 1-12, 2011.
- [91] Sanchez-Torres, A., Radioisotopes - Applications in Physical Sciences. Chapter: Radioisotope Power Systems for Space Applications, *INTECH*, ISBN: 978-953-307-510-5, pp. 457-472, 2011.
- [92] Sanchez-Torres, A., Propulsive Force in an Electric Solar Sail, *10<sup>th</sup> International Workshop on Electric Probes in Magnetized Plasmas (IWEP2013)*, Madrid, 9-12 July, 2013.
- [93] Sanmartin, J. R., Martinez-Sanchez, M., and Ahedo, E., Bare Wire Anodes for Electrodynamic Tethers, *Journal of Propulsion and Power*, Vol. 9, No. 3, 353-360, 1993.
- [94] Sanmartin J. R. and Martinez-Sanchez, M., The radiation impedance of orbiting conductors, *J. Geophys. Res.*, 100, 1677-1686, 1995.

- [95] Sanmartin J. R. and R. D. Estes, The orbital-motion-limited regime of cylindrical Langmuir probes, *Phys. Plasmas* 6, 395-405, 1999. Doi: 10.1063/1.873293
- [96] Sanmartin, J. R. and Estes, R. D., Interference of parallel cylindrical Langmuir probes, *Phys. Plasmas*, 8, 4234-4239, 2001. Doi: 10.1063/1.1390332
- [97] Sanmartin J. R., Physics and Applications of Electrodynamic Space Tethers, Simplicity, Rigor and Relevance in Fluid Mechanics, eds. Higuera, Jimenez and Vega, CIMNE, Barcelona, Spain, 2004, pp. 316-330.
- [98] Sanmartin J. R., Charro, M., Pelaez, J., Tinao, I., Elaskar, S., Hilgers, A., and Martinez-Sanchez, M., Floating bare tether as upper atmosphere probe, *J. Geophys. Res.*, 111, A11310, Doi: 10.1029/2006JA011624, 2006.
- [99] Sanmartin, J. R., Choniere, E., Gilchrist, B. E., Ferry, J., and Martinez-Sanchez, M., Bare-tether sheath and current: comparison of asymptotic theory and kinetic simulations in stationary plasma, *IEEE Trans. Plasma Phys.*, 36, 2851-2858, 2008. Doi: 10.1109/TPS.2008.2003978
- [100] Sanmartin J. R., Charro, M., Lorenzini, E. C., Garrett, H. B., Bombardelli, C., and Bramanti, C., Electrodynamic Tether at Jupiter-I: Capture Operation and Constraints, *IEEE Trans. Plasma Sci.*, 36, no. 5, 2450-2458, Oct. 2008.
- [101] Sanmartin J. R., Charro, M., Lorenzini, E. C., Garrett, H. B., Bombardelli, C., and Bramanti, C., Electrodynamic Tether at Jupiter-II: Fast Moon Tour After Capture, *IEEE Trans. Plasma Sci.*, 7, no. 4, 620-626, Apr. 2009.
- [102] Sanmartin J. R., Bombardelli, C., and Sanchez-Torres, A., A light tether mission at Jupiter, *SPINE Meeting*, ONERA, Toulouse, September 28-29, 2009.
- [103] Sanmartin J. R., A review of electrodynamic tethers for science applications, *Plasma Sources Sci. Technol.*, 19, 1-7, 2010. Doi: 10.1088/0963-0252/19/3/034022.
- [104] Sanmartin, J. R., Lorenzini, E., and Martinez-Sanchez, M., Electrodynamic Tether Applications and Constraints, *Journal of Spacecraft and Rockets*, Vol. 9, No. 3, 442-456, 2010. Doi: 10.2514/1.45352

- [105] Sanmartin J. R., Sanchez-Torres, A., Bombardelli, C., Charro, M., and Lorenzini, E. C., A Light Tether, Low-Orbit Scientific Mission at Jupiter, *3<sup>rd</sup> Europa Jupiter System Mission (EJSM) Instrument Workshop*, ESA, ESTEC, January 2010.
- [106] Sanmartin J. R., Sanchez-Torres, A., and Khan, S. B., Sheath Interference Effects in the Bare-tether Array of an Electric Solar Sail, *11th Spacecraft Charging Technology Conference*, Albuquerque, NM, 20-24 September 2010.
- [107] Sanmartin J. R. and Sanchez-Torres, A., Tether de-orbiting of satellite at end of mission, *39th COSPAR Scientific Assembly*, Mysore, India, July 14-22, 2012.
- [108] Sanmartin, J. R., Sanchez-Torres, A., Khan, S. B., Sanchez-Arriaga, G., and Charro, M., Tape-tether design for de-orbiting from given altitude and inclination, *6th European Conference on Space Debris*, ESA/ESOC, Darmstadt, Germany, April 22-25, 2013.
- [109] Scuddeer, J. D. and Olbert, S., A theory of local and global processes which affect solar wind electrons 2. Experimental support, *Journal of Geophysical Research*, 84, A11, 6603-6620, 1979.
- [110] Segall, S. B. and Koopman, D. W., Application of cylindrical Langmuir probes to straming plasma diagnostics, *The Physics of Fluids*, 16, 7, 1149-1156, 1973.
- [111] Shukla, P. K. and Mamun, A. A., Introduction to dusty plasma physics, *IoP. Series in Plasma Physics*, London, 2002.
- [112] Sittler, E.C. and Scudder, J.D., An empirical polytrophe law for solar wind thermal electrons between 0.45 and 4.76 AU: Voyager 2 and Mariner 10, *Journal of Geophysical Research*, 85, A10, 5131-5137.
- [113] Stangeby, P. C. and Allen, J. E., Transonic plasma flow past an obstacle, *J. Plasma Physics*, 6, 1, 19-32, 1971.
- [114] Summers, D., On the two-fluid polytropic solar wind model, *The Atrophysical Journal*, 257, 881-886, 1982.
- [115] Tsytovich V. N., Morfill, G. E., Vladimirov, S. V., and Thomas, H., Elementary Physics of Complex Plasmas. Springer-Verlag, Berlin, 2008.

- [116] Van der Heide, E.J. and Kruijff, M., Tethers and Debris Mitigation, *Acta Astronautica*, 48, 503-516, 2001. Doi: 10.1016/S0094-5765(01)00074-1
- [117] Wang, X., Bhattacharjee, A., Gou, S. K. and Goree. J., Ionization instabilities and resonant acoustic modes, *Phys. Plasmas*, 8, 5018-5024, 2001.
- [118] Winglee, R. M., Slough, J., Ziemba, T., and Goodson, A., Mini-Magnetospheric Plasma Propulsion: Tapping the energy of the solar wind for spacecraft propulsion, *Journal of Geophysical Research*, vol. 105, A9, 21067-21077, 2000.
- [119] Zanutto D., Colombatti, G., Lorenzini, E., Mantellato, R., and Sanchez-Torres, A., Orbital debris mitigation through deorbiting with passive electrodynamic drag, *Proceedings of the 63th International Astronautical Congress*, IAC-12-D9.2.8., ISSN: 0074-1795, 2012.
- [120] Zubrin, R. M. and Andrews, D. G., Magnetic sails and interplanetary travel, *Journal of Spacecraft and Rockets*, 28, 197-203, 1991.

## APPENDIX A

### THE RADIATION IMPEDANCE WITH THERMAL EFFECTS

In section 2.2 the radiation impedance is determined with the simple cold approximation. A difference between Jovian and LEO cases is the relative-to-thermal velocity ratio. Unlike LEO ( $V_{rel}^{LEO} \gg V_{ti}$ ), the Jovian ambient condition gives  $V_{rel} \sim V_{ti}$  for both Juno and LJO. In this section we briefly discuss the radiation impedance with thermal effects. This effect will be studied in detail in a future work. Thermal contributions in the dielectric tensor are given by the dispersion relation for warm plasma,  $\mathcal{D}_{th} = An^4 + Bn^2 + C = 0$  [3], where

$$A = \varepsilon_{11} \sin^2 \theta + 2\varepsilon_{13} \sin \theta \cos \theta + \varepsilon_{33} \cos \theta, \quad (\text{A.1})$$

$$B = -\varepsilon_{11}\varepsilon_{33} - (\varepsilon_{22}\varepsilon_{33} + \varepsilon_{23}^2) \cos^2 \theta - (\varepsilon_{11}\varepsilon_{22} + \varepsilon_{12}^2) \sin^2 \theta, \\ + 2(\varepsilon_{12}\varepsilon_{23} - \varepsilon_{22}\varepsilon_{13}) \sin \theta \cos \theta + \varepsilon_{13}^2, \quad (\text{A.2})$$

$$C = \varepsilon_{33}(\varepsilon_{11}\varepsilon_{22} + \varepsilon_{12}^2) + \varepsilon_{11}\varepsilon_{23}^2 + 2\varepsilon_{12}\varepsilon_{13}\varepsilon_{23} - \varepsilon_{22}\varepsilon_{13}^2. \quad (\text{A.3})$$

Wavelengths along the magnetic field are larger than the Larmor radius,  $\rho_\alpha = V_{t_\alpha}/\Omega_\alpha$ , for particles of thermal velocity  $V_{t_\alpha} \sim V_\perp$  and  $w < \Omega_i$  (Alfven range). Following the work of Bergman [8] for thermal velocity corrections, the dielectric tensor for ions reads

$$\varepsilon(\mathbf{k}, \omega) = \mathbf{I} - \frac{i\omega_{pi}^2}{\omega\Omega_i} \int_0^\infty (\mathcal{T}^{(1)}(\eta) - \mathcal{T}^{(2)}(\eta)) \\ \times \exp \left[ -\frac{k_z^2 V_{ti}^2 \eta^2}{2\Omega_i^2} - \frac{k_\perp^2 V_{ti}^2}{\Omega_i^2} (1 - \cos \eta) - \frac{i\omega\eta}{\Omega_i} \right] d\eta, \quad (\text{A.4})$$

where  $\mathbf{I}$  is the unit tensor. The tensor  $\mathcal{T}^{(1)}(\eta)$  is

$$\mathcal{T}^{(1)}(\eta) = \begin{pmatrix} \cos \eta & -\sin \eta & 0 \\ \sin \eta & \cos \eta & 0 \\ 0 & 0 & 1 \end{pmatrix}$$

and  $\mathcal{T}^{(2)}(\eta)$  is

$$\mathcal{T}^{(2)}(\eta) = \frac{V_{ti}^2}{\Omega_i^2} \begin{pmatrix} k_{\perp}^2 \sin^2 \eta & -k_{\perp}^2 \sin \eta (1 - \cos \eta) & k_{\perp} k_z \eta \sin \eta \\ k_{\perp}^2 \sin \eta (1 - \cos \eta) & -k_{\perp}^2 (1 - \cos \eta)^2 & k_{\perp} k_z \eta (1 - \cos \eta) \\ k_{\perp} k_z \eta \sin \eta & -k_{\perp} k_z \eta (1 - \cos \eta) & k_z^2 \eta^2 \end{pmatrix}.$$

For the element of the dielectric tensor  $\varepsilon_{11}$ , we have

$$\mathcal{T}_{11}^{(1)}(\eta) = \cos \eta, \quad \mathcal{T}_{11}^{(2)}(\eta) = \frac{V_{ti}^2}{\Omega_i^2} k_{\perp}^2 \sin^2 \eta, \quad (\text{A.5})$$

Since  $k_z \ll 1$ , the element of the dielectric tensor  $\varepsilon_{11}$  reads

$$\begin{aligned} \varepsilon_{11}(k_{\perp}, \omega) &= 1 - \frac{i\omega_{pi}^2}{\omega\Omega_i} \int_0^{\infty} \left( \cos \eta - k_{\perp}^2 \frac{V_{ti}^2}{\Omega_i^2} \sin^2 \eta \right) \\ &\times \exp \left[ -\frac{k_{\perp}^2 V_{ti}^2}{\Omega_i^2} (1 - \cos \eta) - \frac{i\omega\eta}{\Omega_i} \right] d\eta. \end{aligned} \quad (\text{A.6})$$

Making the following expansion

$$\exp \left[ -\frac{k_{\perp}^2 V_{ti}^2}{\Omega_i^2} (1 - \cos \eta) \right] \approx 1 - \frac{k_{\perp}^2 V_{ti}^2}{\Omega_i^2} (1 - \cos \eta) + \frac{k_{\perp}^4 V_{ti}^4}{2\Omega_i^4} (1 - \cos \eta)^2, \quad (\text{A.7})$$

the element of the dielectric tensor  $\varepsilon_{11}$  in Eq. (A.6) may be rewritten as

$$\begin{aligned} \varepsilon_{11}(k_{\perp}, \omega) &\approx 1 - \frac{i\omega_{pi}^2}{\omega\Omega_i} \int_0^{\infty} \left( \cos \eta - k_{\perp}^2 \frac{V_{ti}^2}{\Omega_i^2} \sin^2 \eta \right) \exp \left[ \frac{-i\omega\eta}{\Omega_i} \right] \\ &\times \left[ 1 - \frac{k_{\perp}^2 V_{ti}^2}{\Omega_i^2} (1 - \cos \eta) + \frac{k_{\perp}^4 V_{ti}^4}{2\Omega_i^4} (1 - \cos \eta)^2 \right] d\eta. \end{aligned} \quad (\text{A.8})$$

Carrying out the integral and retaining the terms of order  $(k_{\perp}\rho_i)^4$  we get

$$\varepsilon_{11}(k_{\perp}, \omega) \approx 1 + \frac{\omega_{pi}^2}{\Omega_i^2 - \omega^2} \left[ 1 - \frac{3V_{ti}^2 k_{\perp}^2}{4\Omega_i^2 - \omega^2} + \frac{15V_{ti}^4 k_{\perp}^4}{(9\Omega_i^2 - \omega^2)(4\Omega_i^2 - \omega^2)} \right]. \quad (\text{A.9})$$

Finally, with some algebra we have

$$\begin{aligned} \varepsilon_{11}(k_{\perp}, \omega) &\approx \frac{\Omega_i^2 + \omega_{pi}^2 - \omega^2}{\Omega_i^2 - \omega^2} \left\{ 1 - \frac{3V_{ti}^2 k_{\perp}^2 \omega_{pi}^2}{(4\Omega_i^2 - \omega^2)(\Omega_i^2 + \omega_{pi}^2 - \omega^2)} \right. \\ &\left. + \frac{15V_{ti}^4 k_{\perp}^4 \omega_{pi}^2}{(9\Omega_i^2 - \omega^2)(4\Omega_i^2 - \omega^2)(\Omega_i^2 + \omega_{pi}^2 - \omega^2)} \right\}. \end{aligned} \quad (\text{A.10})$$



Considering  $\varepsilon_{11}$  and  $\varepsilon_{33}$  the terms which contribute to the impedance, Eq. (A.1) reads

$$A = \varepsilon_{11} \sin^2 \theta + \varepsilon_{33} \cos \theta \quad (\text{A.11})$$

where  $\cos \theta \ll 1$ . Changing the element tensor from  $\varepsilon_1$  to  $\varepsilon_{11}$  in equation 2.46 the radiation impedance with thermal effects for Juno-like orbit at equator (see Eq. (2.42)) would be

$$\begin{aligned} Z_A = & \frac{8V_A}{\pi c^2 \sqrt{1 + (V_A/c)^2}} \int_0^{\pi/2} \frac{d\varphi}{\pi/2} \int_0^{2\pi} d\alpha \int_0^{k_M} \frac{dk_{\perp}}{k_{\perp}} \frac{\sqrt{1 - k_{\perp}^2/k_M^2} \sin^2(\frac{1}{2}k_{\perp}L \sin \varphi \sin \alpha)}{\sqrt{1 - k_{\perp}^2/\tilde{k}_M^2}} \\ & \times \sqrt{1 + \frac{k_{\perp}^2}{k_m^2} \frac{\sin^2(k_{\perp}/k_R)}{(k_{\perp}/k_R)^2} \frac{1}{\mathcal{C}_{th}}} \end{aligned} \quad (\text{A.12})$$

where

$$\mathcal{C}_{th} = \sqrt{\left| 1 - \frac{3V_{ti}^2 k_{\perp}^2 \omega_{pi}^2}{(4\Omega_i^2 - \omega^2)(\Omega_i^2 + \omega_{pi}^2 - \omega^2)} + \frac{15V_{ti}^4 k_{\perp}^4 \omega_{pi}^2}{(4\Omega_i^2 - \omega^2)(9\Omega_i^2 - \omega^2)(\Omega_i^2 + \omega_{pi}^2 - \omega^2)} \right|} \quad (\text{A.13})$$

Thermal effects of orders could be analyzed. Carrying out  $\varphi$ -integrand we have

$$\begin{aligned} Z_A = & \frac{4V_A}{\pi c^2 \sqrt{1 + (V_A/c)^2}} \int_0^{2\pi} d\alpha \int_0^{k_M} \frac{dk_{\perp}}{k_{\perp}} \frac{\sqrt{1 - k_{\perp}^2/k_M^2}}{\sqrt{1 - k_{\perp}^2/\tilde{k}_M^2}} \\ & \times \sqrt{1 + \frac{k_{\perp}^2}{k_m^2} \frac{\sin^2(k_{\perp}/k_R)}{(k_{\perp}/k_R)^2} \frac{[1 - J_0(k_{\perp}L \sin \alpha)]}{\mathcal{C}_{th}}}. \end{aligned} \quad (\text{A.14})$$

Both analytical and numerical solution will be carried out in a future work. Notice that the thermal effects here occurs for the range of Alfven mode ( $0 < \omega < \Omega_i$ ).



## APPENDIX B

### MODIFIED EQUINOCTIAL EQUATIONS FOR ORBITAL MECHANICS

The disturbed motion of two bodies may be described by the Lagrange equations [7]. Several variational elements associated to the Lagrange equations are singular for both  $i = 0$  and  $e = 0$ . For some orbits is then convenient to modify classical orbital elements with the following non-singular elements

$$p = a(1 - e^2), \quad (\text{B.1})$$

$$f = e \cos(\Omega + \omega), \quad (\text{B.2})$$

$$g = e \sin(\Omega + \omega), \quad (\text{B.3})$$

$$L = M + \Omega + \omega, \quad (\text{B.4})$$

$$h = \tan\left(\frac{i}{2}\right) \cos \Omega, \quad (\text{B.5})$$

$$k = \tan\left(\frac{i}{2}\right) \sin \Omega, \quad (\text{B.6})$$

The transformation from the equinoctial elements to the classical orbital elements is

$$a = \frac{p}{1 - f^2 - g^2}, \quad (\text{B.7})$$

$$e = \sqrt{f^2 + g^2}, \quad (\text{B.8})$$

$$i = 2 \tan^{-1} \sqrt{h^2 + k^2}, \quad (\text{B.9})$$

$$\Omega = \tan^{-1} \frac{k}{h}, \quad (\text{B.10})$$

$$\omega = \tan^{-1} \frac{g}{f} - \tan^{-1} \frac{k}{h}, \quad (\text{B.11})$$

$$\nu = L - \tan^{-1} \frac{g}{f}, \quad (\text{B.12})$$

Relation between Earth-Centered Inertial (ECI) state vector and modified equinoctial elements. Position is

$$\mathbf{r} = \begin{pmatrix} \frac{r}{s^2} (\cos L + \alpha^2 \cos L + 2hk \sin L) \\ \frac{r}{s^2} (\sin L - \alpha^2 \sin L + 2hk \sin L) \\ \frac{2r}{s^2} (h \sin L - k \cos L) \end{pmatrix},$$

and velocity is

$$\mathbf{v} = \begin{pmatrix} -\frac{1}{s^2} \sqrt{\frac{\mu}{p}} (\sin L + \alpha^2 \sin L - 2hk \cos L + g - 2f hk + \alpha^2 g) \\ -\frac{1}{s^2} \sqrt{\frac{\mu}{p}} (-\cos L + \alpha^2 \cos L + 2hk \sin L - f + 2ghk + \alpha^2 f) \\ -\frac{2}{s^2} \sqrt{\frac{\mu}{p}} (h \cos L + k \sin L + fh + gk) \end{pmatrix},$$

where

$$\alpha = h^2 - k^2, \quad (\text{B.13})$$

$$s = \sqrt{1 + h^2 + k^2}, \quad (\text{B.14})$$

$$r = p/w, \quad (\text{B.15})$$

$$w = 1 + f \cos L + g \sin L, \quad (\text{B.16})$$

The system of first-order modified equinoctial equations of orbital motion are

$$\dot{p} = \frac{2p}{w} \sqrt{\frac{p}{\mu}} \Delta_t, \quad (\text{B.17})$$

$$\dot{f} = \sqrt{\frac{p}{\mu}} \left[ \Delta_r \sin L + [f + (1+w) \cos L] \frac{\Delta_t}{w} - (h \sin L - k \cos L) \frac{g}{w} \Delta_n \right], \quad (\text{B.18})$$

$$\dot{g} = \sqrt{\frac{p}{\mu}} \left[ -\Delta_r \cos L + [g + (1+w) \sin L] \frac{\Delta_t}{w} + (h \sin L - k \cos L) \frac{f}{w} \Delta_n \right] \quad (\text{B.19})$$

$$\dot{h} = \sqrt{\frac{p}{\mu}} \frac{s^2 \cos L}{2w} \Delta_n, \quad (\text{B.20})$$

$$\dot{k} = \sqrt{\frac{p}{\mu}} \frac{s^2 \sin L}{2w} \Delta_n, \quad (\text{B.21})$$

$$\dot{L} = \sqrt{\mu p} \left( \frac{w}{p} \right)^2 + \frac{1}{w} \sqrt{\frac{p}{\mu}} (h \sin L - k \cos L) \Delta_n, \quad (\text{B.22})$$

where  $\Delta_r$ ,  $\Delta_t$  and  $\Delta_n$  are non-two-body perturbations in radial, tangential and normal directions, respectively. The radial direction is along the geocentric radius vector of the spacecraft measured positive in a direction away from the geocenter, the tangential direction is perpendicular to the radius, and the normal direction is positive along the angular momentum of the spacecraft orbit. The equation of motion is rewritten as

$$\mathbf{y} = \mathcal{A} \mathbf{P} + \mathbf{b}, \quad (\text{B.23})$$

where

$$\mathcal{A} = \begin{pmatrix} 0 & \frac{2p}{w} \sqrt{\frac{p}{\mu}} & 0 \\ \sqrt{\frac{p}{\mu}} \sin L & \sqrt{\frac{p}{\mu}} \frac{1}{w} [f + (1+w) \cos L] & -\sqrt{\frac{p}{\mu}} \frac{g}{w} [h \sin L - k \cos L] \\ -\sqrt{\frac{p}{\mu}} \cos L & \sqrt{\frac{p}{\mu}} \frac{1}{w} [g + (1+w) \sin L] & \sqrt{\frac{p}{\mu}} \frac{f}{w} [h \sin L - k \cos L] \\ 0 & 0 & \frac{s^2 \cos L}{2w} \\ 0 & 0 & \frac{s^2 \sin L}{2w} \\ 0 & 0 & \sqrt{\frac{p}{\mu}} \frac{1}{w} [h \sin L - k \cos L] \end{pmatrix},$$

and  $\mathbf{b} = [0 \ 0 \ 0 \ 0 \ 0 \ \sqrt{\mu p} (w/p)^2]^T$ . The acceleration vector of the non-two-body is

$$\mathbf{P} = \Delta_r \mathbf{i}_r + \Delta_t \mathbf{i}_t + \Delta_n \mathbf{i}_n, \quad (\text{B.24})$$

where  $\mathbf{i}_r$ ,  $\mathbf{i}_t$  and  $\mathbf{i}_n$  are unit vectors for radial, tangential and normal directions,

$$\mathbf{i}_r = \frac{\mathbf{r}}{|\mathbf{r}|}, \quad \mathbf{i}_n = \frac{\mathbf{r} \wedge \mathbf{v}}{|\mathbf{r} \wedge \mathbf{v}|}, \quad \mathbf{i}_t = \mathbf{i}_n \wedge \mathbf{i}_r, \quad (\text{B.25})$$

from unperturbed two-body motion,  $\mathbf{P} = 0$  and the equations of motion are  $\dot{p} = \dot{f} = \dot{g} = \dot{h} = \dot{k} = 0$ .

For non-spherical planet, as occurs for both Earth and Jupiter, may be expressed as follows

$$\mathbf{g} = g_n \mathbf{i}_N - g_r \mathbf{i}_r, \quad (\text{B.26})$$

with gravity components

$$g_N = -\frac{\mu \cos \lambda}{r^2} \sum_{k=2}^{\infty} \left(\frac{a}{r}\right)^k P'_k J_k, \quad (\text{B.27})$$

$$g_r = -\frac{\mu}{r^2} \sum_{k=2}^{\infty} (k+1) \left(\frac{a}{r}\right)^k P_k J_k, \quad (\text{B.28})$$

where

$$\mathbf{i}_N = \frac{\mathbf{e}_N - (\mathbf{e}_N^T \mathbf{i}_r) \mathbf{i}_r}{|\mathbf{e}_N - (\mathbf{e}_N^T \mathbf{i}_r) \mathbf{i}_r|}, \quad \mathbf{e}_N = (0 \ 0 \ 1)^T.$$

